Ultrasonic measurement of the phonon Hall viscosity

A Dissertation
Presented to the Faculty of the Graduate School
of Cornell University
in Partial Fulfillment of the Requirements for the Degree of
Doctor of Philosophy

Avi Shragai
December, 2025

Ultrasonic measurement of the phonon Hall viscosity

Avi Shragai, Ph.D.
Cornell University, 2025

Detecting new states of matter requires new experimental probes. For example, though the quantum spin liquid has been studied theoretically for decades, it remains challenging to identify a spin liquid in the lab. Measurement of the thermal Hall conductivity has emerged as a promising new tool for identifying exotic states of matter, including the spin liquid. However, the interpretation these data is complicated by the fact that the transport measurement is agnostic to the type of heat carrier. Additionally, it is difficult to determine from the transport measurement whether the Hall conductivity is intrinsic, a property of bandstructure, or extrinsic, a result of scattering. For this reason, experimental probes with additional specificity are needed to clarify the mechanism of the thermal Hall effect.

Here, we develop an experimental technique using pulse echo ultrasound to isolate the intrinsic phonon Hall effect, which is a consequence of phonon Berry curvature, or equivalently, Hall viscosity. In addition to a thermal Hall effect, phonon Hall viscosity results in an acousitc Faraday effect – the time-odd rotation of the polarization of transverse sound waves. The experimental method presented here measures the acoustic Faraday rotation and is therefore sensitive specifically to the source of intrinsic phonon Hall conductivity.

We first test the technique in yittrium iron garnet (YIG), a simple ferrimagnet with known magnetoelastic coupling. Using broadband ultrasonic transducers, we extend the existing measurements of the Faraday rotation of YIG, strengthening the interpretation of the data in terms of Kittel's model of coupled magnons and phonons.

After confirming the validity of the method, we turn to the spin liquid candidate α-RuCl$_3$. We find non-zero phonon Hall viscosity in α-RuCl$_3$ which peaks near its critical magnetic field, suggesting that the viscosity is the result of coupled spin and lattice degrees of freedom. The Hall viscosity persists above the Neel temperature of α-RuCl$_3$, implying a mechanism distinct from magnon-phonon hybridization. The value of the Hall viscosity we extract can account for a significant portion of the observed thermal Hall effect, implying that the thermal Hall effect of α-RuCl$_3$ is largely intrinsic, with the transverse heat carried by phonons.

Biographical Sketch

Before the yearly wildfires and just after a devastating earthquake, Avi was born in Oakland, California. Educated by Jewish hippies, he spent his early years wearing Tevas and biking through Tilden park. He was lucky to have incredible parents who somehow had the patience to take him and his sister on long road trips, exploring National Parks up and down the west coast.

Avi's path to physics was, well, circuitous. After things kind of exploded at the end of high school, he ended up working at a sandwich shop, bopping around the world, then back at the sandwich shop, then to China, where he almost applied for college. Not quite, though. Three years later, still at a martial arts academy in Hubei and looking for ways to spend his free time, he decided to see what this physics stuff was all about. Beginning with Walter Lewin's lectures and moving through Griffiths, he was hooked. Endless puzzles that somehow said something about the *real* world – what could be better? Finally, an old man of twenty-six, he set out to study physics in earnest as an undergraduate at UC Santa Barbara.

During his second semester of undergraduate studies, Avi had the good fortune of taking a class on waves taught by Andrea Young. Andrea offered him the opportunity to work in his lab, and Avi ate it up. He wound a football field-length of superconducting wire around a brass tube to make a magnet. He spent hours at the mill and lathe machining bits of copper, brass, and fiberglass. Mentored by two of Andrea's students, Marec and Charlie, he found the messy complications of experiments a perfect complement to the mathy bits of physics.

Unable to tolerate blue skies, avocado trees, and ocean air any longer, Avi enrolled in graduate school at Cornell. Again taking a somewhat winding path, through the worlds of 2D physics and data engineering, he landed in Brad Ramshaw's group. He was struck by the elegant, conceptually beautiful way the group approached physics problems, and spent the next seven years shaking rocks, climbing rocks.

Acknowledgments

Breathing life into this project was not easy, and I never could have done it alone. Anyone who has undertaken something similar – engaging, amorphous, consuming, unevenly satisfying – knows that it requires effort on all fronts. I am so grateful to everyone who helped me through.

Thank you Brad for sharing your passion for physics. I have learned so much from you about how to think about the subject, starting with chunks of metal, vacuum grease, and compressors and ending with an interpretation of data. The project we worked on, the focus of this thesis, needed clear thinking at every link of that chain and would not have come together as it did without the grounded, physical flavor of understanding you insist on. Thank you also for your optimism, which helped push this project through some very uncertain moments. It was definitely worth it.

I had the privilege of bridging the startup and tenured phases of Brad's lab, being the last group member to have worked with the very first batch of students. It has been amazing to see the lab develop in both technique and scientific direction. For me, it has meant the opportunity to engage with so many smart people both in the process of building the lab up and, more recently, using that infrastructure to do some pretty amazing science.

Thank you Patrick for teaching me how to do pulse echo experiments, from the details of fabricating transducers to a deep suspicion of measuring ultrasound attenuation. Florian, I learned so much from talking with you about your work on superconductivity and from the level of professionalism you brought to the lab. Gael, no one can match your unique blend of intuitive thinking combined with warmth and inclusivity at work – you made the lab a friendlier place. Alex, thank you for showing me that RF electronics are not voodoo magic and for helping us push the pulse echo technique beyond what we thought possible.

Yifei it has been so much fun thinking together about thermal transport (though maybe more fun for me than for you). Talking with you about your experiments and doing some thermal transport measurements of my own has allowed me to look at the data with clearer eyes. It's also nice to have someone to chat with during helium transfers. Sahas, as the first "new" member of the group to invest in pulse echo, I have benefited tremendously from your incisive questions and understanding of the guts of the experiment. I'm super excited to see where you take it during the rest of your PhD. In that same vein, Juan Pablo, it has been great to work with you over the past year shattering my assumptions about transducers and reaching unspeakable levels of signal to noise. The future is bright!

Thank you, too, to the undergraduates I had the opportunity to work with. Andrej, who escaped into the world of finance but suffered through building a boxcar circuit with me. Alexander, it has been so gratifying collaborating with you over the past year attempting, mostly failing, but now also succeeding, to squeeze some interesting data out of a kagome metal.

I cannot overstate the influence of Arkady, who exerts a force on our group even from a great distance. Thank you Arkady for teaching me how to understand the ultrasound experiment, or at least trying to. The time and energy you gave to explaining groups, cuprates, and the relationship between adiabatic invariant and quantum mechanics made me a better physicist. Maybe most of all, I learned from you that *everything* is in Landau-Lifshitz if you look hard enough.

All of this science was done in the basement of Clark Hall, which would be a mess of chaos if it weren't for Bob, Jason, and the building maintenance staff. Thanks to all of you for keeping the cooling water running, getting packages out the door, and keeping the hallways looking good. Rob, thank you for being so responsive and on top of every aspect of purchasing. Other Rob, thank you for your help designing probes. I regret not taking you up on the unicycle offer, but I guess there's still a little time.

This project would not have been possible without the material and intellectual input from many collaborators. Young-June Kim's group, especially Zeke, thank you for tirelessly growing us ruthenium chloride crystals to match our impossible standards. Much of the theoretical understanding of our results would not have come as easily without discussions with Louis Taillefer, Stephen Winter, Roser Vallenti, and Leon Balents. I also feel lucky to have participated in the CIFAR schools and meetings, which exposed me to many new people and ideas in an exceptionally collegial environment.

Though I spent what was certainly an unhealthy amount of time in the lab, probably because I spent what was certainly an unhealthy amount of time in the lab, I would not have made it through graduate school without the support of family and friends in the real world. My parents have been a never ending source of encouragement, particularly so during my first rocky years in Ithaca. Talya, you're the best, period, even if you believe in the promise of quantum computers.

My time at Cornell would have been much less spicy had it not been for Jacob, who taught me to lead trad. Turns out there's a long line of Cornell physicists who made a mark in the Gunks. Not that I even remotely count myself among them, but who knew? Gaurav, thank you for your limitless optimism and fantastic cooking. Namitha, somehow we made it through.

Lastly, Xinyu thank you for being such a wonderful partner through the ups and downs. Thank you for listening to all my rants and bearing with me through some sleepless weeks. Thank you for sharing Wasson, the king of my heart, and Sherlock, who is also a good boy. These past three years were so much brighter because of you. And we also learned how to speak cat. Well almost.

Contents

Biographical Sketch **i**

Acknowledgments **iii**

List of Figures **ix**

1 Introduction **1**
- 1.1 For everyone 1
- 1.2 For the condensed matter physicist 2
- 1.3 Thermal Hall effect of insulators - review of the data 6
  - 1.3.1 The beginning: phonons in a dielectric 6
  - 1.3.2 Magnons and spin liquids 7
  - 1.3.3 Cuprates and the return of phonons 10
  - 1.3.4 Summing up experiments 13
- 1.4 Phonon Hall effect - brief review of theoretical perspectives . 13
  - 1.4.1 Orientation – anomalous Hall effect in metals 14
    - 1.4.1.1 General considerations 14
    - 1.4.1.2 Intrinsic anomalous Hall effect 15
    - 1.4.1.3 Side-jump scattering 16
    - 1.4.1.4 Skew scattering 17
  - 1.4.2 Anomalous thermal transport 20
    - 1.4.2.1 General considerations 20
    - 1.4.2.2 Skew scattering 21
    - 1.4.2.3 Side-jump scattering 23
    - 1.4.2.4 Intrinsic phonon Hall effect 24
  - 1.4.3 Summing up theories 31

2 The Experiment 33
2.1 Measuring the intrinsic Hall effect 33
2.2 Conceptual Background 34
2.2.1 The elastic tensor: basics 34
2.2.2 The elastic tensor: decomposition 36
2.2.3 Elastic dynamics 43
2.3 Pulse Echo Ultrasound - Hardware 46
2.3.1 Overview of the method 46
2.3.2 The transducer 49
2.3.3 ZnO (on tilt) 54
2.3.4 Growth 55
2.3.5 Sample preparation 58
2.3.6 Electronics 60
2.4 Pulse Echo Ultrasound - Software 62
2.4.1 Data processing 64
2.4.2 Speed of sound and attenuation 65
2.4.3 Extracting the Hall viscosity 68

3 Hall viscosity and the Acoustic Faraday effect of YIG 70
3.1 Introduction 70
3.2 Ultrasound Data 73
3.3 Kittel model 82
3.4 Fitting YIG to the Kittel model 86
3.5 Hall viscosity in the Kittel model 89
3.6 Thermal Hall effect of YIG 91
3.7 Viscosity to phonon Berry curvature 96
3.8 Thermal Hall conductivity – comparison with a simple model 99
3.9 Wrapping up and Next steps 103

4 Hall viscosity of α-RuCl$_3$ 105
4.1 Introduction 106
4.2 Results 107
4.2.1 Measuring the acoustic Faraday effect 107
4.2.2 The acoustic Faraday effect of α-RuCl$_3$ for $B||c$ 111
4.2.3 Extracting the Hall viscosity of α-RuCl$_3$ 113
4.2.4 Comparison to the thermal Hall effect 114
4.3 Discussion 117

4.4 Heat flux in the presence of Hall viscosity: semiclassical estimate of the thermal Hall conductivity 120

Bibliography **123**

List of Figures

1.1 Phase diagrams of the hole-doped cuprates and α-RuCl$_3$ . . 3
1.2 Illustration of the thermal Hall effect measurement 4
1.3 Thermal Hall conductivity in dielectric terbium gallate and ferromagnet $Lu_2V_2O_7$ 8
1.4 Thermal Hall conductivity of α-RuCl$_3$and lanthanum cuprate 11
1.5 Summary of contributions to the anomalous Hall effect. . . . 15
1.6 Summary of the relationship between magnetoelastic coupling, Hall viscosity, phonon Berry curvature, and the acoustic Faraday and thermal Hall effects 29

2.1 Decomposition of the elastic tensor into real/imaginary and symmetric/antisymmetric parts 38
2.2 Schematic of the pulse echo experiment in reflection and transmission modes 47
2.3 Calculated electrical impedance of the piezoelectric transducer 53
2.4 The relative amount of shear and compressional stress generated by the thin film ZnO transducer as a function of the tilt angle of the piezoelectric c-axis from the sample normal . 56
2.5 Zinc oxide transducer fabrication: material stack and SEM image of the transducer cross section 57
2.6 Pulse echo measurement circuit 61
2.7 Raw and processed data in the pulse echo experiment – echo train, single echo, and the amplitude and phase after digital lockin 63

3.1 Unit cell of YIG 71

3.2 Magnetic properties of YIG: magnetization versus temperature and the magnon dispersion 72
3.3 Prepartion of the [100 74
3.4 Acoustic Faraday rotatation of YIG, frequency dependence and amplitude of the reflected echo as a function of applied magnetic field along [100 76
3.5 Illustration of the transducer polarization misalignment and magnetic field antisymmetrization used for detecting the acoustic Faraday rotation in transmission mode 78
3.6 The acoustic Faraday effect of YIG measured in transmission mode and confirming the time-odd nature of the polarization rotation 79
3.7 Full echo patterns of YIG symmetrized and antisymmetrized in applied magnetic field 80
3.8 Reversal of the antisymmetric Faraday signal on reversal of the ultrasound propagation direction 81
3.9 Numerical solution of the Kittel model, dispersion of the hybrid magnon and phonon and the Faraday rotation angle versus frequency 84
3.10 Fits of the acoustic Faraday rotation of YIG to the Kittel model 89
3.11 Temperature dependence of the longitudinal magnetothermal conductivity of YIG 93
3.12 Thermal Hall conductivity of YIG 94
3.13 Comparison of the Hall angle of a variety of insulating magnetic oxides 95
3.14 Calculation of the thermal Hall conductivity of YIG using the phonon Berry curvature and a semiclassical model . . . 102

4.1 Cartoon of the thermal Hall and acoustic Faraday effects and their relationship through the phonon Hall viscosity . . 108
4.2 Experimental geometry and ultrasound characterization in the ultrasound measurement of α-RuCl$_3$ 110
4.3 Summary of the measurement suite used to isolate the acoustic Faraday rotation of α-RuCl$_3$ 112
4.4 Value of the phonon Hall viscosity of α-RuCl$_3$extracted from the acoustic Faraday data using a wave equation 115

4.5 Temperature and magnetic field dependence of the phonon Hall viscosity and comparison with the thermal Hall conductivity 118

Chapter 1

Introduction

1.1 For everyone

Thermal conduction is one of the most intuitive ideas in physics. We all know the feeling of heat leaving our body on a cold day. We've all seen ice melt into a puddle in the sun. The basic idea is simple: hot things get colder and cold things get hotter. Temperatures tend to even out as heat moves between objects – we all know that.

This intuition, however, leaves many questions unanswered. How, exactly, does "heat energy" (whatever that means) move from place to place? Why do some objects seem to hold heat in while others allow heat to move around easily? The answers to these questions go incredibly deep and, in addition to having real-world applications, the fundamentals of such seemingly simple questions continue to occupy materials physicists.

It turns out that a very useful framework for answering these questions starts with specifying exactly what we mean when we say an object is at a particular temperature. A decent working definition is that temperature is the amount of microscopic movement occurring inside a material, where the hotter an object is, the more its constituent parts jostle around. Thermal conduction is the diffusion of these microscopic movements within and between objects. The study of thermal conduction, then, boils down to asking what all this microscopic movement looks like: what, exactly, is moving (atoms? electrons?) and how do these moving entities respond to their environment?

The work presented here focuses on the thermal motion of nuclei, formally known as phonons, commonly known as sound waves. All materials have nuclei, and so all materials move heat around via sound waves. Despite their simplicity, sound waves still seem full of surprises. This work will focus on the developing understanding, often hotly contested, of the ways in which sound waves interact with magnetism to carry heat in unexpected ways.

1.2 For the condensed matter physicist

Many phase transitions are obvious. Obvious in the sense that the order parameter – the object that defines the phase – couples strongly to some common experimental probe. The magnetic moment of a ferromagnet couples to magnetic field. [1] The ratio of lattice constants, which can be measured with x-rays, changes across a structural phase transition. [2, 3] Similarly, phases defined without reference to an order parameter may be identified by the spectroscopic signatures of their excitations. The Fermi liquid is defined by sharp, long-lived quasiparticles which can be detected by angle-resolved photoemission spectroscopy. [4, 5]

Examples exist, however, where the defining feature of a phase is "hidden" from conventional probes. Two particularly beautiful and much-studied examples are the pseudogap phase of hole-doped cuprates and the spin liquid phase of frustrated magnets. [6, 7, 8] [9, 10] In both cases it is difficult to probe the phase directly, either because the order parameter is unknown (the pseudogap) or because the excitations are challenging to detect with existing experimental probes (the spin liquid). Despite years of study, the pseudogap is poorly understood and there is no definitive evidence that a spin liquid exists. Understanding these phases is a pressing problem in condensed matter physics of both fundamental scientific interest and with potential technological applications.

When the order parameter is unknown or difficult to address, indirect probes are necessary. To obtain a better understanding of these phases, transport experiments are some of the most informative and straightforward to perform. Transport measurements provide information about a system's mobile excitations: Quantum oscillations in resistivity reveal Fermi surface geometry. [11] The current-phase relation of a Josephson junction probes the superconducting Cooper pairs on either side of the device. [12] Thermal transport measurements give information about a crys-

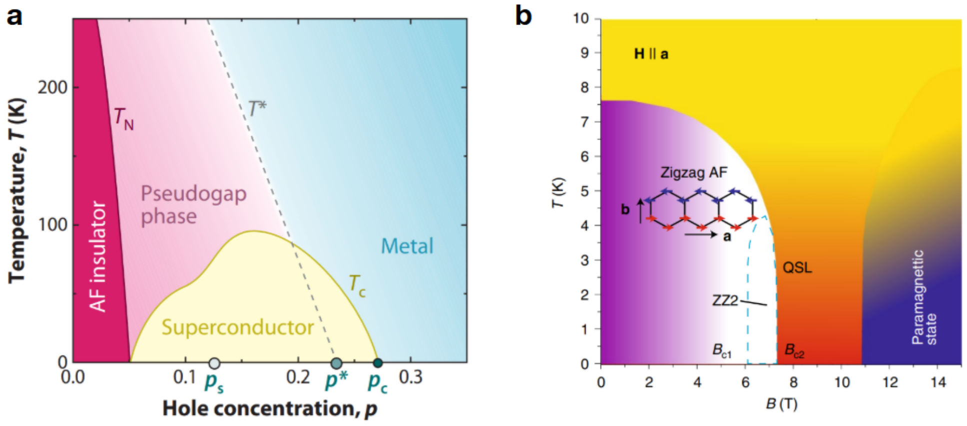

Figure 1.1: **Understanding phases of matter:** Phase diagrams of the hole doped cuprates (panel **a**) and the frustrated magnet α-RuCl$_3$(panel **b**). Though the pseudogap is thought to be a distinct thermodynamic phase, the order parameter and its relationship to high temperature superconductivity is not understood. Frustrated magnets are known, theoretically, to be favorable enviroments for exotic states like the spin ice or quantum spin liquid. Despite years of searching, there is not yet definitive evidence for the physical realization of a spin liquid.

tal's mobile heat carriers. [13, 14] In this way, transport experiments provide valuable insight into a system's quasiparticles and its ground state.

The results of a transport experiment are sometimes definitive, and one of the most striking examples of insight from transport is the discovery of the fractional quantum Hall effect. At low temperature, the Hall resistance of a gallium arsenide two-dimensional electron gas measured as a function of perpendicular applied magnetic field exhibits a series of plateaus. [15] These plateaus track the system entering a series of fractional quantum Hall states. [16] Remarkably, the value of the Hall resistance at each plateau unambiguously identifies the system's ground state at that value of applied magnetic field.

Interpreting transport measurements, however, is rarely so straightforward and is more often complicated by details of modeling or the experimental setup. For example, Josephson tunneling measurements in the

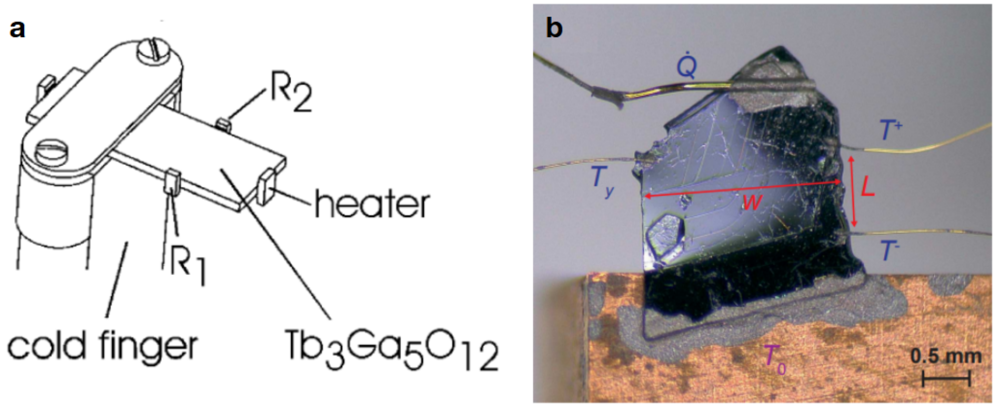

Figure 1.2: **Thermal Hall effect:** Transport experiments such as measurements of the thermal Hall effect are powerful probes of an insulating system's quasiparticles. (**a**) illustrates the cannonical experimental setup: a sample is clamped to a heat bath (cold finger) and a heater is attached to the opposite end. The entire mount is made of electrically insulating material to avoid contamination by the thermal Hall effect of electrons in a metallic mount. Opposing thermometers measure the development of a transverse temperature gradient in the presence of an applied magnetic field. (**b**) shows a sample of α-$RuCl_3$ ready for measurement. The heat sink, in this case, is made of copper and the thermometer contacts and thermal link between the sample and heat sink are made with silver paint.

unconventional superconductor Sr_2RuO_4 were put forward as strong evidence of an odd-parity superconducting state. [17] Subsequent NMR and ultrasound experiments called this interpretation into question. [18, 19] Despite the apparent simplicity of the experiment, it is likely that the details of scattering off the tunneling barrier complicate the original analysis. [20] The microscopic details of transport processes are non-trivial and can qualitatively reframe the interpretation of the data.

With this in mind, we turn our attention to a relatively new transport technique that has direct relevance to both the pseudogap and the spin liquid: the thermal Hall effect of insulators.[21, 22] The thermal Hall effect describes a transverse temperature gradient that develops when heat flows perpendicular to an applied magnetic field. It is exactly analogous to the electrical Hall effect on substituting heat current for electrical current and temperature difference for voltage drop. As such, it promises to give similarly rich information about exotic insulating systems, where electrical transport cannot be performed. The difficulties in understanding the data will fall somewhere between the fractional quantum Hall effect in GaAs and the parity of the order parameter in Sr_2RuO_4.

One of the primary complications in interpreting these measurements is that, unlike electrical transport where only mobile electrons participate, in a thermal experiment heat conduction has many sources. Phonons, magnons, spinons, polarons – anything with dispersion can play a role. As we will see later, this presents both experimental and theoretical challenges. Lattice vibrations in particular, which are always present, are a significant unsolved problem in the thermal Hall effect. In short, thermal transport sees too much, and is agnostic to which heat carrier is responsible for the thermal Hall signal.

A second, more subtle unresolved issue is whether, in a given experiment, the process that generates a thermal Hall effect is intrinsic or extrinsic. By intrinsic we mean that the magnitude of the effect is independent of the mean free path of the heat carrier, resulting, for example, from the band structure of the heat carrier. In contrast, an extrinsic Hall effect depends on the mean free path and is generally the result of a scattering process. In principle experiments that systematically tune the scattering rate could disentangle these contributions. In practice, though some examples exist, "tuning disorder" is laborious and difficult to achieve quantitatively. [23, 24, 25] The issue is further complicated by the fact that both mechanisms can be present simultaneously.

In light of these complications, this thesis presents an ultrasonic measurement to complement thermal Hall experiments. We propose the acoustic Faraday effect as a probe of phonon Hall viscosity, and therefore of the intrinsic phonon contribution to the thermal Hall conductivity. This chapter reviews the literature of the thermal Hall effect in insulating materials and outlines the possible role of phonon Hall viscosity. The following chapter presents our experimental method, pulse echo ultrasound, in a broader context. We then present our protocol for measuring the acoustic Faraday effect using the model system YIG, a relatively simple magnetic insulator. The final chapter summarizes our measurements of the phonon

Hall viscosity in the purported spin liquid α-RuCl$_3$.

The thermal Hall effect is a unique and powerful window into unconventional phases of matter. It appeared to unambiguously identify α-RuCl$_3$ as a spin liquid. It pointed to a unifying physics underlying the pseudogap phase of cuprates. However, as we've hinted at above, thermal transport has limitations. The ultrasound experiments presented here aim to add specificity to the information contained in thermal transport data. The experimental protocol sheds light on a fundamental but difficult to measure aspect of phonons, their Hall viscosity, and sharpens our understanding of unconventional phases of matter more generally.

1.3 Thermal Hall effect of insulators - review of the data

1.3.1 The beginning: phonons in a dielectric

The electrical Hall effect is well-understood. [26] In the presence of a magnetic field the Lorentz force bends electron trajectories, resulting in transverse heat and charge currents. In insulating systems, it is not obvious how a Hall current is generated – what couples charge neutral objects to a magnetic field? Despite an apparent lack of intuitive motivation, the study of the thermal Hall effect in insulating crystals is decades old. Here, we briefly review the experimental data and their evolving interpretations, focusing on magnetic oxides.

For the reasons mentioned above, attempting to measure the thermal Hall effect in an insulator is not clearly motivated. The initial observation of a phonon Hall effect by Strohm et al. was inspired by analogy to the behavior of light. [27] In the presence of an applied magnetic field, the proper description of electromagnetic radiation is in terms of left and right circular waves. A theoretical proposal and follow-up experimental work (carried out ten years before observation of the phonon Hall effect) showed that, despite being electrically neutral, left and right hand polarized light waves in a scattering medium can exhibit different scattering rates.[28, 29] By an intuitive leap, Strohm et al. posited the existence of the thermal Hall effect of phonons.

The cartoon reasoning is simple: if an excitation is described by left and right hand polarizations whose energy splitting and scattering rate is controlled by an applied magnetic field, energy will diffuse with a preferential handedness. The splitting of circular polarized light waves by a magnetic field is well-established. The analogous splitting of transverse sound waves, referred to as the acoustic Faraday effect, is less well-known, but was also predicted (Kittel, 1958) and experimentally measured (Matthews, 1960). [30, 31] In other words, the dispersion of the circular polarized acoustic modes can be controlled and split by a magnetic field. Generically, then, the circular polarized modes will have different scattering rates and generate a phonon Hall effect.

This intuition motivated the measurement of the phonon Hall effect in terbium gallate, a paramagnetic insulating dielectric. FIG XXXXa shows the experimental configuration. In the experiment they attach two resistive RuOX thermometers to opposite faces of a thin plate of terbium gallate. The sample is attached to an insulating LiF heat bath on a nonmetallic mount to avoid contamination of the thermal Hall effect of electrons in the surrounding material. A thin-film heater is attached opposite the heat bath by which a heat current is passed perpendicular to the two thermometers. This experimental arrangement, with some small but important modifications, remains the standard steady-state DC technique.

FIG XXXb shows the difference in resistance between the two sample thermometers as a function of applied magnetic field. To extract the phonon Hall conductivity, they antisymmetrize the resistance difference in applied magnetic field. When the magnetic field is applied perpendicular to the heat current they find an antisymmetric temperature gradient that grows linearly with applied magnetic field. The temperature gradient is linear in applied thermal power and the antisymmmetric gradient vanishes when the magnetic field is directed parallel to the heat current. They extract the thermal Hall angle of terbium gallate, $\theta_H = 4 \cdot 10^{-4}$ at 5.45 K and 4 T.

1.3.2 Magnons and spin liquids

The Hall effect of phonons received little attention and no direct follow-up experiments were done after Strohm. Instead, motivated by the experimental detection of the spin Hall effect, Onose et al. observed a thermal Hall effect in the insulating ferromagnet $Lu_2V_2O_7$. [32] FIG XXXXa

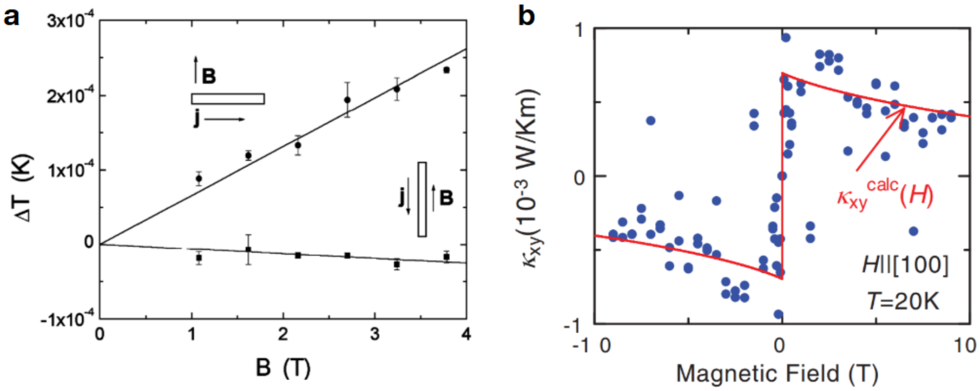

Figure 1.3: **Thermal hall effect of phonons and magnons:** The initial measurements of the thermal Hall effect of insulators were performed on terbium gallium garnet, a paramagnetic dielectric. (**a**) shows the antisymmetric in magnetic field transverse temperature gradient across the sample with the magnetic field applied perpendicular and parallel to the heat current. A gradient above the noise level appears when the applied magnetic field is perpendicular to the sample, implying a non-zero thermal Hall conductivity. (**b**) shows the thermal Hall conductivity of $Lu_2V_2O_7$, an insulating ferromagnet, as a function of applied magnetic field. Note that here, the thermal Hall conductivity is in not linear in magnetic field, but rather resembles the field dependence of the anomalous electrical Hall conductivity. The data are well-describesd by a theoretical model of the thermal Hall effect due to magnons, plotted as a red solid line.

shows the thermal Hall conductivity of $Lu_2V_2O_7$ as a function of applied magnetic field at 10 K. These data are qualitatively different from those in paramagnetic terbium gallate. Instead of a linear in applied magnetic field effect, Onose et al. observe a rapid increase in the thermal Hall conductivity starting from zero applied magnetic field, after which the effect reaches a maximum and decays in the high-field limit. In addition to the non-monotonic magnetic field dependence, the the thermal Hall conductivity was found to onset at the Curie temperature. These features in the data are reminiscent of the anomalous electrical Hall effect in itinerant magnets and suggested new ways of understanding the Hall effect of insulators.

For this reason, the theoretical machinery used to understand the anomalous Hall effect in metals was adapted to the magnon Hall effect in insulating systems. In particular, the language of Berry curvature of the heat carrying quasiparticles augmented the notions of diffusivity and angular momentum employed in the initial work on the phonon Hall effect. Building off work done to understand the electrical Hall effect in the cuprate superconductors, Lee et al. calculated the intrinsic thermal Hall conductivity of an ordered magnet and of the spin liquid. [33] Theory presented alongside the data on $Lu_2V_2O_7$ also quantitatively understood the effect in terms of the Berry curvature of the magnons, and was further developed by Matsumoto. [34]

The discovery of the magnon Hall effect and its interpretation in terms of Berry curvature suggested that the thermal Hall effect of insulators could be used to look for new phases of matter. In particular, concurrent interest in spin liquids gave rise to the idea of using the thermal Hall effect as a screening tool for candidate materials. In this context, experiments were focused on frustrated magnets, of which $Tb_2Ti_2O_7$ and α-$RuCl_3$ received particular attention.

$Tb_2Ti_2O_7$ is an insulating pyrochlore which, despite having large-moment, magnetically active ions and Curier-Weiss temperature of -19 K, does not display magnetic order to the lowest experimentally accessible temperatures. [35, 36] The frustrated magnetism and complex, short-range spin correlations at low temperature gave some weight to the idea that $Tb_2Ti_2O_7$ belongs to the class of spin ices. [37, 38] Remarkably, Hirschberger et al. measured a large thermal Hall conductivity in $Tb_2Ti_2O_7$. [39] Though not immediately indicative of a spin liquid ground state, the result demonstrated the existence of a thermal Hall effect in a material with no well-developed magnons. Further, Hirschberger et al. argue that, based on the range of magnetic fields and temperatures in which the thermal Hall effect is observed, phonons alone cannot be the transverse heat carriers.

A similar story, though at a higher register of excitement, played out in α-$RuCl_3$, a layered honeycomb structure with zig-zag antiferromagnetic order onsetting at $T_N = 7$ K. [40, 41] Despite the presence of magnetic order, theoretical models predicted a spin liquid phase on suppression of magnetic order by an in-plane applied magnetic field. [42] Indeed, the continuum of low-energy excitations observed in neutron scattering and an anomalous, non-saturating magnetization in large applied magnetic field were difficult to understand in terms of conventional magnons. [43, 44, 45]

The spin liquid phase of α-$RuCl_3$ was predicted to host fermionic Majorana edge modes with a quantized thermal Hall conductivity (in direct analogy to the conducting edge modes of the bulk-insulating quantum Hall state). [46] In this context, a quantized thermal Hall conductivity measured just above the critical magnetic field of 7 T was, on its face, the first definitive proof of a spin liquid. [21] The initial experiment was done with the applied magnetic field tilted out of the honeycomb planes. A followup experiment by the same group showed quantization with the magnetic field applied entirely in the honeycomb plane, the so-called planar Hall effect. [47] Breaking briefly with chronology, it is worth noting that subsequent experiments by other groups failed to observe quantization. Work by Czajka et al. found a similar magnitude of the planar Hall conductivity but without quantization. [48]

1.3.3 Cuprates and the return of phonons

This is the point in the story where things get really messy. Putting aside for a moment whether α-$RuCl_3$ is a spin liquid and what the thermal transport data mean, we turn to an experiment done in an entirely different class of materials. Grissonnanche et al. measured the thermal Hall conductivity in the underdoped high-temperature cuprate superconductors. [22] They found a large thermal Hall effect across the underdoped series extending from the insulating parent compound, La_2CuO_4, where the effect was largest, and vanishing at the end of pseudogap. These data were particularly significant because they implied that the physics generating the thermal Hall conductivity was confined to the pseudogap but also present in the undoped compounds, pointing to a unifying physics of the entire phase.

A companion study showed that, despite being high anistropic in their magnetic and electronic properties, the thermal Hall effect of cuprates is remarkably isotropic. [49] The heat carrying excitations that are most isotropic in these cuprates are their lattice vibrations. Further, the temperature dependence of the thermal Halll conductivity follows the tempera-

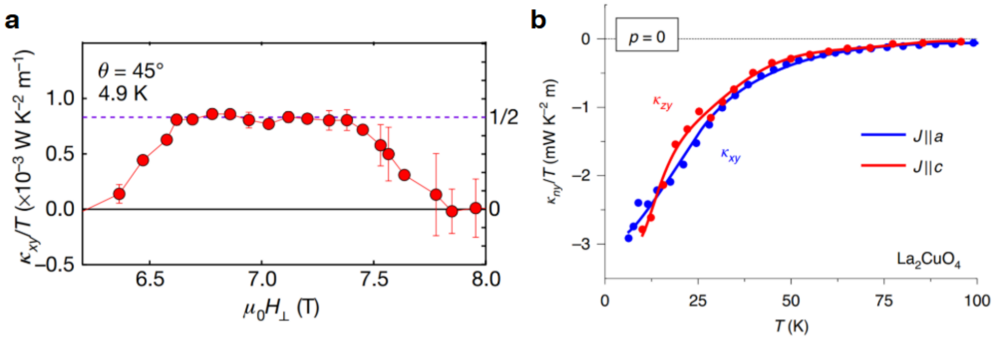

Figure 1.4: **Thermal hall effect of Majoranas and phonons:** In a spin liquid, transverse heat current may be carried by Majorana fermions, resulting in a quantized thermal Hall conductivity. (**a**) shows the magnetic field dependence of the thermal Hall conductivity of spin liquid candidate α-RuCl$_3$. A plateau is observed as a function of applied magnetic field over a range of approximately 1 T, near the region of the phase diagram in which antiferromagnetic order is destroyed (see Figure 1.1). This result generated great excitement, as the magnitude of κ_{xy} at the plateau matches the quantized value predicted for a spin liquid. However, the result proved difficult to reproduce. The thermal Hall effect of underdoped cuprates was investigated as a defining feature of the pseudogap phase. (**b**) shows the temperature dependence of the thermal Hall conductivity of insulating La$_2$CuO$_4$, the parent compound of the lanthanum cuprate series, for two directions of applied heat current. The nearly identical value of κ_{xy}, despite the highly anisotropic nature of the layered cuprate, suggests the heat carriers are long wavelength phonons.

ture dependence of the longitudinal thermal conductivity, suggesting that the same heat carriers are dominant in both channels. Therefore, the authors conclude that the thermal Hall effect of insulating cuprates is due to phonons.

The observation of the thermal Hall effect in insulating cuprates, combined with a nearly simultaneous report of a thermal Hall effect in insulating, non-magnetic $SrTiO_3$, catapulted phonons back onto the thermal stage. [50] In large part due to the magnitude of the effect in terbium gallate, phonons were dismissed as a major contributor in later experiments where a much larger absolute value of thermal Hall conductivity and Hall angle were detected. The experimental results in cuprates, which were soon extended to other insulating parent compounds, strontium titanate, and the antiferromagnetic insulator Cu_3TeO_6 were presented as evidence that phonons alone can generate a significant thermal Hall effect. [51, 52]

Taken together, these data suggested a major shift in how we understand the thermal Hall measurements in other insulators. Phonons are present in every crystal lattice. If phonons are generically capable of producing a thermal Hall effect, then any measurement of the thermal Hall conductivity is potentially riding on a background phonons contribution. This is problematic in the interpretation of a quantized thermal Hall effect, especially in the case where the value of the thermal Hall conductivity has direct bearing on the result. Indeed, Lefrancois et al found that α-$RuCl_3$ exhibits a thermal Hall effect over a range of temperatures and applied magnetic fields extending far beyond the purported spin liquid regime. The suggestion is that in α-$RuCl_3$ as well, the phonon Hall effect plays a non-negligible role.

At the risk of sounding overly dramatic, amid all these developments the study of the thermal Hall effect of insulators entered its late Roman period. An ever-expanding list of insulators exhibits a thermal Hall effect. Iridates, pyrochlores, black phosphorus. [25, 53, 54] More recently, even silicon, germanium, silicon dioxide. [55] It is beyond the scope of this document to examine all these data in detail. The underlying message, however, is that there may be something fundamental to phonons – theoretically, or experimentally – whose importance has not yet been recognized.

1.3.4 Summing up experiments

This account of the thermal Hall effect of insulators is incomplete; however, we see the overall progression of experimental focus. The phonon Hall effect was originally conjectured and experimentally demonstrated in a paramagnetic dielectric. The conceptual understanding was of the anisotropic diffusion of magnetic field-split left and right handed modes. The magnon Hall effect revived the idea of the Hall effect of charge-neutral excitations, now understood in the language of the anomalous Hall effect in metals. Ideas in topology, namely quantized Berry curvature, led to proposals that the thermal Hall effect could be used to identify exotic phases of matter such as the spin liquid. This gave way to the study of spin liquid candidates $Tb_2Ti_2O_7$ and α-$RuCl_3$. As a probe of exotic excitations more generally, the thermal Hall experiment was conducted in underdoped cuprates, leading the community back to the idea of a phonon Hall effect.

We have come full circle. There is no obvious mechanism for the thermal Hall effect in insulators, yet it seems ubiquitous. Magnons, phonons, spinons have all been put forward as the heat carriers of the thermal Hall effect and, as noted previously, the thermal transport experiment cannot distinguish these contributions directly. So even this most basic question – what carries the heat energy? – remains unanswered. A major open question is the role of phonons and, in the following section, we will examine in more detail some theories of the phonon Hall effect and how the proposed mechanism might be disentangled experimentally. This will bring us to the Hall viscosity of phonons and acoustic Faraday rotation measurements developed later.

1.4 Phonon Hall effect - brief review of theoretical perspectives

Broadly speaking, modern treatments of the phonon Hall effect are rooted concentually in theories of the anomalous Hall effect in metals. [56, 57] Both are anomalous because they appear in the absence of an external Lorentz force. Because of this parallel development, we will first review the sources of the electrical Hall effect, then port these ideas into the language of thermal transport. The literature of theories of the anomalous

Hall effect is vast and this account will be sparse: decades of experimental work on the "extraordinary" Hall effect of magnetic systems (1881) preceeded the development of a microscopic theory from Karplus and Luttinger (1954), and many more decades passed until the field seemed settled enough to warrant a review (2010). We present only the essential ideas (without reference to experiment) and how they appear in a semiclassical Boltzmann theory of the Hall effect. For the reaminder of this section "Hall effect" will be used to refer to either the electrical or phonon analog, or both, depending on context.

1.4.1 Orientation – anomalous Hall effect in metals

1.4.1.1 General considerations

Sources of a Hall effect are often divided between intrinsic contributions, which would be present even in a detect-free crystal, and extrinsic contributions, which rely on scattering. Extrinsic contributions are classified by their dependence on the scattering rate, assuming that the scattering potential is weak and can be treated perturbatively. The simple treatment we will pursue here also assumes different scattering mechanisms do not "talk" to each other (are statistically independent and do not coherently interfere with each other). Many of the scaling laws relating the underlying mechanisms to the resulting conductivities also break down when the assumption of isotropic scattering is dropped. All of this will become important when we return to the thermal Hall effect of insulators.

We use the Boltzmann formalism to organize these contributions. The Boltzmann equation is a means of calculating transport coefficients by finding the deviation of the particle distribution function due to a driving field. The deviation of the distribution function is found by requiring that, in steady state, the distribution shift due to the driving field be balanced by scattering. For electrons in a uniform electric field the distribution function, f, is a function of momentum only, and the stady state solution satisfies

$$\dot{\mathbf{k}}\frac{\partial f}{\partial \mathbf{k}} = \left(\frac{\partial f}{\partial t}\right)_{coll}, \tag{1.1}$$

where $(\partial f/\partial t)_{coll}$ is the time derivative of the distribution function due to all sources of scattering. This provides the simplest conceptual division:

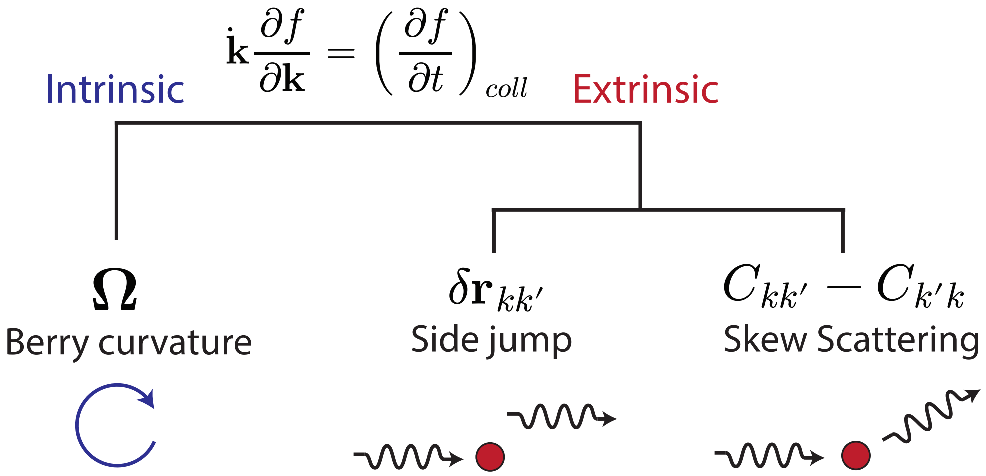

Figure 1.5: **Summary of contributions to the anomalous Hall effect:** Contributions to the anomalous Hall effect can be organized according to whether they depend on or are independent of scattering. Intrinsic contributions, such as those due to Berry curvature, are independent of scattering are incorporated directly into the semiclassical equations of motion. Extrinsic contributions depend on scattering are can be divided into two classes. Skew scattering describes a scattering cross section that is antisymmetric in incoming and outgoing states. The side jump contribution arises when the incident quasiparticle experiences a transverse shift in real space during the scattering process.

intrinsic contributions live on the left hand side, and extrinsic contributions live on the right hand side of Equation 1.1.

1.4.1.2 Intrinsic anomalous Hall effect

First, we deal with the intrinsic contribution. Despite more recent abstraction into topological invariants, the original formulation of the intrinsic Hall effect was motivated by a very simple observation. In the Fermi liquid, we exploit the periodicity of the lattice to write the electron states as Bloch wavefunctions. However, in the presence of a static electric field the periodicity of the lattice is spoiled by the electrical potential. This means the Bloch states are no longer eigenstates of the system and the electric field mixes states in different bands. [58, 59] Karplus and Luttinger noted that the interband matrix elements with the electric potential, in combination with spin-orbit coupling, leads to a transverse, Hall current. [60]

To briefly make contact with the Berry curvature, $\mathbf{\Omega}$, note that the first order correction to the Bloch wavefunction, $|\delta u_n\rangle$, on the n-th band due to the electric potentaial $e\mathbf{E} \cdot \mathbf{r}$ is

$$|\delta u_n\rangle = e\mathbf{E} \cdot \sum_{m \neq n} \frac{\langle u_n| \mathbf{r} |u_m\rangle}{E_n - E_m} |u_m\rangle = ie\mathbf{E} \cdot \sum_{m \neq n} \frac{\langle u_n| \partial_{\mathbf{k}} |u_m\rangle}{E_n - E_m} |u_m\rangle . \tag{1.2}$$

In addition, the correction to the velocity $\hat{v} = \partial H / \partial \mathbf{k}$ is proportional to the real part of $\langle u_n| \hat{v} |\delta u_n\rangle$. Using the Schrodinger equation and the orthonormality of the Bloch states, we also have $\langle u_n| \partial_{\mathbf{k}} |u_m\rangle = \langle u_n| \partial H / \partial_{\mathbf{k}} |u_m\rangle / (E_n - E_m)$ and, inserting Equation 1.2 into the correction to the velocity, we get the anomalous velocity in terms of the Berry curvature $\hat{v} \sim \mathbf{E} \times \mathbf{\Omega}$.

A more formal incorporation of the Berry curvature into the semiclassical equation of motion is derived in many places. [61] The result is the same as the abbreviated analysis above and consequently, the charge current in the Boltzmann picture must include this extra “anomalous” term. Starting from the band mixing picture gives a pretty wild picture of the anomalous velocity as originating from a fast oscillation of the Bloch states between bands as the wave packet propagates. The phase structure on the bands, their Berry curvature, is converted to sideways motion through rapid transitions driven by the electric field.

1.4.1.3 Side-jump scattering

The extrinsic Hall conductivity, by definition *requires* scattering. However, completely counter to intuition, the so-called side-jump contribution is independent of scattering rate and arises in the following way. A scattering event takes an incoming state with momentum $\mathbf{k}$ and transfers it to an outgoing state with momentum $\mathbf{k}'$. One can notice that, naively, the scattering event also changes the expectation value of the Bloch state in real space, $\langle u_k| i\partial_{\mathbf{k}} |u_k\rangle$. Of course the Bloch states are not localized in real space, but this idea applied to a wave packet is the basic intuition for the side jump process: the movement of charge jumps in real space as well as momentum space during a scattering event. Problems related to gauge invariance and what exactly is meant by "the phase evolution of the wavepacket during scattering" were clarified relatively late, and are discussed by Sinitsyn. [62]

The fact that the side-jump contribution to the Hall conductivity is independent of scattering rate comes from the fact that, though the transverse current generated by side-jump events is proportional to the scattering rate, the frequency of these events at fixed longitudinal driving field is inversely proportional to the scattering rate. So more scattering more side-jump, but simultaneously, more scattering less current. These two effects exacltly cancel and the side-jump Hall conductivity is extrinsic but independent of scattering rate. Alternatively, consider the side-jump Hall angle which decreases as τ increases. But $\sigma_{xx} \sim \tau$, so σ_{xy} does not depend on the scattering rate.

In effect, the side-jump process rides on top of other scattering events. It does not describe a change in the distribution function directly, but is a side effect of changes to the distribution function. For this reason side-jump scattering is somewhat awkward to incorporate into the Boltzmann theory. The standard treatment is given by Sinitsyn. [62] Because both the side jump and intrinsic contributions to the Hall conductivity do not depend on the scattering rate, disentangling the two through transport experiments is especially difficult. This highlights the importance of developing more direct probes of the Berry curvature.

1.4.1.4 Skew scattering

Lastly, we come to the extrinsic skew, or antisymmetric, scattering. The importance of skew scattering was initially overlooked because, in the Born approximation of the Fermi golden rule, scattering between $|n\rangle$ and $|m\rangle$ is determined by the square of the matrix element with the potential $|\langle n| V |m\rangle|^2$ which is invariant uder the exchange $n \leftrightarrow m$. At this level of approximation, then, the scattering matrix is symmetric and cannot result in a scattering cross section that is odd in the outgoing scattering angle and generates a transverse current. (This was confusing for me, so to be exlicit: for fixed incoming $\mathbf{k}$ the cross section is the modulus square of an integral of a scalar function $f[\mathbf{k}, \mathbf{k}']$. Symmetric scattering requires that f consist only of symmetric combinations of $\mathbf{k}$ and $\mathbf{k}'$, ie $f = f[\mathbf{k} \cdot \mathbf{k}']$ which is independent of how $\mathbf{k}'$ is rotated around the direction of $\mathbf{k}$.) The skew contribution, then, must come from going beyond the Born approximation and including higher powers of the potential in the scattering matrix.

But how does the antisymmetric scatering occur? The mechanism of skew scattering is most concretely understood by the example of spin orbit coupling where we imagine a central impurity potential, $V(r)$, that couples to electrons via $\lambda\mathbf{S}\cdot(\nabla V\times\mathbf{p})$. For plane wave states this results in a $\mathbf{k}\times\mathbf{k}'$ term in scattering potential matrix element, with, say, $\mathbf{k}'$ coming from the momentum operator $\mathbf{p}$ acting on the outgoing state and $\mathbf{k}$ coming from the gradient of the potential integrated against the incoming state. This, however, is still not enough: in the Born approximation the scattering rate still geos as the modulus square of the matrix element and no skew term appears. Going "beyond" the Born approximation means the antisymmetric scattering requires, on top of a spin orbit type interaction (more generally, the system or scatterer must involve a pseudovector, $\boldsymbol{\sigma}$, to create scalars of the form $\boldsymbol{\sigma}\cdot(\mathbf{k}\times\mathbf{k}')$), the coherent interference between states participating the scattering event. This generates terms in the scattering cross section proportional to $|V|^3(\mathbf{k}\times\mathbf{k}')$. Because the resulting scattering cross section is odd in the scattering angle, antisymmetric scattering generates a transverse current.

(Beyond beyond relevant, but it is interesting to note that the first theoretical account of the skew scattering by Smit was proposed in objection to the idea that the Hall effect was intrinsic. His reason for discarding the the intrinsic Hall effect was the assumption that it would be exactly cancelled by the effect of scattering. In modern language, he argued the side-jump would always negate the intrinsic Hall effect.)

To see the effect of the skew scattering on the Hall conductivity, we consult the Boltzmann equation. Starting with Equation 1.1, we can write the distribution function about its equilibrium, writing $f = f_0 + g$ and find the deviation to linear order in g. The Boltzmann equation now reads [63]

$$e\partial_{\mathcal{E}}f_0\mathbf{E}\cdot\mathbf{v} = \int d\mathbf{k}'\,(C_{k'k}g(\mathbf{k}) - C_{kk'}g(\mathbf{k}')) = \frac{g(\mathbf{k})}{\tau(\mathbf{k})} - \int d\mathbf{k}' C_{kk'}g(\mathbf{k}'), \tag{1.3}$$

where $C_{kk'}$ is the scattering matrix. The definition of $\tau(\mathbf{k})$ accounts for all states scattering out of $\mathbf{k}$ and the remaining integral captures states scattering into $\mathbf{k}$. We are particularly interested in the skew scattering which, as noted above, is the antisymmetric part of the scattering matrix

$$C_{sk} = \frac{1}{2}\left(C_{kk'} - C_{k'k}\right). \tag{1.4}$$

Absorbing the symmetric part of $C_{kk'}$ into $1/\tau$ defining

$$\frac{1}{\tilde{\tau}} \equiv \frac{\delta_{kk'}}{\tau(\mathbf{k}')} - \frac{1}{2}\left(C_{kk'} + C_{k'k}\right) \tag{1.5}$$

we can view the left hand side of Equation 1.3 can be thought of as a linear operator, A, acting on the distribution g

$$A_{kk'} = \frac{\delta_{kk'}}{\tau(\mathbf{k}')} - C_{kk'}, \tag{1.6}$$

which allows us to write the formal solution $g = e\partial_{\mathcal{E}} f_0 A^{-1}\mathbf{E} \cdot \mathbf{v}$ and expand A^{-1} in powers of $\tilde{\tau}$:

$$g(\mathbf{k}) \sim A^{-1} = \tilde{\tau}(\mathbf{k}) - \tilde{\tau}(\mathbf{k})C_{sk}\tilde{\tau}(\mathbf{k}') + \tilde{\tau}(\mathbf{k})C_{sk}\tilde{\tau}(\mathbf{k}')C_{sk}\tilde{\tau}(\mathbf{k}'') - ... \tag{1.7}$$

Noting that the Hall current is proportional to the distribution $f_0 + g$ times the transverse velocity, we see that the skew contribution goes as $\tilde{\tau}^2 C_{sk}$. Writing the effective skew scattering rate as a fraction of the normal scattering $C_{sk} = \alpha_{sk}/\tilde{\tau}$ we get the skew contribution to the Hall conductivity $\sigma_{xy}^{(sk)} \sim v_y/E \sim \tilde{\tau}$. The skew scattering contribution scales with the longitudinal conductivity $\sigma_{xy}^{(sk)} \sim \sigma_{xx}$.

Before moving on, it is important to note a few limitations, as given by [57], in the classfication of scattering mechanisms given above, namely division based on the Hall conductivity in powers of the scattering time. This is particularly relevant, as experimental data used to single out one mechanism over another (for electrical and phonon Hall effects) are often presented as plots of the Hall resistance versus the longitudinal resistance. First, the entire discussion deals only with elastic impurity scattering. At temperatures approaching and above the Debye temperature inelastic scattering by phonons, for exmaple, quantiatively changes the scaling between Hall conducivity and scattering rate. Second, empirically, the apparent dominance of one mechanism over another *depends on* the absolute value of the resistivity. Highly conductive materials seem to exhibit more linear dependence of σ_{xy} on σ_{xx}, less conductive materials tend to show more intrinsic scaling of the Hall conductivity, and the behavior of even worse conductors is still poorly understood (often the scaling of

ρ_{xy} with ρ_{xx} falls somewhere between 1 and 2). So the temperature dependence of the Hall conducitivty is rarely diagnostic, and the "goodness" of the conductor itself can favor one mechanism over another.

If we limit ourselves to simple impurity scattering, the formal solution Equation 1.7 along with the intrinsic and side jump corrections to the transverse velocity contains all the major contributions to the anomalous Hall conductivity. Becuase of its relative familiarity, this introduction to the terminology is presented in the language of electrons with a driving electric field. We now reframe these concepts for phonons in a thermal driving field.

1.4.2 Anomalous thermal transport

1.4.2.1 General considerations

From the perspective of Boltzmann transport the thermal conductivity of phonons is, in many respects, similar to the charge transport of electron. Because of the temperature gradient, one keeps the gradient in the distribution function, n, and we have

$$\dot{\mathbf{r}}\nabla_{\mathbf{r}}n = \dot{\mathbf{r}}\nabla_{E}n\frac{E}{T}\frac{\nabla T}{T} = \left(\frac{\partial n}{\partial t}\right)_{coll}, \tag{1.8}$$

where, again, the right hand side keeps track of collisions. The gradiant of the distribution function is converted to a temperature gradient $\nabla_{\mathbf{r}}n = \nabla T\nabla_{\mathbf{T}}n$, after which it is converted to an energy gradient. The deviation is now from the Bose distribution, $n_0(E) = 1/(\exp(E/k_BT) - 1)$, so $n = n_0 + g$. The strategy is now the same as for charge current, but we must find the energy current density

$$\mathbf{j}_Q = \int d^3\mathbf{k}E(\mathbf{k})\mathbf{v}(\mathbf{k})n. \tag{1.9}$$

The collision terms and their effect on the (phonon) Hall conductivity are the same as for the Hall effect of electrons. However, as we will see below, great care needs to be taken with the intrinsic portions of the Hall conductivity. Because of this subtlety, we will leave the discussion of the intrinsic contribution for the end, and discuss the extrnisic Hall conductivity first.

1.4.2.2 Skew scattering

Invoking skew scattering to explain the thermal Hall effect in insulators is appealing for three primary reasons. First, estimates of the intrinsic contribution tend to be orders of magnitude below the experimentally measured thermal Hall conducivity. This comes from somewhat generic arguements, but there are important exceptions which we will discuss later. Second is the experimentally measured temperature dependence of the thermal Hall conductivity. In almost every material with a sizeable κ_{xy}, the thermal Hall angle is independent of temperature over some range of temperature. Note however, that, as mentioned above, attributing a constant Hall angle to skew scattering becomes difficult at elevated temperature where the inelastic scattering is non-negligible. Additionally, the temperature dependence as $T \to 0$ is sometimes found to scale at T^4, in contrast to the T^3 dependence predicted for an intrinsic Hall effect. Lastly, the measured Hall anlge across materials falls, almost always, within an order of magnetiude of 10^{-3}. Again, a Hall angle indpendent of material details is suggestive of an extrinsic skew mechanism.

Discussions of phonon skew scattering fall into two broad catargories. In one scenario, the phonon may be "normal" but the scatterer couples to the external magnetic field and imparts handedness to the phonon transport. Alternatively, the phonon itself can already be coupled to the magnetic field (by an intrinsic mechanism, discussed later) and the impurity amplifies the effects of this coupling in transport. It's interesting to note that this almost exaclty mimics the discussion of the role of spin orbit coupling in the Hall effect of metals (see [64]: is it in the SOC of the crystal or the defect?).

Considering the phonon Hall effect in insulating oxides like terbium gallate and strontium titanate, Felbus provides an example of the first proposed scenario. [56] First, note that the Hall angle from skew scattering is constant, similar to what is observed in experiment and suggesting that the Hall effect is extrinsic. [50] They propose that the phonon Hall effect is due to oxygen vacancies surrounded by ions that carry a net charge. Scattering off the charged impurity from momentum $\mathbf{k}$ to $\mathbf{k}'$ in the presence of a magnetic field, $\mathbf{B}$, may depend on the quantity $\mathbf{B} \cdot (\mathbf{k} \times \mathbf{k}')$. The content of their argument is in estimating the dimensionless prefactor in such a term which would equal the thermal Hall angle.

They reason that the (lossy) ultrasound attenuation, η, should scale with defect scattering rate and, in addition, the degree of skewness in the process is due to the cyclotron motion of the ion and should scale with $\omega_C \sim qB/M$, where M is the ion mass and q its charge. Because they are looking for a skew effect, which involves interference between scattering channels, that is linear in the magnetic field, they need a second scattering process (independent of ω_C) to interact with the one proportional to $\mathbf{B}$. They note that symmetric scattering off these same charged defects will depend on the acousitc mismatch between the defect and the host material, being a function of the elastic moduli, C but is indepdnent of the applied magnetic field. The dimensional argument (born out by their calculation) is that the linear in magnetic field skewness is then $\omega_C\eta/C \approx 10^{-3}$, in agreement with experiment.

In contrast to the skew effect of the scatterer, theories such as those presented by Guo and Chen consider the case of phonons already coupled to the magnetic field incident on scalar scattering cites. [65, 66] The idea here is that the phonons in the host crystal already have handedness of their own, quantified by the Berry curvature, $\mathbf{\Omega}$. A scattering site that does not couple to the magnetic field then, can still generate a skew term proportional to $\mathbf{\Omega}\cdot(\mathbf{k}\times\mathbf{k}')$. Chen et al. note that, in order for the process to remain linear in magnetic field and mean free path (to maintain a fixed Hall angle), they must add the assumption of strong scattering. This allows them to bypass the Fermi rule entirely instead of invoking interference between scattering channels. Strong scattering is not unreasonable in strontium titanate, which has structural domain walls. Guo et al. retain the weak scattering assumption but find an interference mechanism that maintains a linear in scattering rate effect.

The quantitative aspect of these arguments can be captured with dimensional analysis. As will be dsicussed later, the intrinsic coupling of the phonon to a magnetic field is captured by a viscous coupling of the form $i\eta\omega k^2$, where η is a time odd Hall viscosity. To lowest order, the Berry curvature comes from the perturbations to the wave function divided by k^2 (since is comes from $\langle\partial_{\mathbf{k}}u|\,|\partial_{\mathbf{k}}\delta u\rangle$ where u and δu are the wavefunction and its first-order correction). This suggests

$$\Omega(k) \sim \frac{\eta\omega}{C}\frac{1}{k^2} = \frac{\eta v}{C}\frac{1}{k}, \tag{1.10}$$

where C is the elastic modulus (which sets the scale of the unperturbed energy), and $v = \omega/k$ is the speed of the acoustic phonon. The skew scattering rate can be writte $A\mathbf{\Omega}\cdot(\mathbf{k}\times\mathbf{k}')/\tau$, where τ is the phonon scattering time, and A set the degree of skewness. In a Boltzmann pciture then, the Hall and longitudinal conductiivties are the energy current integrated against the deviation of the distribution function due to antisymmetric and symmetric scattering, respectively. Therefor, up to constants, the Hall angle should be $\sim A\Omega k^2 = A\eta\omega/C$. For thermal phonons, the characteristic frequency is $k_BT/\hbar$ giving (again born out by the more rigorous calculation of Chen)

$$\frac{\kappa_{xy}}{\kappa_{xx}} \approx A\frac{\eta}{C}\frac{k_BT}{\hbar}. \tag{1.11}$$

Combined with the fact that $\kappa_{xx} \sim T^3$ we have $k_{xy} \sim T^4$, which matches the low temperature scaling in $SrTiO_3$. Matching the absolute value of the Hall angle to experiment relies on further assumptions about the scale of A, which we will not repeat here.

These explanations of the phonon Hall effect capture key elements of the experimental data. In particular, the magnitude of the Hall and, to some extent, the temperature dependence of the Hall conductivity. These models, however, makes key assumptions that need experimental verification. For example, an irradiation study on terbium gallate could give weight to the theory of charged impurities. Direct measurement of the flexoelectric coupling in strontium titanate would allow the arguments of Chen to become quantiative. Further, comparison of the flexoelectric couplings in oxygen-16 and oxygen-18 variants of $SrTiO_3$ could strengthen the theory by explaining the reduction of thermal Hall conductivity in the isotopically substituted compound. [23]

1.4.2.3 Side-jump scattering

There has been limited work on the side-jump scattering for phonon systems. This may be due to the lack of experimental evidence suggesting a sizeable side-jump contribution, or the relative difficulty of isolating the side-jump, or the difficulty in finding physically motivated settings in which the side-jump would occur. In any case, for completeness we briefly touch on the work of Guo who proposes the resonant side-jump to explain the Hall effect in cuprates. They note that the intrinsic coupling of phonons to the magnetic field typically rely on spin orbit coupling, which is relatively weak in cuprates. In addition to the pure intrinsic scenarion which, as noted above, is typically very small, this fact also seems to rule out intrinsic-extrinsic mechanisms where the Berry curvature of the phonon produces strong skew scattering.

The question then is to find a mechanism that does not rely on strong spin orbit coupling but preserves the experimental constancy of the Hall angle. Guo accomplishes this by considering the resonant scattering of phonons off magnetic defects. We think of the defect as two-level system and, despite the weak spin orbit coupling at the defect, when the splitting of the defect levels matches the phonon energy, we see a large enhancment of the scattering rate. This enhancement serves two purposes: first, it compensates for the weak spin orbit coupling and second, it produces a side-jump effect that is no longer independent of scattering rate. This occurs because, near resonance, the timescale at which phonons are absorbed and re-emmitted to produce a trasverse current is set by dynamics of the defect rather than the rate of incident phonons. This flavor of resonant absorbtion is often associated with the physics of glassy systems, as discussed by Anderson, and is possibly relevant to the underdoped cuprates. [67]

1.4.2.4 Intrinsic phonon Hall effect

Finally, the intrinsic Hall conductivity, where we ask how the basic phonon dynamics are altered to give a transverse current. Discussions of the intrinsic effect tend to be very technical so it's helpful to ground ourselves in a physical picture of what we're looking for. Falling back for a second on electrons, we know the intrinsic Berry curvature "acts like" a magnetic field (is a rank two antisymmetric tensor, or pseudovector). This synthetic magnetic field mixes components of the electron velocity without disspating energy, rotating an electron traveling along x into an electron traveling along y. We expect the intrinsic phonon Hall effect to be describable in a similar way. We need an object that losslessly transfers phonons from one momentum state to another.

Now the big conceptual difference is that, in the case of electrons, the transverse current is driven by an electric field. To state the obvious, this immediately suggests examining the response of the electron system to electric field – its electrical susceptibility. For phonon thermal transport it is not immediately obvious what the equivalent quantity is. But we'll work with what we have: we are interested in the response of the system to a thermal gradient. The thermal gradient drives a heat current by creating a population imbalance in lattice vibrations, or thermal strains. This suggests we look at the system's *strain* susceptibility.

To be a bit more precise, start with an innocuous definition of the electrical conductivity

$$j_i(\omega, \mathbf{k}) = \sigma_{ij}(\omega, \mathbf{k}) E_j(\omega, \mathbf{k}), \tag{1.12}$$

relating the current j_i to the electric field E_j. In linear response, the condctivity is the dynamic susceptibility in response to the electric field. In the clean limit, the Kubo formalism is a tractable way to compute the electron response and, relevant to us, the Berry curvature of electrons is the imaginary (dissipationless) antisymmetric part of the Kubo susceptibility. The formal equivalence is derived, for example, in Guiliani and Vignale. (For the dirty limit, see the dispairing chapter 7 in Mahan)

Because the intrinsic response dominates in the clean limit, the dynamic susceptibility provides a conceptual and computational link between the electrical and phonon Hall effects. As suggested above, we consider the stress-stress susceptibility which is probed, for example, in a pulse echo ultrasound experiment. [68] We want

$$C_{ijkl} = \int dt e^{i\omega t} \left\langle \left[\frac{\partial H}{\partial \varepsilon_{ij}}, \frac{\partial H}{\partial \varepsilon_{ij}} \right] \right\rangle, \tag{1.13}$$

which, in the limit of low frequency and long wavelength, reduces to the static thermodynamic definition of the elastic tensor as the second derivative of the free energy with respect to strain. [68] The imaginary antisymmetric piece of the dynamic elastic tensor does exactly what we want to generate a Hall effect. Explicitly, if we expand the antisymmetric imaginary component of the elastic tensor in powers of frequency, the linear in frequency term, known as the Hall viscosity $i\eta_{ijkl}(\omega)$, describes a stress, σ_{ij} (not conductivity), generated by a time varying strain

$$\sigma_{ij} = i\omega \eta_{ijkl} \varepsilon_{kl} = \eta_{ijkl} \dot{\varepsilon}_{kl}, \tag{1.14}$$

where η is real. As the imaginary antisymmetric part of a susceptibility, the Hall viscosity is a type of Berry curvature. To try avoiding extra confusion (of which there will be plenty of soon, maybe already?), we will call this the *strain* Berry curvature. The strain Berry curvature is exactly equivalent to the Hall viscosity divided by $\hbar$, and the two terms will be used interchangeably.

An alternative, less physical but more schematic route to the same idea is to ask what happens if we view the lattice strain as a tuning parameter in the complete system Hamiltonian, H. Given a set of eigenstates $|\Psi_i\rangle$, the expectation value of the change of H with respect to strain is

$$\left\langle \frac{\partial H}{\partial \varepsilon_{ij}} \right\rangle = \sum_i \langle \Psi_i | \frac{\partial H}{\partial \varepsilon_{ij}} | \Psi_i \rangle = \sum_i \frac{\partial}{\partial \varepsilon_{ij}} \langle \Psi_i | H | \Psi_i \rangle - 2\Re \left[\left\langle \frac{\partial \Psi_i}{\partial \varepsilon_{ij}} \right| H | \Psi_i \rangle \right]. \tag{1.15}$$

Using the Schrodinger equation this can be rewritten

$$\left\langle \frac{\partial H}{\partial \varepsilon_{ij}} \right\rangle = \frac{\partial E}{\partial \varepsilon_{ij}} + \sum_i 2\Im \left[\left\langle \frac{\partial \Psi_i}{\partial \varepsilon_{ij}} \middle| \middle| \frac{d\Psi_i}{dt} \right\rangle \right] = \frac{\partial E}{\partial \varepsilon_{ij}} + \sum_{kl} \dot{\varepsilon}_{kl} \sum_i 2\Im \left[\left\langle \frac{\partial \Psi_i}{\partial \varepsilon_{ij}} \middle| \middle| \frac{\partial \Psi_i}{\partial \varepsilon_{kl}} \right\rangle \right]. \tag{1.16}$$

Theleft hand side is something like a stress, while the term $\partial E / \partial \varepsilon_{ij}$ can be understood as the usual, in phase, stiffness. The second term, which is antisymmetric under exhchange $ij \leftrightarrow kl$, can be expressed as

$$\sum_{kl} \dot{\varepsilon}_{kl} \sum_i 2\Im \left[\left\langle \frac{\partial \Psi_i}{\partial \varepsilon_{ij}} \middle| \middle| \frac{\partial \Psi_i}{\partial \varepsilon_{kl}} \right\rangle \right] \equiv \Omega_{ijkl} \dot{\varepsilon}_{kl}, \tag{1.17}$$

where Ω_{ijkl} is, again, the strain Berry curvature.

The Hall viscosity is not a new concept and appears in Landau Lifshitz (Physical Kinetics, section 13) – it is "allowed by symmetry" and therefore must exist. Hall viscosity was later studied in relation to quantum Hall systems and exotic superconductivity before it was revived in the context of thermal transport. [69, 70] The role of Hall viscosity in the phonon Hall effect was clarified only after the discovery of the magnon Hall effect and the simultaneous theoretical developments of Matsumoto. [34, 71]

A full account of how to calculate the thermal Hall conductivity due to the Hall viscosity is beyond the scope of this introduction. [72] Possibly we'll do an appendix. After obtaining the Hall viscosity, we "just" need to include it in a Boltzmann or Kubo transport calculation. None of the core ideas are new, but of course the details are intricate. This is a nice opportunity, however, to introduce two related concepts which are central to discussions of the phonon Hall effect.

Though we have introduced the strain Berry curvature, which comes from the strain susceptibility, transport calculations are normally done starting with the quasiparticls band structure. For this reason, before doing a transport calculation, the (momentum dependent) Hall viscosity is usually folded into the phonon Hamiltonian as a low energy perturbation $\delta H_{visc} = \eta_{ijkl}\varepsilon_{ij}\dot{\varepsilon}_{kl}$. The Hall viscosity then alters the phonon dispersion and may be used to calcualate a *different* Berry curvature, this time defined in momentum space, on the phonon bands. This is exactly analogous to the momentum space Berry curvature of electrons and is usually called the phonon Berry curvature, $\mathbf{\Omega}(\mathbf{k})$.

The relation to thermal transport is most easily seen using Luttinger's trick. [73] The idea is to imagine the temperature gradient $\nabla T/T$ as a force pulling thermal energy to cold spots. In terms of a potential, ψ, the intrinsic part of the Boltzmann equation, Equation 1.8, can be written

$$\dot{\mathbf{r}}\nabla_E n \frac{E}{T}\nabla\psi = 0, \tag{1.18}$$

where $\nabla\psi = \nabla T/T$. This potential comes into the Hamiltonian as a correction $\delta H(\mathbf{k}) = E(\mathbf{k})\psi$, where $E(\mathbf{k})$ is the energy in the absence of the thermal gradient, from which we see that the resulting change in the phonon momentum is

$$\hbar\dot{\mathbf{k}} = \frac{\partial H}{\partial \mathbf{r}} = E\nabla\psi. \tag{1.19}$$

If there is also phonon Berry curvature, this generates an anomalous velocity $\mathbf{v} = \dot{\mathbf{k}} \times \mathbf{\Omega}$, as in the case of electrons in an electric field. The resulting transverse heat current is

$$\mathbf{j}_Q = \int \frac{d^3\mathbf{k}}{(2\pi)^3} E(\mathbf{k})\mathbf{v}(\mathbf{k})n_0(\mathbf{k}) = \int \frac{d^3\mathbf{k}}{(2\pi)^3} E(\mathbf{k})^2 \left(\frac{\nabla T}{T} \times \frac{\mathbf{\Omega}}{\hbar}\right) n_0(\mathbf{k}), \tag{1.20}$$

from which $\mathbf{j}_Q/\nabla T$ is the thermal Hall conductivity.

From these considerations, you would conclude that the intrinsic phonon Hall effect fits neatly into Boltzmann transport. And that is almost correct, however, there is a technical subtlety due to Matsumoto, building off work done on the thermopower of metals, that ammends Equation 1.20. [34, 74] This correction contrasts with a more intuitive aspect of charge transport and illustrates the subtleties of working with Kubo susceptibilities. In a magnetic system with magnetization $\mathbf{M}$, the internal field results in a bound current density $\mathbf{j}_b \sim \nabla\times\mathbf{M}$. Though it does not result in a net current in any particular direction (the little loops all cancel), the Kubo response needs the local current density as input, including the local magnetization current. In the case of charge transport, finding this quantity is familiar, as the magnetization is the derivative of the free energy with respect to magnetic field.

In the case of heat transport, however, finding the local energy current takes more care. To see the root of the ambiguity, note that the heat (and charge) current, $\mathbf{j}$ satisfies the continuity condition $\partial\rho/\partial t = -\nabla\cdot\mathbf{j}$, where ρ is the energy density. It seems like we can add any divergence free current without ruining continuity. However, in the same way that the magnetization results in circulating loops of charge current, the viscosity results in circulating loops of heat current. The correct Kubo thermal Hall requires self-consistently incorporating the effects of the viscosity into the local energy current density. This is accomplished by building off Luttinger's trick of faking the effect of a thermal gradient in the Hamiltonian. In particular, we add a ficticious vector potential $\mathbf{A}$ that couples to the heat current as $\mathbf{j}_Q\cdot\mathbf{A}$, in exact analogy to the coupling between electrical current and magnetic field. The potential $\mathbf{A}$ is then used to define the circulating heat current.

The local circulation of heat energy due to the viscosity is what prevents the intrinsic thermal Hall effect from being captured correctly in a simple Boltzmann transport. At first glance it would seem like little loops of energy current should all cancel and be irrelevant for transport. However, in the thermal transport problem the temperature gradient results in imperfect cancellation of the bound current and makes a real contributions to the Hall conductivity. Depending on the form of the Berry curvature, failing to correctly account for these loops of heat current can result in a diverging thermal Hall conductivity or violation of the Wiedemann Franz law as $T \to 0$. [34]

Up to now, the source of the Hall viscosity has not been specified. The Feynmann Hellman type derivation given in Equation 1.16 makes it clear that, in principle, any time reversal symmetry breaking subsystem that couples to strain can generate Hall viscosity. One obvious contender is the spin lattice coupling, which results from the dependence of the exchange integral on the relative position of atomic orbitals in real space. Though

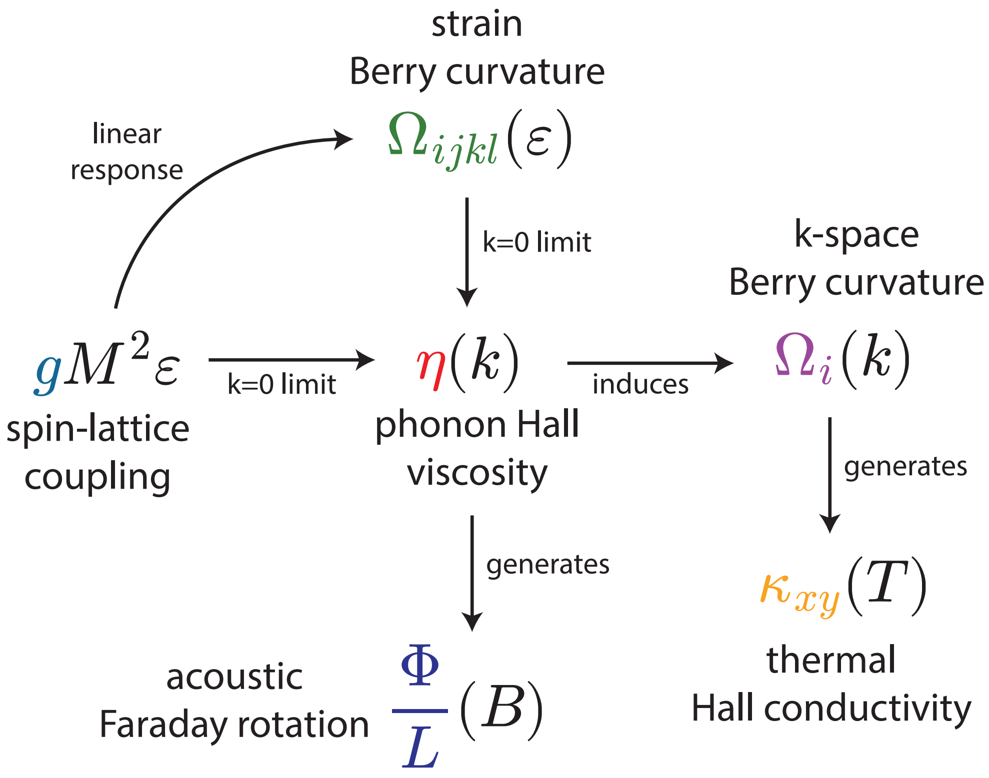

Figure 1.6: **Roadmap of the Hall viscosity:** The intrinsic thermal Hall effect of phonons can be thought of as arising from Berry curvature. This conceptual understanding, however, has many interpretations depending on the context. Fundamentally, the Hall conductivity of phonons (inversion and time reversal even objects) must result from coupling to another degree of freedom, for example spin-lattice coupling. The coupling is reflected in the material's response to lattice deformation and defines the strain Berry curvature in linear response. In the long wavelength limit, the strain Berry curvature can be interpretted as a dissipationless phonon Hall viscosity that alters the dynamics of sound waves. A property of the phonon dispersion, the Hall viscosity induces a Berry curvature on the phonon bands. By transferring energy between elastic modes, the Hall viscosity generates both thermal Hall and acoustic Faraday effects.

not framed in the language of Berry curvature, the role of spin lattice coupling in dissipationless phonon dynamics was initially explored by Kittel. [30] A detailed account of Hall viscsoity in the Kittel model is presented in a later chapter. More recent works have examined the Hall viscosity in layered magnetic systems, for example the cuprates, and frustrated spin systems such as α-RuCl_3. [75, 76] A phonon Hall effect from coupling to spinons is discussed in Zhang. [77] Though the details of the coupling mechanism differs between these proposals, the conceptual meat is the same.

Though the idea of Hall viscsoity is intellectually appealing, it remains to be seen if it is experimentally relevant. Generically the intrinsic phonon Hall effect is expected to be much smaller than what is measured in experiment. This expectation comes from estimates of the following form: insert a generic Berry curvature Equation 1.10 into the expression for the Hall current Equation 1.20. Then, ignoring the complications of energy magnetization which do not change the outcome here, this gives a thermal Hall conductivity that scales as

$$\kappa_{xy} \sim \frac{k_B^4}{\hbar^3} \frac{\eta}{Cv} T^3, \tag{1.21}$$

where, again, η is the viscosity, C is the elastic sitffness, and v is the speed of sound. Note that the T^3 scaling is generic to the low temperature intrinsic contribution, where the thermal energy is small enough that the momentum dependence of η is irrelevant. If we put in numbers, say $\eta = 10^{-3}$ Pa·s, $C = 100$ GPa, $v = 3000$ m/s, we get $\kappa_{xy} \approx 10^{-4}$ W/m·K at 10 K, where the thermal Hall conductivity is found to peak. This is actually not so far from experimental values.

The estimate, however, relies on the momentum independence of the viscosity over the thermal energy scale. In a perturbative picture, the viscosity is the result of phonons coupled to a rapidly changing excitation that can be integrated out of the problem. [75] So the assumption is only valid when the energy gap of the excitation is much larger than $k_B T$. If we take the case of magnetic excitations where the energy gap can be of order the applied magnetic field, then for a typical 10 T magnetic field, the range of appropriate temperatures is closer to 1 K, which reduces the estimate to a value orders of magnitude below what is seen in experiment. A further assumption is the value of the viscosity, η. The corresponding value due to electrical polarization fluctuations in SrTiO_3 is estimated to be much smaller than what we have used here. [66]

This estimate does, however, point to scenarios in which the Hall viscosity *can* produce an experimentally relevant thermal Hall effect. First, we might find a material in which the Hall viscosity arises from fluctuations that extend to low energy, rather than decaying from a sharp mode at high energy. A large spin-lattice coupling combined with a viscosity that decays slowly as a fucntion of momentum would bring the intrinsic effect back into play. This will be relevant to our measurements in α-$RuCl_3$. [76] Second, we can imagine a case where the perturbative picture is no longer valid at all, as in the case of phonon-magnon hybridization at a band crossing. The hybrid excitations have a distinct character from phonons and can result in viscosity "hot spots" at the band crossing. [78] This may be relevant in systems with significant thermal Hall conductivity at high temperature such as $Fe_2Mo_3O_8$.

1.4.3 Summing up theories

So, out of the zoo of thermal Hall measurements comes a zoo of thermal Hall theories. We loosely followed the more mature understanding of the anomalous Hall effect in metals to divide the possible mechansims into intrinsic and extrinsic, according to whether they rely on scattering. We saw how it is difficult to convincingly demonstrate the dominance of any single contribution experimentally, where perhaps the gold standard is a controlled disorder study at low temperature.

Considering the data we have, the approximate temperture independence of the thermal Hall angle in many materials is suggestive of skew scattering, modulo the complications of inelastic scattering. Further, many estimates of an intrinsic contribution fall far below what is found in experiment. As such, skew scattering of phonons off charged defects may explain the phonon Hall effect in systems where these defects exist, for example insuating oxides. Because many of the materials which exhibit a phonon Hall effect also host a form of fluctuating or high energy excitation that couples to strain, a number of proposals invoke an intrinsic-extrinsic scenario. This many be relevant in strontium titanate or the underdoped cuprates.

Though the intrinsic contribution is generically understood to give a negligible thermal Hall effect, we saw that there are important exceptions and that the intrinsic scenario cannot be universally ruled out. The intrinsic contribution is plausibly relevant in materials with magnetic fluctuations that extend to low energy, or in which there is strong hybridization between phonons and another sharp, time reversal symmetry breaking excitation. Given the diversity of insulators in whcih the thermal Hall effect has been measured, it seems unlikely that a single explanation can accomodate all the data.

How do we untangle this mess?

Chapter 2

The Experiment

2.1 Measuring the intrinsic Hall effect

Armed with information about the thermal Hall effect of insulators, we are ready to introduce the core ideas to explore experimentally. Our motivation at this point is clear: the thermal Hall effect in insulators, a surprising experimental discovery, can have many sources. We want an experimental probe that can show us where the Hall effect is coming from, so we can learn about spin liquids and underdoped cuprates.

Transport, though exceptionally powerful, is too blunt a tool. But thermal transport is non-specific in very specific ways. First, in a thermal transport experiment you probe with an ensemble of phonon energies, as the heat current you inject samples the Bose distribution at the experimental temperature. This is obviously problematic if you want to zero in on resonant side-jump scattering or the viscosity generated at a band crossing, both of which happen over a small energy window. Second is the ubiquity of scattering – all materials have imperfections. This is less relevant when we consider a transport method like quantum oscillations, where changes in the resistivity are what matter. However, the multiplicity of scattering types combined with the difficulty of treating scattering in a controlled way theoretically make teasing out information about extrinsic sources of the Hall effect incredibly tricky.

These considerations – lack of specificity in energy, and the complications of scattering – immediately suggest a spectroscopic tool to complement the thermal transport. Further, because life is already hard enough, we might sidestep the extrinsic mechanism entirely and look specifically at the intrinsic Hall effect. That's what we'll do.

As we saw previously, the intrinsic phonon Hall effect can be understood as the consequence of strain Berry curvature, or Hall viscosity. The Hall viscosity is defined as the antisymmetric, imaginary part of the dynamical strain susceptibility, which can be measured directly with ultrasonic probes like resonant ultrasound spectroscopy or the pulse echo method. [79, 80] The focus of this document is the pulse echo method.

This chapter will is divided into two main sections. We first review the properties of the elastic tensor and its relationship to the physical observables measured in the pulse echo experiment. These physical observables will be connected back to the intrinsic phonon Hall effect. Second, we will discuss the details of how the pulse echo measurement is done, starting from a chunk of crystal and ending with data. The chapter closes with some possible future technical directions to explore. This is the only chapter that matters, so I hope it works.

2.2 Conceptual Background

2.2.1 The elastic tensor: basics

When you cool water through zero degrees celsius it becomes ice. The defining characteristics of the solid ice, as opposed to liquid water, are its ability to resist stretching and twisting. These rigidities let us know we have entered a new phase of matter. The structural features appear because of the bonds that develop between molecules on entering the solid phase and, therefore, contain information about the nature of those bonds. Quantitatively, the resistance to stretching, compressing, and twisting is encoded in the relationship between strain, the degree of deformation, and stress, the resulting forces.

Because a rigid translation of an object is space does not change its internal structure, the deformations we are interested in must have some spatial variation. If we imagine breaking up our object into chunks of volume dV and labeling the positions of each chunk before and after deformation $\mathbf{u}_i$ and $\mathbf{u}_i'$, then the relevant strains are those in which $d\mathbf{u}_i = \mathbf{u}_i - \mathbf{u}_i'$ varies as a function of position.

Because the rigid rotation of an object in space does not change its internal structure, in the limit of very long wavelengths we can subtract the rotational component from the deformation. A rotation of the displacement $d\mathbf{u}_i$ about $\hat{\mathbf{n}}$ corresponds to the curl $\hat{\mathbf{n}} \cdot (\nabla \times d\mathbf{u})$, so we subtract this out of the deformation. (Antisymmetric strains do have physical consequences, and have been measured experimentally, see [80].) What we are left with are the symmetric gradients of the deformation, and we define the strain tensor, $\hat{\varepsilon}$ with components

$$\varepsilon_{ij} = \frac{1}{2}\left(\frac{\partial u_i}{\partial x_j} + \frac{\partial u_j}{\partial x_i}\right). \tag{2.1}$$

Because of the rigid bonds between atoms, distortions of the lattice result in forces, $\mathbf{F}$, which act to bring the atoms back to their equilibrium positions. In equilibrium the net force *within* the object must be zero, and the only non-zero forces are on the object's surface

$$\mathbf{F}_{surf} = \int d\mathbf{A} \cdot \hat{\sigma}_{surf}, \tag{2.2}$$

where $\hat{\sigma}_{surf}$ is the surface pressure, a matrix with components that tell you the force component i per unit area normal to the direction x_j. The Gauss law tells us we can track this surface pressure back into the object's interior, converting the surface integral to one over the bulk – this defines the stress tensor σ_{ij}, from which the body forces are $\mathbf{F} = \nabla \cdot \hat{\sigma}$. The absence of net torque on the object guarantees that the stress tensor is symmetric, $\sigma_{ij} = \sigma_{ji}$.

The work done displacing a small volume of material by an amount $d\mathbf{u}$ against the internal force is $dW = \mathbf{F} \cdot d\mathbf{u} = \nabla \cdot \hat{\sigma} \cdot d\mathbf{u}$. Integrating over the volume of the object, transfering the derivative to the displacement, and ignoring the object's boundary we arrive at the elastic potential energy

$$U_{el} = \sigma_{ij}\varepsilon_{ij}, \tag{2.3}$$

which is the fundamental quantity that allows us to extract thermodynamic and spectroscopic information. In the limit of small displacements, the relationship between the stress and strain tensors is linear and can be defined through the tensor of elastic moduli

$$\sigma_{ij} = C_{ijkl}\varepsilon_{kl}. \tag{2.4}$$

Since the stress and strain are symmetric, we know C_{ijkl} is invariant under interchanging either or both of $i \leftrightarrow j$ and $k \leftrightarrow l$. Because the elastic energy can be written $C_{ijkl}\varepsilon_{ij}\varepsilon_{kl}$, we also know that C_{ijkl} is invariant under interchange of the first and second pairs of indices.

Additionally, because the stress and strain are a conjugate pair of variables, when a system is in equilibrium the elastic modulus can be defined thermodynamically

$$C_{ijkl} = \left.\frac{\partial^2 U}{\partial\varepsilon_{ij}\partial\varepsilon_{kl}}\right|_{\varepsilon\to 0}. \tag{2.5}$$

For completeness, we note that our experiment will done at finite frequency and, consequently, the quantity we probe is the dynamic stress-stress susceptibility

$$C_{ijkl}(\omega) = \frac{iV}{\hbar Z}\int dt e^{i\omega t}\mathrm{Tr}\left[\mathrm{e^{-H/k_BT}}\left[\sigma_{\mathrm{ij}}(0), \sigma_{\mathrm{kl}}(\mathrm{t})\right]\right] \tag{2.6}$$

where $Z = \mathrm{Tr}[\mathrm{e^{-H/k_BT}}]$ is the partition function, H is the Hamiltonian, and V is the sample volume. In the limit $\omega \to 0$, this matches the thermodynamic definition. This can be seen by writing $\sigma_{kl}(t) = e^{iHt}\sigma_{kl}(0)e^{-iHt}$, inserting the indentity, and carrying out the integral in time. We only bring this up because in what follows we are especially interested in the dynamics of the strain wave, which are not captured in the thermodynamic definition.

2.2.2 The elastic tensor: decomposition

We aim to measure the portion of the elastic response the would generate a thermal Hall effect. Before setting out to do the experiment, we should know if that particular elastic response is allowed by symmetry.

Like any tensor, the dynamical elastic tensor can be decomposed into real (time even) and imaginary (time odd) parts, we write $C_{ijkl} = c_{ijkl} + i\eta_{ijkl}$. These can be further subdivided into symmetric and antisymmetric parts. A summary of the decomposition is given in Figure 2.1. Because we maintain the stress and strain as symmetric objects, when we say symmetric and antisymmetric, we mean under the exchange of the first and second pair of indices:

$$C_{sym} = \frac{1}{2}\left(C_{ijkl} + C_{klij}\right) \qquad C_{asym} = \frac{1}{2}\left(C_{ijkl} - C_{klij}\right). \tag{2.7}$$

The tensor of elastic moduli can, in principle have arbitrarily complicated dependence on frequency. In this discussion, relevant to low energy ultrasound experiments, we will restrict ourselves to liner order in ω or, equivalently, keeping only one time derivative of strain in the potential energy. In this approximation the real antisymmetric part of the modulus is zero. Writing out what is left explicitly gives an elastic potential energy

$$U_{el} = \frac{1}{2}c_{ijkl}\varepsilon_{ij}\varepsilon_{kl} + \frac{1}{2}\eta_{ijkl}\varepsilon_{ij}\dot{\varepsilon}_{kl}, \tag{2.8}$$

where c_{ijkl} tells us about the dispersion (speed of sound) and the viscous contribution η_{ijkl} tells about mode conversion, either into heat or between elastic modes. The symmetric viscosity results in energy loss and is even under reversing the sign of an applied magnetic field. In the context of an ultrasound experiment the symmetric viscosity is proportional to the ultrasonic attenuation. The antisymmetric, Hall viscosity, generates acoustic Faraday rotation and an intrinsic thermal Hall effect.

The number of independent elastic moduli are reduced in a symmetric environment such as a crystal lattice, and some tensor elements are forced to zero. To discover which components remain, we break the stress and strain tensors into pieces that transform together under symmetry operations of the lattice. These are called irreducible strains and stresses (Landau Lifshitz Quantum Mechanics gives an excellent treatment of the irreducible representations). For example, the trace of the strain tensor behaves like a number (scalar): under rotations, reflections, and mirror operations the trace stays the same.

An irreducible elastic modulus, an independent component of the real, symmetric part of the elastic tensor, is the ratio of stress to strain of the same type. So for each irreducible stress/strain there is one elastic constant, and if there are multiple stresses/strains of the same irreducible type we get an extra elastic constant connecting each pair.

To find the number of irreducible strains, we need to know the number of irreducible strains. The easiest way to do that is to think of the strain tensor as built from a symmetric outer product of two vectors. As a concrete example we can figure out the irreducible strains in an isotropic

$$C_{ijkl} = c_{ijkl} + i\eta_{ijkl}$$

	Real	Imaginary
Symmetric	$\frac{c_{ijkl} + c_{klij}}{2}$ Dispersion	$\frac{\eta_{ijkl} + \eta_{klij}}{2}$ Loss
Antisymmetric	0	$\frac{\eta_{ijkl} - \eta_{klij}}{2}$ Hall Viscosity

Figure 2.1: **Decomposition of the elastic tensor:** The tensor of elastic moduli, C_{ijkl}, can be split into real and imaginary parts, which are further decomposed into symmetric and antisymmetric components. By the Onsager reciprocity, the real part, c_{ijkl}, is even under time reversal and the imaginary part, η_{ijkl}, is time-odd. The real symmetric modulus is the lattice stiffness and is proportional to the (direction dependent) speed of sound. The symmetric imaginary part generates "trivially" time-odd energy loss, and is proportional to the ultrasound attenuation. The imaginary antisymmetric piece, the Hall viscosity, describes dissipationless mixing between symmetry channels and can result in acoustic Faraday and thermal Hall effects.

medium. In that case, the symmetry of the environment is the full rotational group O(3). The irreducible representations of O(3) are the spherical harmonics, and a vector transforms like a *p*-orbital, so we want to find the number of spherical harmonics in the symmetric product of a *p*-orbital with itself. We do this using the rules for addition of angular momentum from quantum mechanics:

$$p \otimes p = s \oplus p \oplus d \tag{2.9}$$

ie, the sum of the angular momentum of two objects with angular momentum $\ell = 1$ can have $\ell = 0, 1, 2$ - an *s*-, *p*-, or *d*- orbital. The rules of the addition of angular momentum tell us the $\ell = 1$ part of the sum is antisymmetric and the *s*- and *d*- multiplets are symmetric. So there are two irreducible strains: one which transforms like a scalar (*s*-wave, monopole) and one which transforms like a five-dimensional object (*d*-wave, quadrupole). The scalar is a compressional strain and the *d*-wave part is the shear. So despite starting with potentially 21 independent symmetric elastic moduli, we end up with only 2 in an isotropic environment.

As we lower the symmetry we increase the number of elastic moduli. The 5 component shear strain successively breaks into smaller and smaller bits, which allows more couplings between irreducible strains. For example, one environment we encounter later is the cubic symmetry, $\mathrm{O_h}$, in which the shear splits into a 3-component (T_{2g}) strain and 2-component (E_g) strain (three elastic moduli).

Figuring out the number of elastic moduli in a general, lower symmetry environment follows the same formulaic plan as in free space, the only tools we need are character and representation multiplication tables. Identify the representations that contain the vector (x, y, z), express the square of that collection of representations as a sum, and keep only the symmetric parts. Each representation in that sum is an irreducible strain. For example, in $\mathrm{S_6}$, the symmetry group of α-$\mathrm{RuCl_3}$, the vector is $A_u \oplus E_u$, and the square is

$$(A_u \oplus E_u) \otimes (A_u \oplus E_u) = \begin{bmatrix} A_u \otimes A_u & A_u \otimes E_u \\ E_u \otimes A_u & E_u \otimes E_u \oplus [A_g] \end{bmatrix} = \begin{bmatrix} A_g & E_g \\ E_g & E_g \oplus A_g \oplus [A_g] \end{bmatrix}. \tag{2.10}$$

So the symmetric part, the irreducible strains, are $2A_g + 2E_g$, where the antisymmetric $[A_g]$ in the product E_u^2 gets thrown away, and the off-diagonal E_g parts are the same object. Or, you can cheat and find the strains by looking for representations with quadratic basis functions. Either way, you get six independent elastic moduli. The lossy viscosity (imaginary, symmetric) has the same symmetric properties as the real symmetric tensor, and therefore the same number of independent components.

The imaginary antisymmetric moduli, the Hall viscosities, behave in a slightly different way. The antisymmetric viscous part of Equation 2.8, written now in terms of irreducible representations, is

$$U_{\text{visc}} = \frac{\eta_{\Gamma\Gamma'}}{2}(\dot{\varepsilon}_{\Gamma}\varepsilon_{\Gamma'} - \varepsilon_{\Gamma}\dot{\varepsilon}_{\Gamma'}). \tag{2.11}$$

The system, assumed to break time reversal symmetry (whether intrinsically or through an applied magnetic field), allows $\eta_{\Gamma\Gamma'}$ to be time odd. Both the energy and tensor element $\eta_{\Gamma\Gamma'}$ are scalars (A_g objects in the S_6 point group), which requires the term in parentheses in Equation 2.11 to also be a scalar. Because $\eta_{\Gamma\Gamma'}$ is antisymmetric under exchange $\Gamma \longleftrightarrow \Gamma'$, this forces either: 1) that $\varepsilon_\Gamma = \varepsilon_{\Gamma'}$ and that the representation Γ squared contains an antisymmetric scalar (and therefore must two or three dimensional); or 2) that ε_Γ and $\varepsilon_{\Gamma'}$ are distinct strains that belong to the same representation.

As a simple example, we can consider the case of an isotropic, time reversal symmetry breaking medium. As noted above, the strains transform as $\ell = 0$ (s-wave, compression) and $\ell = 2$ (d wave shear) spherical harmonics. A viscosity element could only come from an antisymmetric component of the product of the shear strain with itself. However, the scalar, s wave component of the product $d \otimes d$ is symmetric under exchange. Therefore, we conclude that the isotropic medium has no Hall viscosity, a result repeated many times in the literature.

When time reversal symmetry is broken by an applied magnetic field, it is more transparent to "factor out" the magnetic field from the Hall viscosity. Then, to identify which magnetic field components generate which Hall viscosity coefficients, we expand the viscosity to linear order in applied magnetic field. The magnetic field splits into representations, B_Σ, and we form the antisymmetric products which each contribute to the elastic energy,

$$U_{\text{visc}}(B_\Sigma) = B_\Sigma\, \tilde{\eta}^{\Sigma}_{\Gamma\Gamma'}(\dot{\varepsilon}_{\Gamma}\varepsilon_{\Gamma'} - \varepsilon_{\Gamma}\dot{\varepsilon}_{\Gamma'}), \tag{2.12}$$

where now the coefficient $\tilde{\eta}^{\Sigma}_{\Gamma\Gamma'}$ is a scalar and has unit of $\mathrm{Pa{\cdot}s{\cdot}T^{-1}}$, and the antisymmetric term in parentheses transforms as Σ so that the whole expression is a scalar. Note that the product $\dot{\varepsilon}_\Gamma \varepsilon_{\Gamma'}$ generically decomposes into the sum of multiple representations, not all of which transform like Σ. To avoid cluttering the notation further, we specify which portion of the product is involved in a particular term with the superscript on the coefficient $\tilde{\eta}^{\Sigma}_{\Gamma\Gamma'}$ (but again note that $\tilde{\eta}^{\Sigma}_{\Gamma\Gamma'}$ itself is always a scalar).

To illustrate this idea, consider the isotropic medium again, but now with time reversal symmetry broken by the application of a magnetic field. The magnetic field transforms as an inversion even p wave harmonic. Considering the available products of strain, we see that the square of the d wave shear strain contains an antisymmetric under exchange p wave component, and can couple linearly to the magnetic field. (Note also, that the cube of the magnetic field has an $\ell = 3$ component that can couple to the f wave component the shear strain squared – we can generate more viscosities by considering higher powers of mangetic field.) Therefore, up to third order in $\mathbf{B}$ we have two Hall viscosities, in agreement with the arguments of Landau and Lifshitz, Physical Kinetics.

Now we take the specific example of α-RuCl$_3$. Below its structural transition at 150 K, α-RuCl$_3$transitions to rhombohedral symmetry with point group S$_6$. There are four irreducible strains in S$_6$: two A_g strains and two E_g strains:

$$\varepsilon_{A_g^{(1)}} = \varepsilon_{x^2+y^2}, \quad \varepsilon_{A_g^{(2)}} = \varepsilon_{z^2}, \ \varepsilon_{E_g^{(1)}} = \left\{\varepsilon_{x^2-y^2}, \varepsilon_{xy}\right\}, \quad \varepsilon_{E_g^{(2)}} = \left\{\varepsilon_{xz}, \varepsilon_{yz}\right\}.$$

The magnetic field splits into two representations: the out-of-plane component transforms as A_g, and the in-plane component transforms as E_g:

$$B_{A_g} = B_z, \quad B_{E_g} = \left\{B_x, B_y\right\}.$$

To simplify the notation in what follows, we drop the g in the representation labels since we only need to consider representations that are even under inversion. As mentioned earlier, because the product of two strains can decompose into the sum of several other strains, we use the notation from Equation 2.12 to specify which viscosity coefficient goes with which strain in the sum. For example, one such term will be

$$U_{\text{visc}}(B_{A_{1g}}) \sim B_{A_g} \tilde{\eta}^{A_g}_{E_g^{(1)} E_g^{(2)}} (\varepsilon_{E_g^{(1)}} \dot{\varepsilon}_{E_g^{(2)}} - \dot{\varepsilon}_{E_g^{(1)}} \varepsilon_{E_g^{(2)}}) \equiv B_A \tilde{\eta}^{A}_{E_1 E_2} (\varepsilon_{E_1} \dot{\varepsilon}_{E_2} - \dot{\varepsilon}_{E_1} \varepsilon_{E_2}), \quad (2.13)$$

where $\tilde{\eta}^{A}_{E_1 E_2}$ denotes a viscosity term that couples the A_g portion of the product of $E_g^{(1)}$ and $E_g^{(2)}$ strains to the B_{A_g} magnetic field component.

With an out-of-plane magnetic field B_z, we can form the following four Hall viscosity contributions to the elastic energy:

$$\begin{aligned} U_{\text{visc}}(B_z) = B_A \Big[& \tilde{\eta}^{A}_{A_1A_2}(\varepsilon_{A_1}\dot{\varepsilon}_{A_2} - \dot{\varepsilon}_{A_1}\varepsilon_{A_2}) + \tilde{\eta}^{A}_{E_1E_2}(\varepsilon_{E_1}\dot{\varepsilon}_{E_2} - \dot{\varepsilon}_{E_1}\varepsilon_{E_2}) \\ & + \tilde{\eta}^{A}_{E_1E_1}(\varepsilon_{E_1}\dot{\varepsilon}_{E_1} - \dot{\varepsilon}_{E_1}\varepsilon_{E_1}) + \tilde{\eta}^{A}_{E_2E_2}(\varepsilon_{E_2}\dot{\varepsilon}_{E_2} - \dot{\varepsilon}_{E_2}\varepsilon_{E_2}) \Big], \end{aligned} \tag{2.14}$$

where the last two terms, which involve the square of a representation, arise because the product of E_g with itself contains an antisymmetric object which transforms as A_g.

An in-plane magnetic field generates five Hall viscosity terms:

$$\begin{aligned} U_{\text{visc}}(B_x, B_y) = B_E \Big[& \tilde{\eta}^{E}_{A_1E_1}(\varepsilon_{A_1}\dot{\varepsilon}_{E_1} - \dot{\varepsilon}_{A_1}\varepsilon_{E_1}) + \tilde{\eta}^{E}_{A_1E_2}(\varepsilon_{A_1}\dot{\varepsilon}_{E_2} - \dot{\varepsilon}_{A_1}\varepsilon_{E_2}) \\ & \tilde{\eta}^{E}_{A_2E_1}(\varepsilon_{A_2}\dot{\varepsilon}_{E_1} - \dot{\varepsilon}_{A_2}\varepsilon_{E_1}) + \tilde{\eta}^{E}_{A_2E_2}(\varepsilon_{A_2}\dot{\varepsilon}_{E_2} - \dot{\varepsilon}_{A_2}\varepsilon_{E_2}) \\ & + \tilde{\eta}^{E}_{E_1E_2}(\varepsilon_{E_1}\dot{\varepsilon}_{E_2} - \dot{\varepsilon}_{E_1}\varepsilon_{E_2}) \Big]. \end{aligned} \tag{2.15}$$

The Hall viscosity we measure in our experiment, where the shear sound propagates along the c-axis of the crystal, shows up here as $B_A\tilde{\eta}^{A}_{E_2E_2} = \eta_{xzyz}$ and is only generated by the out-of-plane magnetic field, B_z. When the magnetic field is tilted away from the *c* axis (but with some component still along z), all nine Hall viscosity coefficients from both Equation 2.14 and Equation 2.15 can be generated, including η_{xzyz}.

When the applied magnetic field is strong compared the exchange interaction, it is appropriate to consider the effect of the magnetic field on the symmetry of the crystal. In particular, the applied magnetic field is considered a “fixed” part of the system and the symmetry is lowered to operations, including time reversal symmetry, that preserve the direction of the field. As an example we can analyze the tetragonal system considered in the context of the Hall effect of cuprates. [75] The point group of the crystal in $\mathrm{D_{4h}}$ and with a strong magnetic field along the crystal c-axis, the symmetry is lowered to $\mathrm{C_{4h}}$, in which there are two A_g, two B_g, and one E_g irreducible strains. This gives three Hall viscosities, in agreement with [75]: the distinct A_g strains can couple, the distinct B_g strains can couple, and the square of E_g contains an antisymmetric scalar. (Note that, confusingly, in this case the literature usually reverts *back* to the parent group at $\mathbf{B} = 0$.)

2.2.3 Elastic dynamics

Having identified the non-zero elements of the Hall viscosity tensor, we turn to how the Hall viscosity manifests in an experiment. We consider the propagation of sound waves in a crystal with Hall viscosity. Having identified the elastic potential energy Equation 2.8, we can write the Lagrangian of the elastic medium with mass density ρ

$$\mathcal{L} = \frac{\rho}{2}\dot{u}_i\dot{u}_i - \frac{c_{ijkl}}{2}\varepsilon_{ij}\varepsilon_{kl} - \frac{\eta^{(S)}_{ijkl}}{2}\varepsilon_{ij}\dot{\varepsilon}_{kl} - \frac{\eta^{(A)}_{ijkl}}{2}\varepsilon_{ij}\dot{\varepsilon}_{kl}, \tag{2.16}$$

where $\eta^{(S)}$ is the symmetric viscosity and $\eta^{(A)}$ is the antisymmetric Hall viscosity. We now add pieces in, one by one.

When both the symmetric and antisymmetric viscosities are zero, the equation of motion for a harmonic displacement $\mathbf{u} = \mathbf{A}e^{i(\omega t - \mathbf{k}\cdot\mathbf{r})}$ with wave vector $\mathbf{k}$, frequency ω, and polarization $\mathbf{A}$ is the standard wave equation

$$\rho\omega^2 A_i = c_{ijkl}k_jk_kA_l \equiv \rho v^2 A_i = M_{ij}A_j, \tag{2.17}$$

where $M_{ij} \equiv c_{iklj}\hat{k}_k\hat{k}_l$, cares only about the direction of $\mathbf{k}$, and $v = \omega/k$ is the phase velocity of the wave. Because M_{ij} is symmetric and real, there are always three prependicular polarizations. However, when the symmetry is sufficiently high, the polarizations are only parallel and perpendicular to the propagation direction. By considering rotations of the elastic tensor about the direction of the wave vector, it is not hard to show that a two- or three-fold axis of rotation about the wave vector is necessary and sufficient for the polarizations to be parallel and perpendicular to $\mathbf{k}$. In a triclinic crystal there are no transverse waves.

In passing, note that because the elastic tensor is rank four (ie it transforms as four copies of a vector, and $\ell = 1$ object) its decomposition into spherical tensors contains only those with $\ell \leq 4$. For this reason, an axis of higher than four-fold symmetry is indistinguishable from full rotational symmetry: an hexagonal crystal looks isotropic in the plane. Similarly, the polarization is a vector, and so propagation along three-fold axes of symmetry and higher have only one distinct transverse speed of sound.

It is also intereting to ask the effect of tilting the wave vector slightly off an axis of high symmetry. How much to the speeds of sound and polarization vectors change? Some insight comes from perturbation theory. A small rotation away from the original propagation direction can be expressed as $\mathbf{1} + \boldsymbol{\theta}\cdot\mathbf{J}$, where $\mathbf{1}$ is the identity, $\mathbf{J}$ are the generators of rotation, and $\boldsymbol{\theta}$ is a small angle that defines the perturbation. Corrections to the speed of sound at first order in θ will come from

$$\frac{\delta v}{v} = A_i(\boldsymbol{\theta} \cdot \mathbf{J})_{j\mu} C_{i\mu kl} k_j k_k A_l. \tag{2.18}$$

For high symmetry directions, **k** and **A** are either perpendicular or parallel and, for a rotation away from **k**, this first order correction vanishes, being proportional to elements of the elastic tensor that are zero. Therefore, the corrections to the speed of sound go as θ^2. (An exception to this rule is for propagation along the three-fold axis in cubic symmetry.) The correction to the polarization will go as the small angle θ divided by the different in the speeds of sound squared.

Now we consider the effect of symmetric viscosity. The stress is now

$$\sigma_{ij} = (c_{ijkl} + i\omega\eta^{(S)}_{ijkl})\varepsilon_{kl}, \tag{2.19}$$

from which we find the power density of the elastic wave

$$P = \frac{dU_{el}}{dt} = i\omega \Im \sigma_{ij}\varepsilon_{ij} = \omega^2 \eta^{(S)}_{ijkl}\varepsilon_{ij}\varepsilon_{kl}. \tag{2.20}$$

Dividing by the total energy density (assuming the $\eta^{(S)}\omega \ll c$), we find the ultrasound attenuation per unit length

$$\alpha = \frac{\omega^2}{\rho v^3}\eta^{(S)}_{ijkl}\hat{A}_i\hat{k}_j\hat{A}_k\hat{k}_l, \tag{2.21}$$

where we have converted the strains to displacements and divided by the speed of sound, v. This is only valid for particularly high symmetry directions, but the flavor is correct. So we confirm that the symmetric imaginary part of the elastic tensor results in loss.

Now consider the antisymmetric imaginary Hall viscosity. Now the power loss is

$$P \sim \eta^{(A)}_{ijkl}\varepsilon_{ij}\varepsilon_{kl} = 0 \tag{2.22}$$

by the antisymmetry of the tensor, so this is a lossless viscosity. To see what the Hall viscosity does we go back to the Lagrangian and consider the case of a sound propagating along a two-fold symmetric z-axis with a single Hall viscosity element, $\eta = \eta_{xzyz}$, so that Equation 2.16 becomes

$$\mathcal{L} = \frac{\rho}{2}\dot{u}^2 - \frac{c_{44}}{2}k^2 u_y^2 - \frac{c_{55}}{2}k^2 u_x^2 - \frac{\eta}{2}k^2(u_x\dot{u}_y - \dot{u}_x u_y), \tag{2.23}$$

from which we derive the equation of motion

$$\rho\omega^2\vec{u} = k^2\begin{bmatrix} c_{55} & i\eta\omega \\ -i\omega\eta & c_{44} \end{bmatrix}\vec{u}. \tag{2.24}$$

We can gain some intuition for the equation of motion by rewriting the matrix on the right-hand side in terms of the average elastic modulus $c = (c_{44} + c_{55})/2$ and the difference $\delta = (c_{44} - c_{55})/2$. Then the equation of motion becomes a sum of Pauli matrices,

$$\begin{bmatrix} c_{55} & i\eta\omega \\ -i\omega\eta & c_{44}. \end{bmatrix} = c1 + \delta\sigma_z + \omega\eta\sigma_y \tag{2.25}$$

The square of the phase velocities, $v_\pm^2 = \omega^2/k^2$, are then

$$\rho v_\pm^2 = c \pm \sqrt{\delta^2 + \omega^2\eta^2}, \tag{2.26}$$

so that the two transverse wave speeds are split both by the difference in elastic moduli and by the viscosity. The polarizations are, up to a normalization constant,

$$\mathbf{u}_+ = \frac{1}{\sqrt{\delta^2 + \omega^2\eta^2}}\begin{bmatrix} \delta + \sqrt{\delta^2 + \omega^2\eta^2} \\ i\omega\eta \end{bmatrix} \qquad \mathbf{u}_- = \frac{1}{\sqrt{\delta^2 + \omega^2\eta^2}}\begin{bmatrix} i\omega\eta \\ \delta + \sqrt{\delta^2 + \omega^2\eta^2} \end{bmatrix}. \tag{2.27}$$

From Equation 2.27 we can see that when $\eta = 0$, changing δ does not change the polarizations thought it does split the degenerate speeds of sound. When $\delta = 0$ adding non-zero viscosity results in circular rather than linear polarizations. Finally, when both $\eta, \delta \neq 0$, we get elliptical polarizations.

This is the characteristic which allows the Hall viscosity to be detected by an ultrasound experiment: of the three components of the elastic tensor, only Hall viscosity results in circular polarized normal modes. Crucially, the difference in the speed of sound between left and right handed modes is odd under time reversal. As we will see in the next section these two features, unique to the odd viscosity, allow us to isolate and detect the Hall viscosity in an experiment.

2.3 Pulse Echo Ultrasound - Hardware

The Hall viscosity causes dissipationless mixing of sound modes. Of particular interest to us are elements of the Hall viscosity tensor that mix different shear modes. In this case, the effect of the viscosity is to rotate the transverse polarization of the shear mode as a sound wave propagates. Here we describe the pulse echo method, which can be used to detect the polarization rotation and measure elements of the Hall viscosity tensor.

2.3.1 Overview of the method

The pulse echo method is a tool for measuring the speed and attenuation of sound waves of a particular frequency, propagation direction, and polarization. The experiment consists of applying a short pulse of stress and allowing the resulting strain wave to travel through the sample. The strain wave bounces back and forth "echoing" between the sample boundaries and is read out by monitoring the strain at the sample surface. The injection and detection of strain is normally done with a piezoelectric element, which converts electric field to strain and strain to electric field. This allows the strain wave to be generated by applying a voltage and the returning echoes to be measured with a voltmeter.

To ground ourselves in reality, we consider the typical time and length scales of the experiment. Your run-of-the-mill crystal of quantum material can be grown with dimensions of $\ell \sim 1$ mm. The typical speed of sound in a solid is $v \sim 3000$ m/s, so the time is takes a pulse of sound to travel across the sample will be $t \sim 300$ ns. For a measurement of this type to be meaningful, the width of the sound pulse must be less than the time between successive reflections, this means we work with pulse widths $w \sim 30$ ns. Finally, to make a phase sensitive measurement (to be described in a moment), we want many periods of the soundwave to be within a single pulse. This requires the frequency to be $f \sim 0.5$ GHz. Equivalently, we are working with sound wave lengths of $\lambda \sim 5$ μm. These numbers vary, of course, but that is the right idea.

The quantities we have access to are the time of flight, the phase of the return pulse, and its amplitude. Clearly, the time to traverse the sample gives the speed of sound $v = \ell/t$. However, the thickness is difficult to measure to better than one percent, which puts a bound on the precision of the absolute value of the speed of sound. The phase of the return echo,

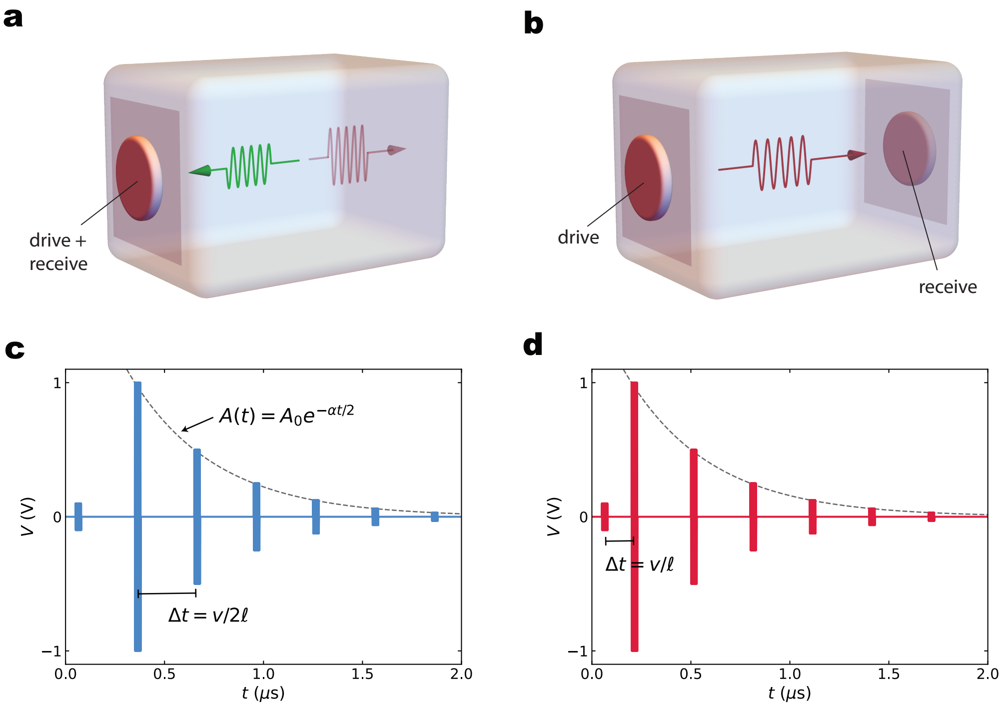

Figure 2.2: **Schematic of the pulse echo experiment:** In the pulse echo experiment, a strain pulse is injected into a crystalline sample using a piezoelectric transducer. The pulse propagates through the sample, reflecting off the sample boundaries, and is detected either by the same transducer used to excite the strain wave (**a**) in reflection mode, or using a second transducer on the opposite face of the sample (**b**) in transmission mode. The raw data, in both experimental configurations, is a series of "echoes" spaced in time by $\Delta t = v/2\ell$, where v is the speed of sound and ℓ the sample thickness. The echo amplitudes decay exponentially according to the attenuation, α, of the sound wave. (**c**) In the reflection experiment, the first detected echo arrives $t_0 = v/2\ell$ after the initial excitation, and subsequent echoes arrive at $2t_0, 3t_0, ...$ **d** In the transmission experiment, the first detected echo arrives $t_0 = v/\ell$ after the initial excitation, and subsequent echoes arrive at $3t_0, 5t_0, ...$

however, increases the precision many orders of magnitude if we are only interested in the relative changes in the speed of sound. To see this, note that the total phase accumulated during the time t is

$$\phi = 2\pi\frac{\ell}{\lambda} = 2\pi\frac{\ell f}{v} \implies \delta\phi = -2\pi\frac{\ell f}{v}\frac{\delta v}{v} = -\phi\frac{\delta v}{v}. \tag{2.28}$$

For our typical dimensions, the total phase is $\phi \sim 1000$ rad and we can estimate the uncertainty in the phase as $\Delta\phi \sim 1/\sqrt{wfN}$, where wf is the number of periods in the pulse and N is the number of averages we take. A modern oscilloscope can average 10^4 waveforms, giving $\Delta\phi \sim 10^{-3}$ rad, by which we can reach precision on the order of $\delta v/v \sim 10^{-6}$ – about ten thousand times better than time-of-flight.

The second quantity to which we are sensitive is the amplitude of the incoming strain pulse. As discussed earlier, the strain wave does irreversible work on the crystal as it propagates, generating heat as quantified by the attenuation α, which measures the fractional energy loss per unit length. A fractional energy loss per unit length corresponds to an exponential decay of the initial amplitude, A_0

$$A(x) = A_0 e^{-\alpha x/2}, \tag{2.29}$$

where the factor of $1/2$ accounts for the fact that the energy is proportional to the amplitude squared. There are various annoying conventions for the units of attenuation, with the unfortunate fact that we have ten fingers meaning that the standard unit of decay assumes the base 10 logarithm (dB). If we stay in the natural base, the unit is neper (Np).

It is also important to note that the piezoelectric transducers used for excitation and detection of the strain are polarization specific, which is especially relevant to the measurement of Hall viscosity. This means that the strain wave is *generated* with a particular polarization and that we also *measure* a particular polarization.

In sequence, what happens in the pulse echo experiment is strain of an initial polarization is generated in the transducer by application of a voltage. This is converted to a stress of the same type in the sample which breaks into (possibly three) normal modes in the sample and propagates (at possibly three different speeds). When the strain from a normal mode is incident on the detecting transducer, it generates a strain which results in a voltage across the transducer, which can be read out on an oscilloscope.

That is the idealized experiment. Now the details.

2.3.2 The transducer

There are two broad classes of transducers used for the pulse echo experiment: bulk and thin film. The very earliest experiments employed very large ceramic piezoelectric rods coupled to the sample either with glue or a small amount of mechanical pressure. As the technique developed the transducers were miniaturized to both reduce experimental artifacts (described in more detail later) and to make the method compatible with smaller samples. These transducers were still bulk pieces of ceramic or single crystal (commonly lithium niobate) and bonded to the sample. This same period, however, saw the development of thin film transducers in which a ~ 1 μm layer of piezoelectric material (commonly cadmium sulfide or zinc oxide, later aluminum nitride) was sputtered directly on to the sample surface.

Thin film and bulk transducers are complementary in many ways, though the thin film offers some distinct advantages. Note that the response of a transducer as a function of frequency can, to first approximation, be regarded as that of a mechanical resonator clamped at one end (one face of the transducer is bonded to the sample). As such, the transducer of thickness t has a resonances when the frequency, f_n, is

$$f_n = \frac{v}{2t}(2n+1), \tag{2.30}$$

with n a non-negative integer and v is the speed of sound in the piezoelectric. The width of the response resonances will be defined by the mechanical quality factor of the piezoelectric, roughly in proportion to its crystallinity. The bulk transducer typically has thickness ~ 100 μm and a very high quality factor $\sim 10^3$. So the response is at discrete frequencies starting at and spaced by $v/2t \approx 25$ MHz, with minimal response between resonances.

In contrast, the thin film will have resonances in the gigahertz. Further, the sputtered film is typically granular and much more easily damped by the electrode used to contact the transducer. This results in a quality factor of order 1. Therefore, the thin film transducer is ideal for probing at larger drive frequency and allows for nearly continuous, broadband operation with gigahertz bandwidth.

Compared to the bulk piezo, the thin film also has the advantage of not requiring a bonding layer to attach it to the sample. The intert bonding layer both reduces the coupling between the transducer and sample and results in unwanted reflections as strain is transmitted between the transducer and sample. The lower quality factor of the thin film also reduces the amount of ringing artifacts in the experiment where, even though a short voltage pulse is applied, the resulting mechanical motion of the transducer may continue for significantly longer.

Though superior in many ways, the use of thin film transducers faded as the pulse echo technique became less common and the community waited for a new generation of heavy fermions to study by ultrasound. The experiments described in this thesis exclusively employ thin film zinc oxide transducers, which turn out to be very well suited to α-RuCl$_3$, a fragile material easily distorted by heavy glue.

The pulse echo experiment aims to measure the linear strain susceptibility of the sample. In the context of a pulse echo experiment, this means that we want small strains ($\varepsilon \ll 1$). To check that we are in the linear response regime, we need to estimate the size of the strain we apply. This turns out to be trickier than it might seem, but we can obtain an upper bound by considering the properties of the piezoelectric transducer. Before diving into specific materials, we can estimate the piezoelectric constant, p, by imagining a small electric dipole of order ea, where e is the electron charge and a the lattice constant, being stretched by an applied electric field against the lattice stiffness, giving

$$p = \frac{\delta\sigma}{\delta E} \approx \frac{e}{a^2}. \tag{2.31}$$

The piezoelectric constant is usually given in units of $\delta\varepsilon/\delta E$, so dividing by the elastic modulus gives the estimate $p \approx 10$ pm/V. In a pulse echo experiment we apply ~ 10 V to the 1 μm thick transducer, resulting in a small strain $\varepsilon \sim 10^{-4}$. This provides an upper bound, as the electrical impedance matching between the transducer and the voltage source results in a significant reduction in applied power. It is interesting to note that, though we are almost certainly in the linear response regime, a 2ω response does sometimes appear and is most likely due to heating of the sample.

An impedance mismatch occurs because the transducer is not a well controlled circuit element, but is typically driven by a 50 Ω voltage source.

It is a nice introduction to the physics of the piezoelectric to derive an expression for the impedance of the transducer.

To start, the piezoelectric effect describes the interconversion of electric field and strain. As such, it corresponds to a term in the free energy

$$U_p = p_{ijk} E_i \varepsilon_{jk} \tag{2.32}$$

where E_i is the component of the electric field, ε_{ij} is the strain, and p_{ijk} is the piezoelectric tensor. Because the electric field is inversion odd, a material must break inversion symmetry to exhibit a spontaneous piezoelectric effect. The number of independent piezoelectric coefficients is dictated by the point group symmetry of the material in the same way as the elements of the elastic tensor.

We consider a 1 dimensional model, with a transducer of thickness t and area A with dielectric consant ϵ and elastic modulus c_0. The piezoelectric coefficient will be p, which gives an energy density in terms of the strain and the displacement field, D

$$\mathcal{E}(\varepsilon, D) = \frac{c_0}{2}\varepsilon^2 + \frac{1}{2\epsilon}D^2 - p_0 D\varepsilon. \tag{2.33}$$

In the pulse echo experiment we apply the electric field E, for which we need the transformed energy in terms of E

$$U(\varepsilon, E) = \frac{\left(c_0 - \epsilon p_0^2\right)}{2}\varepsilon^2 - \frac{\epsilon}{2}E^2 - \epsilon p_0 E\varepsilon \equiv \frac{c}{2}\varepsilon^2 - \frac{\epsilon}{2}E^2 - pE\varepsilon, \tag{2.34}$$

where $c = c_0 - \epsilon p^2$ is the reduced speed of sound in the polarized state. This gives the stress and electrical displacement field

$$D = -\frac{\partial U}{\partial E} = \epsilon E + p\varepsilon \tag{2.35}$$

$$\sigma = \frac{\partial U}{\partial \varepsilon} = c\varepsilon - pE, \tag{2.36}$$

The top side of the transducer at height t is assumed free, so there is no stress at the top. The stress at the bottom will be left un specified for now. For harmonic displacements $u = u_+ e^{i(\omega t - kx)} + u_- e^{i(\omega t + kx)}$ with wavelength $\lambda = 2\pi/k$ and frequency ω we get

$$0 = ikc\,(u_+ - u_-) - pE \tag{2.37}$$

$$\sigma = ikc\left(u_+e^{i\phi} - u_-e^{-i\phi}\right) - pE, \tag{2.38}$$

where we have written $kt = \phi$ is the phase lag across the transducer. Now the voltage different across the transducer is the integral of the electric field

$$V = \int dxE(x) = \frac{1}{\epsilon}\int dx\,(D - p\varepsilon) == Dt - \frac{p}{\epsilon}\left(u_+(e^{i\phi} - 1) + u_-(e^{-i\phi} - 1)\right). \tag{2.39}$$

Additionally, there is a bound charge on the surface of the transducer

$$q_b = AD, \tag{2.40}$$

which generates a current $i\omega AD$. This gives the impedance

$$Z = \frac{V}{I} = \frac{1}{i\omega C}\left(1 + k_c^2\left(1 + \frac{\sigma}{2pD}\right)\frac{\tan(\phi/2)}{\phi/2}\right) \tag{2.41}$$

where we have defined the coupling constant $k_c^2 = p^2/\epsilon c$, which is the ratio of elastic to electrical energy densities in equilibrium. The boundary stress σ will depend on the situation. We give here the result for the case when the transducer is attached to a sample of length much longer than the ultrasound pulse, so the sample can we considered semi-infinite. (The result change in the case on continuous wave excitation in which standing waves can appear.)

$$Z = \frac{1}{i\omega C}\left(1 - \frac{k_c^2}{\phi}\frac{2Z_t(\cos(\phi) - 1) - iZ_s\sin(\phi)}{iZ_s\cos(\phi) + Z_t\sin(\phi)}\right), \tag{2.42}$$

where Z_t and Z_s are the acoustic impedances of the transducer and sample respectively. This reduces to the result above for the free transducer case $\sigma = Z_s = 0$. Note that the overall behavior is capacitive, where the interaction with the sample controls when energy will be converted to an acoustic wave inside the sample. From the expression for the impedance we can define an effect resistance, capacitance and inductance, from which

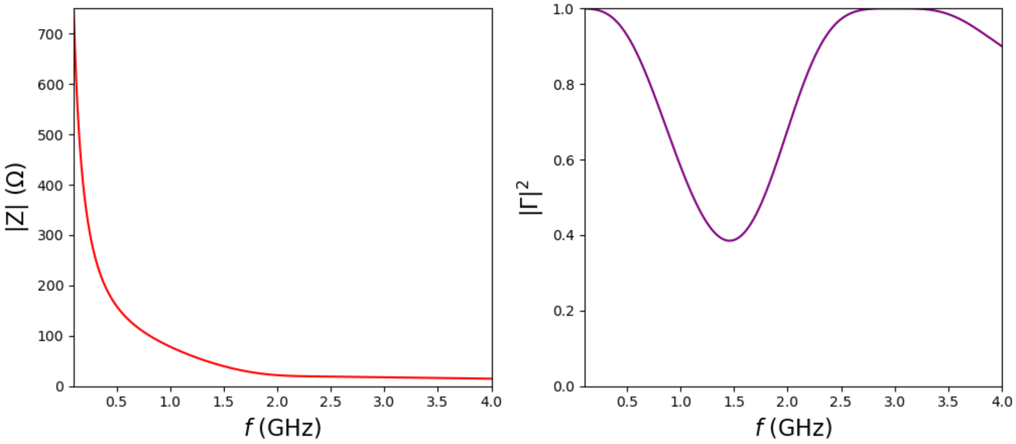

Figure 2.3: **Impedance of the transducer:** Here we plot the magnitude of the impedance (**a**) and the power reflection coefficient (**b**) for a 50 Ω source using the model Equation 2.42 assuming typical transducer parameters. We take the sample and piezo acoustic impedances equal, use the dielectric constant of ZnO, and transducer dimensions 200 μm laterally and 1 μm thick. The impedance is largeley capacitive. The reflection coefficient dips near 1.5 GHz, where the transducer has a resonance and can transmit acoustic energy into the sample. The width of the resonance in this model is set by the inverse of the coupling $Q \sim 1/k_c$.

we can find the center frequency $\omega_0 \sim v/t$ as expected, and the quality factor $Q \sim 1/k_c$ – so the resonance is sharper the better the conversion between acoustic and electrical energies.

The model actually compares favorably with measurements of the impedance on as fabricated transducers. However, because the VNA impedance measurement has more in common with the continuous wave excitation (where the sample cannot be considered semi-infinite), we delay looking at those data, which have some very beautiful features related to the quasi-continuous wave excitation.

The impedance mismatch between the driving source and the transducer is a both a feature and a bug. Clearly we need to inject ultrasound into the sample to measure anything. However, if the transducer is perfectly matched to the source we will not get multiple reflections within the sample, which is sometimes useful for sanity checking features in the data. More fundamentally, the necessity of exchanging energy with the waveguide used to excite the sample makes obtaining an absolute value for the ultrasound attenuation almost impossible without detailed knowledge of the coupling. However, the prospect of driving a large acoustic energy with very little voltage is appealing, as large voltages inevitably heats the sample at the lowest temperatures. The utility of impedance matching probably scales as one over the temperature.

Lastly, we comment on the deficiencies of the model presented here in speaking to the real experiment. We have neglected entirely the contact between the waveguide and the sample, which is a mess of paint and wire. Additionally, this simplified model assumes only a single mode is excited, which is not true in a multimode transducer where shear and compressional waves are excited simultaneously.

2.3.3 ZnO (on tilt)

Having understood the electrical characteristics of the transducer fully, we move to the specific piezoelectric material, zinc oxide, used in the experiments discussed later. Stoichiometric zinc oxide crystallizes in the hexagonal point group C_{6v}, in which the coordinate z transforms as a scalar allowing a spontaneous c-axis electrical polarization. The symmetry allows for three independent piezoelectric coefficients, which contribute to the free energy

$$U_{piezo} = d_{33}E_z\varepsilon_{zz} + d_{31}E_z\varepsilon_{x^2+y^2} + d_{15}\left\{E_x, E_y\right\} \cdot \{\varepsilon_{55}, \varepsilon_{44}\}\,. \tag{2.43}$$

The values are in the range of $d_{33} = 12$ pm/V, $d_{31} = -5$ pm/V, and $d_{15} = -5$ pm/V. Therefore, we calculate the induced stress, $\hat{\sigma}$, on application of the electric field $\mathbf{E} = \cos(\theta)\hat{z} + \sin(\theta)\hat{x}$, tilted an angle θ away from the c-axis

$$\hat{\sigma} = d_{33}\cos(\theta)\sigma_{zz} + d_{31}\cos(\theta)\sigma_{x^2+y^2} + d_{15}\sin(\theta)\sigma_{44}, \tag{2.44}$$

and we develop a compressional stress both perpendicular and parallel to the c-axis, in addition to a shear stress polarized along the in-plane direction of the electric field.

To make things relevant to the experiment, if we have a zinc oxide film on a sample, then the direction of the electric field will be normal to the film and the strain wave we generate will also travel normal to the film, into the sample. From Equation 2.44 we know that if the c-axis of the film is normal to the sample surface we only generate compressional strain.

Figure 2.4 shows the situation in general, we can ask how much of each type of strain we active for a given electric field direction , set, now, by the direction of the film c-axis relative to the sample normal, θ. This will be proportional to $A(\theta) = p_{ijk}\hat{E}_i\hat{u}_j\hat{k}_k$, where $\hat{E}$ is the electric field direction, $\hat{u}$ is the direction of the displacement in the strain, and $\hat{k}$ is its propagation direction in the sample, where $\hat{E} = \hat{k}$ by necessity. As the c-axis is tilted away from the sample normal, we exchange compressional strain for shear strain. The compressional strain vanishes entirely at $\theta \approx 40^\circ$ because of the competition between positive and negative piezoelectric coefficients.

In a tilted zinc oxide transducer, where the sample normal is neither in the plane or along the c-axis of the zinc oxide, the waves generated are referred to as quasi-longitudinal and quasi-shear. Remember, though, that if the waves in the crystal are *pure* transverse and compressional waves (ie the propagation direction is along a high symmetry direction of the *sample*), then the incoming wave in the zinc oxide will generate a mix of shear and compressional waves in the zinc oxide. This can result in the re-emission of a mixed wave – so only shear is incident on the transducer, for example, but shear and compressional waves are launched back into the sample.

2.3.4 Growth

Zinc oxide preferentially grows with the c-axis normal to the sample surface resulting in pure compressional sound. However, measuring the Hall viscosity requires the generation of shear waves. For this reason we develop a method of sputtering inclined c-axis films, which results in a mixed-mode film that generates both longitudinal and transverse waves.

We fabricate the zinc oxide thin films by sputtering deposition. We perform all depositions in a 4-gun Angstrom Engineering NexDep magnetron sputtering system, with the sample mounted above the sputtering targets.

The transducer consists of three layers: a bottom Ti/Pt layer (8nm/100nm), an $\sim 1\ \mu$m layer of piezoelectric ZnO, and a top layer of

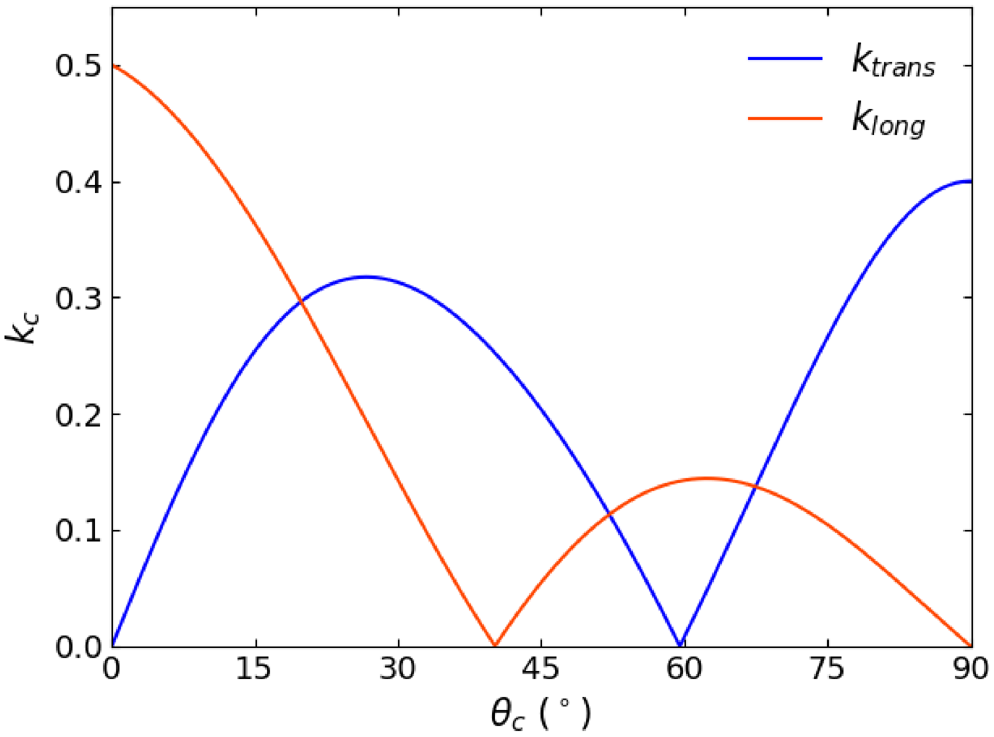

Figure 2.4: **Angle dependence of stress generated in the ZnO film:** The amount of stress generated by the zinc oxide transducer is a function of the angle between the piezoelectric's crystalline c-axis and the applied electric field. A thin film grown on a sample surface is most easily excited by an electric field normal to the film. Here, we plot the amount of longitudinal (k_{long}) and transverse (k_{trans}) stress generated as a function of the angle between the ZnO c-axis and the applied electric field. With the c-axis normal to the sample surface, only longitudinal waves are generated. However, is the c-axis is tilted away from the sample normal, we generate both longitudinal and transverse waves.

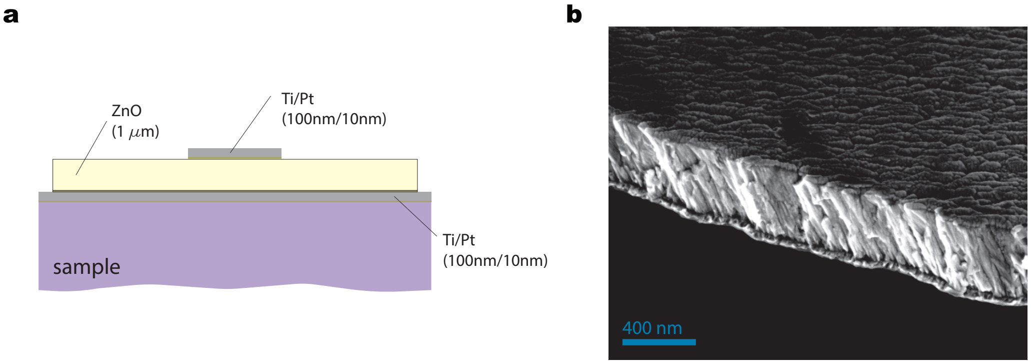

Figure 2.5: **Transducer fabrication:** we use sputtered thin films of zinc oxide as the piezoelectric transducer in the pulse echo experiment. (**a**) is a schematic of the material stack. The bottom electrode is 100 nm of DC sputtered platinum covering the entire surface of the sample. The active ZnO layer, approximately 1 μm thick, is RF sputtered in a 3:1 mixture of Ar:O gas at 3 mtorr. A second 100 nm layer of platinum forms a top electrode. Alternatively, silver paint is used as a top electrode. In the fabrication process, a 10 nm sticking layer of titanium is sputtered before each layer of platinum or zinc oxide. By sputtering the zinc oxide at a fixed, oblique angle relative to the sample, we grow inclined c-axis ZnO films. (**b**) shows an SEM micrograph of the film cross section. The bright white material in the center is ZnO, which grows in columnar grains with the crystal c-axis along the major axis of the column. The image shows grains approximately 100 nm in diameter growing at an angle of $\sim$ 22° relative to the surface normal. The tilted c-axis film allows simultaneous generation of compressional and shear strain.

Ti/Pt (8nm/100nm). The bottom metallic layer ensures adhesion of the ZnO to the sample surface and functions as a ground electrode for the transducer. The top metallic stack serves as an electrode for excitation and read out. Both metal layers are DC sputtered in a pure argon environment.

We deposit the piezoelectric ZnO layer by RF sputtering with a 2 inch diameter, 99.99% purity ZnO target. We use a 1:3 ratio of oxygen to argon flow rates at a total pressure of 3 mTorr. The deposition rate is approximately 0.2 /s using a power density of 21 $\mathrm{W/in^2}$.

The polarization of the transducer is determined by the c axis orientation of the ZnO layer. For shear-polarized transducers, we use "glancing angle deposition" to orient the ZnO c axis away from sample surface normal. To achieve this, we position the sample as far from the sputtering target as our chamber allows, and keep the sample stage fixed (i.e. no rotation) during deposition. The angle of incidence of ZnO ions on the sample surface in our sputtering chamber is approximately 70° away from the surface normal. The resulting ZnO films have their c axis tilted away from the sample surface normal along the straight line connecting the sample and target. This process results in a transducer that generates both compressional and shear stress in the sample. The polarization of the shear stresses is in the direction of the ZnO c axis tilt.

The measurements of the Hall viscosity will be done in a transmission configuration, in which two mixed-mode transducers are used in the experiment: one to excite the strain wave and a second, on the opposite side of the sample, to detect it. To facilitate antisymmetrization of the data as a function of magnetic field, enabling a more sensitive detection of the Hall viscosity, the transverse polarization of one transducer is rotated 45° with respect to the transverse polarization of the other transducer: this allows differentiation between "rotation left" vs "rotation right". A precise 45° misalignment is not necessary to perform the antisymmetrization, but maximizes the size of antisymmetric signal in the presence of viscosity. A full accounting of the experiment protocol is given in the later chapters on YIG and α-$\mathrm{RuCl_3}$.

2.3.5 Sample preparation

The Platonic ideal of the pulse echo sample is an infinite slab 300 μm thick. In pratice, we start with a possibly unoriented chunk of crystal and approximate the ideal as best we can. One first aligns the crystal according to the elastic moduli that are will be measured in the experiment using Laue backscattering x-ray diffraction. The Laue pattern must be matched to a simulated diffraction pattern to determine the orientation. An alignment of $\sim 1^\circ$ is possible.

To do a reflectometry experiment, the strain pulse must also make it back to the drive transducer, requiring that the sample faces between which the strain wave bounces be parallel. This is accomplished by hand polishing the sample on a precision machined polishing puck. After aligning the sample by Laue on the polishing puck, the first side can be polished knowing that the alignment is maintained. The sample can then be flipped and, if it is re-bonded flush against the polishing puck, the second side can be polished parallel to the first. It is often good to re-check the alignment with x-ray diffraction before polishing the second face, ensuring that parallel faces will be obtained.

The thin film transducer is $\sim 1\ \mu$m thick; therefore, the sample's surface roughness must be much less than 1 μm. Starting with an unpolished sample, we polish with successively finer grit polishing paper, finishing with a 10 nm grit. Polishing is done using either methanol or isopropanol as lubricant. Care must be taken to avoid scratches during the polishing process, regularly removing material that has been polished away. All the polishing surfaces and the polishing puck must be kept as clean as possible.

Before being loaded in the sputtering chamber, samples are cleaned with acetone, methanol, and isopropanol. The cleaning process will depend on the fragility of the sample. Sonication for ~ 5 min in each solvent is best if possible. Samples can then be dried with dry air and mounted on a glass slide with silver paint for sputtering.

Particularly delicate samples, like α-RuCl$_3$, cannot be polished or sonicated and the transducer must be grown on a cleaved face. Such delicate samples are handled only with a brush and never with tweezers.

For metallic samples, the sample bulk is electrically contiguous with the transducer bottom electrode, and the sputtering process can be done without breaking vacuum. For semiconducting or insulating samples, the sample is removed from the sputtering chamber after the bottom electrode has been deposited and, to allow access to the bottom electrode after the zinc oxide layer has been sputtered, a small dot of silver paint is placed in the corner of the sample away from where the top electrode will be made.

This acts as a mask and can be washed away with solvent later.

After the transducer is deposited, the sample is mounted on a PCB for measurement. Samples are bonded to the ground plane of the PCB with GE varnish for mechanical stability. When it is particularly important that the sample not move, or if the sample will experience large forces during the experiment (ie a magnetic sample in a large magnetic field) then angstrom bond or Stycase epoxy can be used in place of varnish. Additional support for the sample can be given using pieces of glass slide attached to the PCB.

The electrical connections to the transducer top and bottom electrodes are made either directly to the PCB ground plane (bottom electrode) or from the sample to the ground plane or signal wave guide using 99.99% purity, 25 μm diameter silver wire. Contacts are painted by hand using DuPont silver paste (solvent?).

Contacts painted by hand are typically limited to > 100 μm in diameter (though, of course, sometimes we get lucky). If a particularly small diameter contact is desired, the following trick is useful. Prepare a very thin mixture of GE varnish and toluene-ethanol. The mixture should be nearly transparent. Spread a layer of the thinned varnish on the surface of the sample where you want to make contact. The varnish will dry to form a thin insulating layer over the zinc oxide. Wait until the layer is partially dry ($\sim$ 30 min), then, using a 2 μm diameter TEM tip, poke a small hole in the varnish layer. It should be possible to make a hole about 30 μm in diameter. After the varnish dries completely, contact can be made using silver paste applied over the hole.

2.3.6 Electronics

Figure 2.6 shows the measurement circuit for the ultrasound experiment in transmission mode. We use a Tektronix TSG 4106A signal generator to generate RF pulses. We set the pulse position, width, and repetition frequency by external pulse modulation of the RF source supplied by a Tektronix AFG 3100 arbitrary waveform generator. Before arriving at the drive transducer the RF pulse is amplified by a Mini Circuits ZHL-42W+ power amplifier. The transmitted ultrasound excites the receive transducer, which is connected to a low noise Mini Circuits ZX60-83LN-S+ amplifier in series with a ZHL-42W+ power amplifier. We record the ampli-

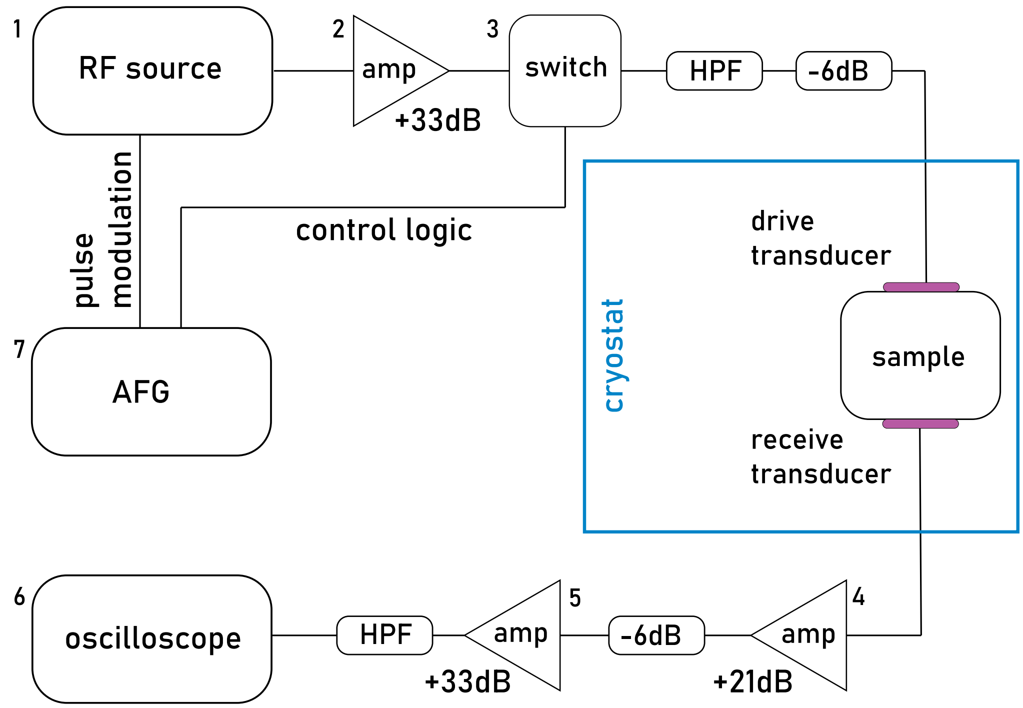

Figure 2.6: **Measurment circuit:** Schematic of the measurement circuit, starting from the top left and moving clockwise. We generate RF pulses at the transducer drive frequency (~1 GHz) using a Tektronix TSG 4106A signal generator (1). The source is pulse modulated using a Tektronix AFG 3100 waveform generator (7) to output ~30 ns square pulses at a repetition frequency of ~100 kHz. The RF pulse is further amplified by a Mini Circuits ZHL-42W+ power amplifier with 33 dB gain (2). The pulse is then fed through a Mini Circuits ZFWA2-63DR+ switch (3) to isolate the sample and downstream circuit from the power amplifier after the initial drive pulse is sent to the transducer. The switch logic is controlled by a second channel on the AFG 3100 generator (7). Before reaching the sample, the pulse is high-pass-filtered (HPFed) to remove switching noise and attenuated to minimize unwanted reflections from the transducer. The signal at the receive transducer – the transmitted ultrasound – is amplified twice, first by a low noise Mini Circuits ZX60-83LN-S+ (4) then by a second ZHL-42W+ power amplifier (5) before being filtered and recorded on a Tektronix MSO 6 Series oscilloscope (6).

fied signal from the receive transducer on a Tektronix MSO 6 Series oscilloscope. We use Mini Circuits ZFWA2-63DR+ switches to isolate the RF source and pulse amplifier from the oscilloscope. The switch logic is controlled by the AFG 3100 waveform generator.

For the experiment in the reflection configuration, in which a single transducer is used to both excite and detect the ultrasound, the same circuit can be used with only one modification. The receive amplifier (element 4 in Figure 2.6) is attached to the third port of the switch (element 3 in Figure 2.6). In this way, the switching logic allows a single transducer to be driven and then read out on the oscilloscope. Given a typical echo spacing of $\sim$ 100 ns, this requires a switch that can toggle in tens of nanoseconds.

In all cases the oscilloscope is sequence triggered using the TTL of the switching logic function generator (first trigger) in combination with a split copy of the RF pulse (second trigger). This provides a more stable method of averaging than a simple edge trigger, typically increasing signal to noise by a factor of two.

2.4 Pulse Echo Ultrasound - Software

All data were collected using custom-built software written in Python using primarily the PyQt module. We use the twisted module for asynchronous control and collection. With the advent of large language models, the task of putting together data collection user interfaces became trivial. Thank god.

In all experiments, our raw data is the amplified voltage across the transducer as a function of time. A typical example is shown in Figure 2.7a. The MSO 6 series oscilloscope we used has a 6 GHz bandwidth and we normally collect data with 40 ps between points, or roughly 10 points per period of the ultrasound excitation. A typical trace is approximately 5 μs in duration.

Precise triggering is necessary to avoid smearing out the phase of each pulse. To maximize signal to noise we employ sequence triggering in which the scope is first triggered by the gating pulse sent to the switches, and the secondary trigger is a split copy of the RF pulse sent to the sample. The repetition rate of the RF pulses is normally 10 kHz, which is just above the frequency at which the scope can collect data in fast acquisition mode.

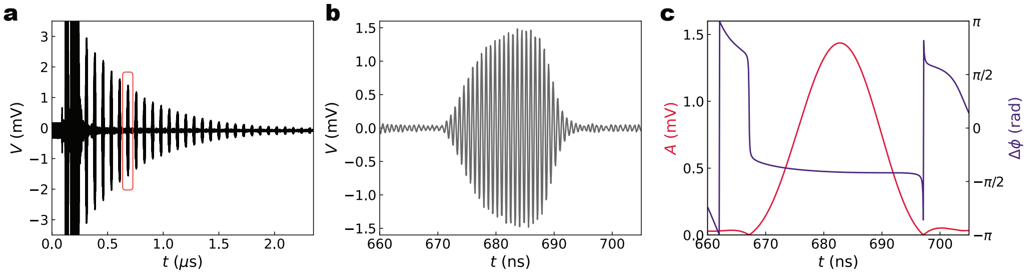

Figure 2.7: **Analyzing the data:** In the pulse echo experiment, we measure the voltage across a detection transducer as a function of time. (**a**) shows a typical raw echo pattern (compressional sound along the c-axis of CsV_3Sb_5 at 3.0 GHz and 350 mK). The echo spacing gives the absolute value of the speed of sound but does not allow sensitive measurement of changes in the sound velocity, which are typically part per thousand or smaller. To increase the precision of the measurement, we consider the phase of the excitation at each echo. (**b**) illustrates the raw signal at a single echo within the rectangle in panel **a**, which can be analyzed by digital lockin. The phase of that echo, along with its amplitude, are shown in (**c**). By recording the phase of echo at the amplitude peak, we can achieve part per million precion in tracking changes in the speed of sound as a function of temperature or applied magnetic field.

Typically we average 10^4 waveforms while continuously sweeping either the magnetic field or temperature. In fast acquisition mode, 10^4 averages are collected in $\sim$ 10s for a 10^5 point waveform. To avoid smearing out features in the data, either the field/temperature ramp rate must be slow compared to features in the speed of sound or attenuation. Alternatively, a the data can be collected a series of discrete points in the external parameter, which also allows for extended averaging if increased signal to noise is required.

2.4.1 Data processing

To extract the relative change in the speed of sound and attenuation, we need the phase and amplitude of the ultrasound echoes. Because a standard commercial lockin amplifier requires a continuous wave input, we use digital lockin on our pulsed signal. Figure 2.7b-c shows a single echo in the time domain along with the processed data obtained by digital lockin. The digital lockin is performed in software by the following steps:

The raw signal, $S(t)$, is separated into in-phase, $I(t)$, and quadrature, $Q(t)$, components at the drive frequency ω

$$I(t) = S(t)\cos(2\pi f t) \qquad Q(t) = S(t)\sin(2\pi f t), \tag{2.45}$$

from which the DC component is extracted using a digital, phase-lag-free low pass filter.

The filter implementation is in scipy butterworth, which constructs a lowpass response function $H(s) = A_{out}(s)/A_{in}(s)$, where A_{out} and A_{in} are the (complex) output and input to the filter decomposed into decaying/growing sinusoids, $s = i\omega + \alpha$. The response function, $H(s)$, is chosen to be the ratio of polynomials $H = P/Q$ which, in the time domain, defines an ordinary differential equation relating the input to the output data $\hat{P}A_{in}(t) = \hat{Q}A_{out}(t)$, where $\hat{P}$, $\hat{Q}$ are time-domain differential operators (polynomials in d/dt). The differential equation is converted to a finite difference equation, which is solved by moving through the data in one direction or another. The zero-phase-lag version does it once forward and another time backwards.

The lowpass cutoff of the filter must be set low enough to remove unwanted noise, but not so low that it washes out the shape of each pulse in the echo train. In practice, for a pulse width of $w \sim 30$ ns, a lowpass cutoff of $\sim 1/w = 30$ MHz works reasonably well.

After lowpass filtering the amplitude, $A(t)$, and phase change $\phi(t)$, of the data at the drive frequency are

$$A(t) = \sqrt{I(t)^2 + Q(t)^2} \qquad \phi(t) = \tan^{-1}\left(\frac{Q(t)}{I(t)}\right) \tag{2.46}$$

Some artifacts are introduced a result of the filtering. First, because the filtering removes the higher frequency components of the square pulse which amplitude modulates the RF signal, side lobes appear in the amplitude of pulse envelope. Second, the phase of the pulse is distorted. This occurs because the low pass filter smoothly connects the phase within the pulse to the random phase of the noise outside the pulse. If the cutoff time constant is similar to the pulse width, the phase will have a sloping background over the width of the pulse. We do not see this in the amplitude because $\sqrt{I^2 + Q^2}$ is smooth as $(I, Q) \to (0, 0)$ but $\tan^{-1}(Q/I)$ is not. Because of these artifacts, it is important to check that features in the data are robust to the value of the low pass cutoff.

2.4.2 Speed of sound and attenuation

Using the phase and amplitude we can extract changes in the speed of sound and the ultrasound attenuation. Changes in the speed of sound are found by tracking the difference in phase of two echoes divided by the total phase between them:

$$-\frac{\delta v}{v} = \frac{\delta \phi}{\phi} = \frac{\phi_2 - \phi_1}{2\pi f t} \tag{2.47}$$

where ϕ_1, ϕ_2 are the phases at two echoes taken from the lockin, f is the drive frequency, and t is the time spacing between the echoes.

There is ambiguity in picking the points in time within each echo at which to evaluate the phase. We can estimate the error introduced by this ambiguity, which comes from two sources. First, as mentioned earlier, the digital filtering introduces a slope in the phase within the pulse, which changes ϕ_1 and ϕ_2 in Equation 2.47. The total change in phase across the echo is normally $\sim$ 1 mrad, introducing a systematic error $\sim 10^{-6}$ in the change in speed of sound. Second, the choice of where to evaluate the phase changes introduces uncertainty into the total phase via the echo spacing, t in Equation 2.47. This gives a maximum absolute uncertainty $\sim w/t$, where w is the pulse width, which can be almost 100%. This systematic is largely mitigated by being consistent in picking the positions within the pulse at which to evaluate the phase. Under the assumption that the envelope is static (as a function of external parameter) we use the position of the peak in amplitude.

This assumption, however, may not always hold. Changes in the envelope shape as a function of external parameter come most obviously from interference. In particular, the strain pulse has finite extent in space, which means different portions of the strain pulse interact with different parts of the sample. As an example, if the faces of the sample are not parallel, some parts of the pulse will travel a longer distance than others. The pulse can also reflect off the back of the transducer. Additionally, the sample has finite extent and the strain wave can bounce off the sample's lateral boundaries if the transducer is close to the sample edge.

This type of interference distorts both the amplitude and phase, but has an outsized effect on the amplitude as a function of propagation time. This is because the wavelength of the ultrasound is of the order 1 μm, which is similar to the path difference you might expect on reasonably but not perfectly parallel sample faces. Faces only 1° off parallel for a 200 μm diameter transducer result in path differences of a full wavelength between successive echoes. The sound wavelength is also similar to the thickness of the transducer. In any case, this can cause a path difference of order the wavelength to accumulate on each traversal of the sample, which can result in very dramatic departures from the exponential behavior expected from energy loss.

The wavelength itself also changes as a function of external parameter which, combined with path difference interference, can also alter the pulse shape. This can be understood qualitatively by considering the phase from a pulse reflected off a tilted boundary. If the maximum difference in path length between parts of the reflected signal is $\delta\ell$ (ie the boundary is tilted by ϕ and the spatial extent of the pulse is $\delta\ell/\tan(\phi)$), then the total reflected signal is distorted by an amount

$$\int_0^{\delta\ell} dy e^{iky} = e^{ik\delta\ell/2}\mathrm{sinc}\left(\frac{k\delta\ell}{2}\right) \tag{2.48}$$

where k is the sound wave vector. We see that the phase picks up an extra piece proportional to $k\delta\ell/2$. Because $\delta\ell$ will be proportional to the total distance the pulse travels (ie it picks up more path length difference on each reflection) there will be a different amount of distortion for each echo. For this reason, even though Equation 2.47 *should* give the same answer independent of which echoes are chosen, in an imperfect sample interference effects can give systematic differences between echo pairs.

Furthermore, as the wave vector changes by δk as, say, a function of temperature the systematic also changes by an amount $\delta\phi_s = \delta k\delta\ell = (\delta v/v)(k\delta\ell)$, where $\delta v/v$ is the fractional change in the speed of sound. For realistic values of $k \sim 3 \cdot 10^6$ m^{-1} and $\delta\ell \sim 1 - 10$ μm, we get a systematic phase distortion that is of order the fractional change in the speed of sound. When divided by the total phase between echoes, usually $\sim 10^3$ rad, we expect systematic error in the relative change in the speed of sound by less than one percent. Note that this effect becomes more pronounced, and the requirements of parallelism of the sample faces becomes more stringent, at higher frequency.

The ultrasound attenuation can be extracted by two methods. First, if the signal consists of many echoes, we can fit the set of echo amplitudes versus time to the exponential decay. However, because of the interference effects mentioned above, the fit is often unreliable unless there are many large amplitude echoes, which allows the interference to be averaged out. Additionally, as the amplitude of the echoes begins to hit the noise floor of the measurement circuit (which necessarily happens) we come up against the fact that the amplifiers used in the measurement are not perfectly linear, and tend to exhibit higher gain at lower amplitude.

A second method requires only a single echo. Writing the amplitude $A = A_0 e^{-\alpha(T)t/2}$ where A_0 is the initial excitation, t is the transit time, and $\alpha(T)$ is the temperature dependent attenuation, we can extract the difference in attenuation between temperature T and T_0 by

$$\Delta\alpha = \alpha(T) - \alpha(T_0) = -\frac{2}{t}\log\left(\frac{A(T)}{A(T_0)}\right). \tag{2.49}$$

This has the disadvantage that the interference effects come in directly. It also does not include the temperature dependence of the loss in the coaxial cables between the sample and the measurement electronics. Both of these effects can be significant if the temperature range in question is large.

Lastly, we note several reasons that the absolute value of the attenuation is particularly difficult to extract. The interaction of the ultrasound pulse with the transducer is non-negligible and results in energy loss unrelated to the properties of the sample. When the sample faces are not parallel, a fraction of the sound energy is also deflected away from the transducer and is not measured, an addition another source of loss unrelated to the sample. If the surface roughness of the sample is not completely negligible compared to the sound wavelength, diffuse scattering off the boundary can also decohere the sound pulse adding another loss channel unrelated to the bulk properties.

2.4.3 Extracting the Hall viscosity

Most relevant to our original mission, is how to take the pulse echo data, namely the amplitude of an echo as a function of applied magnetic field, and calculate the Hall viscosity. Recall that the Hall viscosity results in an antisymmetric in magnetic field amplitude due to the rotation of transverse polarization. Our experiment consist of two transducers – one generating the strain wave and a second to detect it – which have shear polarizations rotated with respect to each other.

We use the equations of motion—Equation 2.24—to model the ultrasound experiment. Our experiment consists of launching a strain wave along the c axis with frequency ω and polarization at angle ϕ_i in the x-y plane: $\mathbf{u}_i = (\cos(\phi_i), \sin(\phi_i))$. To obtain the amplitude that we measure at the receive transducer for a given value of the viscosity, we proceed in three steps.

First, we compute the normal mode wave vectors, $k_\pm$, and polarizations $\mathbf{u}_\pm$, using Equation 2.24. The initial polarization is then decomposed into the normal modes:

$$\mathbf{u}_i = \alpha \mathbf{u}_+ + \beta \mathbf{u}_-, \tag{2.50}$$

from which we can find the coefficients $\alpha = \mathbf{u}_+^\dagger \cdot \mathbf{u}_i$ and $\beta = \mathbf{u}_i^\dagger \cdot \mathbf{u}_i$. The phase of each mode after traveling the length of the sample, ℓ, is $e^{ik_\pm \ell}$. We then project each mode on to the polarization of the receive transducer $\mathbf{u}_f = (\cos(\phi_f), \sin(\phi_f))$, giving two contributions to the final (complex) amplitude, $\tilde{A}_\pm$ from each mode polarization $\mathbf{u}_\pm$

$$\tilde{A}_\pm = \left(\mathbf{u}_\pm^\dagger \cdot \mathbf{u}_i\right)\left(\mathbf{u}_f^\dagger \cdot \mathbf{u}_\pm\right) e^{ik_\pm \ell} \tag{2.51}$$

The receive transducer sees the sum of the two modes, and the amplitude we measure, A_m is the amplitude of the sum

$$A_m = \left|\tilde{A}_+ + \tilde{A}_-\right| \tag{2.52}$$

By flipping the sign of η in the model we form symmetrized and antisymmetrized amplitudes as a function of applied magnetic field. Because the antisymmetric amplitude alone is not a meaningful quantity in this context (it depends on the overall amplitude of the initial excitation, for example) we normalize the antisymmetric amplitude in the model and the data by the symmetric amplitude at zero applied magnetic field. To extract the viscosity as a function of applied magnetic field, we perform a one parameter fit to the ratio of the antisymmetric and zero field symmetric amplitudes using the model presented above. The value of viscosity as a function of magnetic field is found by minimizing the squared difference between the model output and the data.

Chapter 3

Hall viscosity and the Acoustic Faraday effect of YIG

Before attempting to measure the phonon Hall viscosity in frustrated magnets like α-RuCl$_3$, it is useful to first validate our experimental technique in a simpler and more controlled setting. For that reason, we study the acoustic Faraday rotation in yttrium iron garnet, $Y_3Fe_5O_{12}$ (YIG), a prototypical insulating magnet with a well-documented acoustic Faraday effect. [81, 82] This chapter begins with a brief review of the relevant properties of YIG, followed by our extension of previous measurements of the acoustic Faraday rotation and their interpretation in terms of Hall viscosity. Finally, we present our measurements of the thermal Hall conductivity of YIG and discuss their connection to the ultrasound data.

3.1 Introduction

The acoustic Faraday effect refers to the polarization rotation of transverse sound waves in a crystal. The simplest realization of the acoustic Faraday effect requires a material with three ingredients. First, the crystal structure must have an axis of at least three-fold rotational symmetry, ensuring that the two transverse sound modes are degenerate at zero applied magnetic field. Second, the material should host sharp, well-defined excitations that can be tuned with an external magnetic field and brought an energy comparable to the ultrasound drive frequency – this provides a means of controlling the strength of the Faraday rotation. Third, the sound

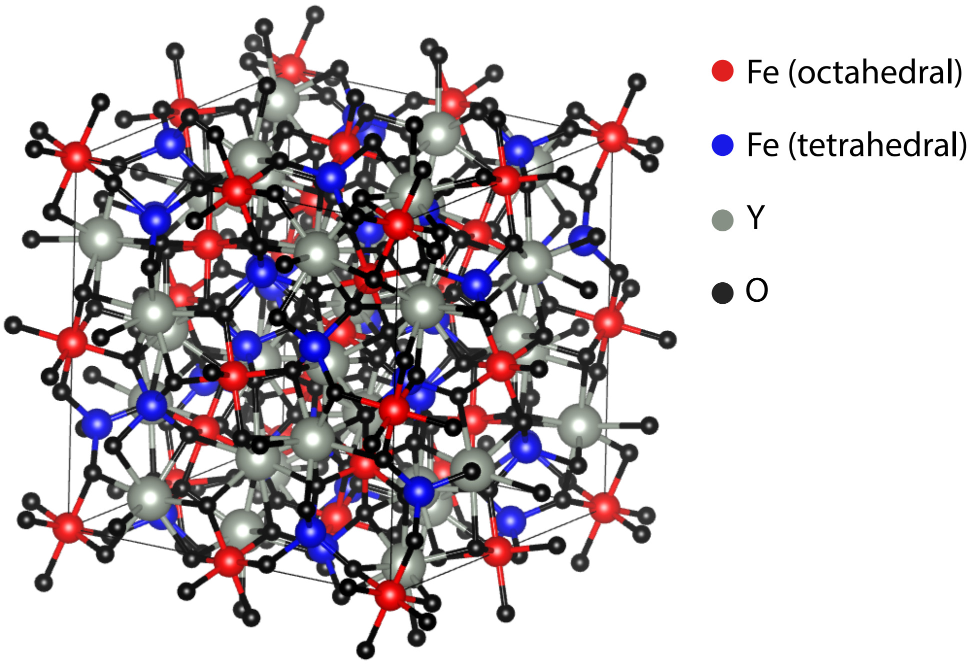

Figure 3.1: **Unit cell of YIG:** the cubic unit cell of YIG. Magnetically active iron atoms sit in two symmetry-distinct sites – half are surrounded by six oxygen atoms in an octahedral environment (blue) and half are surrounded by four oxygen atoms in a tetrahedral environment (green).

waves must interact strongly with the field-tunable excitation. We find all three of these ingredients in YIG, making it an ideal test case for acoustic Faraday rotation measurements.

YIG crystallizes with cubic symmetry (space group 230, point group O_h) with a unit cell consisting of eight formula units (160 atoms). The magnetically active Fe^{3+} atoms occupy sites with both octahedral and tetrahedral symmetry. Strong exchange interactions result in magnetic order, while spin orbit coupling and crystal field splitting cause very weak magnetic anisotropy, discussed in detail below. Recent refinements of neutron scattering data suggest that YIG exhibits slight rhombohedral distortion at low temperature; however, this distortion introduces only minor changes to the low-energy magnetic dispersion. [83, 84].

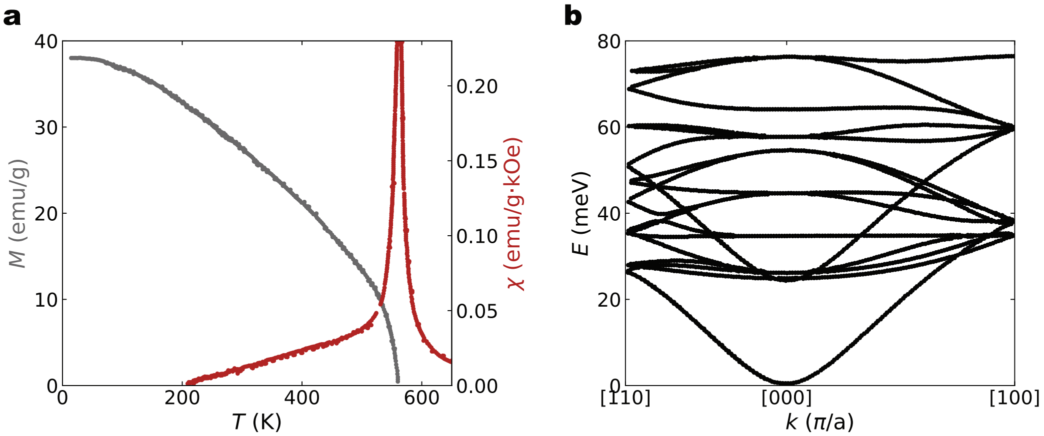

Figure 3.2: **Magnetic properties of YIG:** (**a**) Temperature dependence of the magnetic moment and magnetic susceptibility of YIG. Ferrimagnetic order onsets at ≈560 K, signaled by the appearance of a finite magnetic moment and a sharp spike in the magnetic susceptibility. (**b**) Magnon dispersion of YIG calculated using DFT. At low energy the dispersion is particularly simple, featuring a single parabolic band at $k = 0$ separated from higher energy excitations by nearly 200 K. Neutron scattering experiments show excellent agreement with the calculated dispersion. [83]

General interest in YIG arises from its exceptionally sharp low-energy magnetic excitations, which make it a model system for studying spin waves. [81] Magnetization measurements show that YIG develops a finite magnetic moment of $\sim 5\mu_B$/f.u. below $T_C \approx 560$ K. [85, 86] The Hund's rules imply that each of the five magnetically active iron atoms should contribute $5\mu_B$, so the relatively small magnetization indicates the magnetic moment of YIG is mostly compensated. The residual moment remains uncompensated at all temperatures below the ordering temperature, growing as the temperature is lowered. [87]

Ferromagnetic resonance measures a small negative anisotropy $K_1 \approx -600$ J/m^3, indicating that the magnetic easy axis lies along the crystaline [111] direction. [88] YIG's [111] easy axis, along the body diagonal, allows for eight possible domains. However, owing to its small anisotropy, the coercive field is exceptionally low ($H_c \approx 0.1$ mT) and the magnetic moment can be reoriented by a modest applied magnetic field, saturating on application of ~100 mT. [89] The exceptionally small anisotropy field, $H_a \approx 10$ mT implies a very small gap in the magnon spectrum on the order of a few μeV, consistent with low-energy neutron scattering. [88, 90] As mentioned earlier, this low-energy, field-tunable magnon gap will become important for realizing an acoustic Faraday effect in YIG.

For the purposes of this study, the most relevant property of YIG is its magnetoelastic coupling, which links applied magnetic field to induced strain. The static magnetostriction of YIG was first measured by incorporating a sample into a resonant cavity and tracking the shift in resonance frequency as a function of applied magnetic field. Using this method, Callen et al. reported a static magnetostriction of $6 \cdot 10^6$ erg/cm^3. [91] The sizable magnetostriction, together with YIG's cubic structure and sharp low-energy magnons, make it an ideal system in which to study acoustic Faraday rotation. Indeed, four years after Kittel proposed the effect, Matthews and Lecraw observed acoustic Faraday rotation in YIG using pulse echo ultrasound. [31] Modeling their data after Kittel's theory, they extracted a magnetoelastic coupling constant $7 \cdot 10^6$ erg/cm^3, in good agreement with the static magnetostriction. Follow up ultrasound experiments confirmed the Faraday rotation with reasonable quantitative agreement across experiments. [92, 82]

Having established YIG as an excellent reference material for acoustic Faraday effect measurements, we extend the existing data and validate the experimental method we will use later for α-RuCl$_3$. In particular, where previous work measured the Faraday response at a single frequency, we use broadband ultrasonic transducers to measure the effect continuously as a function of frequency. Although previous work found excellent agreement with Kittel's model, we incorporate additional experimental checks to strengthen the case that the observed signature of Faraday rotation – oscillations of the transmitted acoustic power as a function of applied magnetic field – is indeed a time-odd effect.

3.2 Ultrasound Data

We measure the ultrasound velocity and attenuation for compressional and transverse sound waves propagating along the [100] direction of YIG.

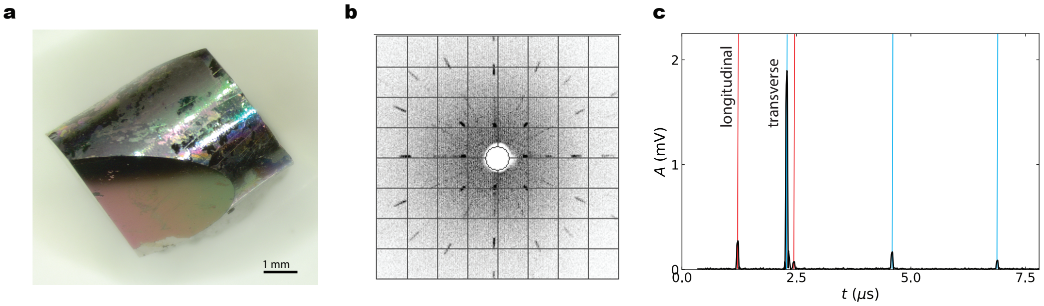

Figure 3.3: s
ample of YIG for pulse echo ultrasound measurement]**Ultrasound in YIG along [100]:** Preparation of the [100] aligned sample of YIG for the acoustic Faraday effect measurement. (**a**) The sample after being cut, aligned, and polished. (**b**) Laue pattern after alignment – clear four-fold rotational symmetry of the X-ray pattern indicates [100] alignment to ~1°. (**c**) Pulse echo pattern at 300 K with a drive frequency of 1.5 GHz. Two sets of decaying echoes are observed. The more closely spaced set of echoes, marked in red, correspond to compressional sound traveling at 7400 m/s. The slower, transverse sound, marked in blue, travels with velocity 3900 m/s. Both speeds of sound agree well with the literature.

Direction	Polarization	Velocity (m/s)	Modulus (GPa)
[100]	[100]	7400	280
[100]	[010]	3900	80

Table 3.1: **Elastic properties of YIG:** summary of the elastic properties of YIG releveant for the experiments presented in this section. The mass density is $\rho = 5.17$ g/cm^3.

The basic characteristics of the sample are shown in Figure 3.3. The sample was cut from a 1 cm rod of YIG purchased from OXIDE and oriented for the ultrasound experiment using Laue backscattering X-ray diffraction. After polishing parallel faces for transducer deposition, the distance between faces was 4.5 mm. A single transducer was deposited on one of the polished surfaces, and the resulting echo pattern at a drive frequency of 1.5 GHz is shown in Figure 3.3c. Two distinct echo trains are visible: the spacing between the smaller and larger amplitude sets of echoes corresponds to sound velocities of 7400 m/s and 3900 m/s respectively. These values are in good agreement with previous measurements of longitudinal and transverse sound waves propagating along [100] in YIG. [93] Identical measurements were performed on a [111] oriented cylinder of YIG. A summary of the elastic properties is given in Table 3.1

To measure the acoustic Faraday rotation we apply a magnetic field parallel to the sound propagation direction and record the amplitude and phase of the reflected ultrasound pulses. Figure 3.4b shows the amplitude of a transverse sound wave as a function of applied magnetic field at a temperature of 298 K and an ultrasound frequency of 1.40 GHz. At the lowest magnetic field values the amplitude drops sharply before recovering to about half its zero field value. With further increase of the magnetic field, the amplitude begins to oscillate and the period of oscillation decreases, becoming very rapid as the magnetic field approaches 130 mT. The oscillations then disappear for approximately 25 mT, after which the low-field pattern is reproduced in reverse.

Up to this point, our data reproduce previous reports of acoustic Faraday rotation in YIG, observed at a single frequency. Because our ultrasonic transducers operate continuously over a ~1 GHz bandwidth, we can also examine how the Faraday rotation evolves as a function of ultrasound frequency. Figure 3.4a shows the amplitude of transverse ultrasound as a function of applied magnetic field and frequency at a temperature of 298 K. The amplitude minima – visible as dark bands – disperse approximately linearly with frequency. Moving from high to low magnetic field starting at 300 mT, these bands of minima change slope and become more closely spaced in magnetic field. A similar pattern appears on moving from low to high magnetic field starting at zero tesla. In the intermediate field regime is a "dead zone" in which oscillations are absent over the full range of accessible frequencies. This broadband capability provides a further test of theoretical models of the acoustic Faraday effect.

YIG is an ideal system for observing the acoustic Faraday effect because high-quality crystals with low damping and large dimensions are easily grown. As a result, the polarization undergoes several full rotations before detection, producing pronounced oscillations in the detected amplitude. In this case, amplitude oscillations alone are highly suggestive of polarization rotation. However, in order to detect acoustic Faraday rotation in other systems – where either the effect is intrinsically much smaller or large single crystals are not available – we develop an experimental pro-

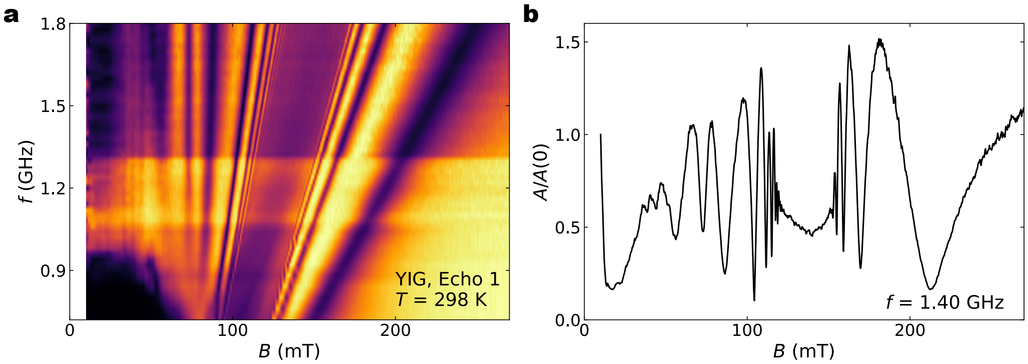

Figure 3.4:]
Acoustic Faraday rotation of YIG: (**a**) shows the measured amplitude of a reflected transverse sound wave as function of applied magnetic field and frequency. Both the sound wave vector and the magnetic field are along the [100] direction of YIG. Black regions indicate minima of the amplitude and, at fixed frequency, there are clear oscillations of the amplitude as a function of magnetic field. As a function of frequency, the amplitude minima disperse linearly. (**b**) shows a linecut of the data in **a** at a fixed frequency of 1.40 GHz normalized to the zero-field amplitude. The period of the amplitude oscillations in non-uniform in applied magnetic field. The period decreases on approaching ~130 mT from both the high-field and low-field directions.

tocol capable of isolating the Faraday rotation even when the polarization rotates by less than 2π. Beyond extending the range of materials in which Faraday rotation can be detected, this technique shows definitively that the “handedness” of the polarization rotation is odd under time-reversal – a defining feature of the acoustic Faraday effect that cannot be established in the simplest experimental configuration.

To that end we perform measurements in transmission mode, in which two transducers are grown on opposing faces of the YIG sample. The polarization of the two transducers is misaligned by 45° and one transducer is used to generate the ultrasound pulse and the second, receive transducer is used to detect incoming strain waves on the opposite side of the sample. As illustrated in Figure 3.5, misaligning the transducers allows us to distinguish clockwise and counterclockwise rotation because, in this configuration, the receive transducer polarization is rotated relative to the drive transducer polarization with a definite handedness. For that reason, starting from no rotation, clockwise polarization rotation cause the amplitude at the receive transducer to increase, whereas counterclockwise rotation would cause the received amplitude to decrease. In contrast, in a reflection experiment, clockwise polarization rotation is indistinguishable from counterclockwise polarization rotation. This occurs because the response of a shear polarized transducer is proportional to the absolute value of the cosine of the angle between the incoming sound wave and the transducer polarization and does not depend on the sign of the angle.

The ability to distinguish clockwise and counterclockwise rotation allows us to perform two experiments to detect time-odd Faraday rotation. The First, we can perform the experiment in positive and negative applied magnetic field and antisymmetrize the data. Field-even effects, such as magnetic field dependent ultrasound attenuation, will cancel on antisymmetrization leaving only the field-odd amplitude changes due to polarization rotation. Magnetic field antisymmetrization has the advantage that we do not need to observe a full 2π rotation to detect the polarization rotation, and therefore translates well to very thin samples.

Second, because the each piezoelectric transducer can be used to both excite and detect ultrasound in the sample, we have the ability to interchange the drive and receive transducers in the experiment. This can be done by simply interchanging cables at room temperature and does not require remounting or realigning a sample. For an ultrasound pulse that travels one sample length before detection, switching drive and receive transducers has the effect of reversing the propagation direction of the ultrasound. This offers a second way to confirm the presence of polarization rotation: reversing the propagation direction switches the sign of the antisymmetric signal. We perform both magnetic field antisymmetrization and reversal of the propagation direction in our experiments on YIG.

Figure 3.6a shows the symmetric in magnetic field amplitude of a transverse ultrasound pulse as a function of applied magnetic field and frequency taken at 298 K. The same bands of minima appear in the transmission experiment as in reflection mode, Figure 3.4. While a reflection experiment has identical amplitude oscillations in positive and negative applied magnetic fields, the transmission experiment can confirm the time-odd nature of the effect. Figure 3.6b shows the antisymmetric in field signal over the same range of magnetic fields and frequencies as a. The amplitude

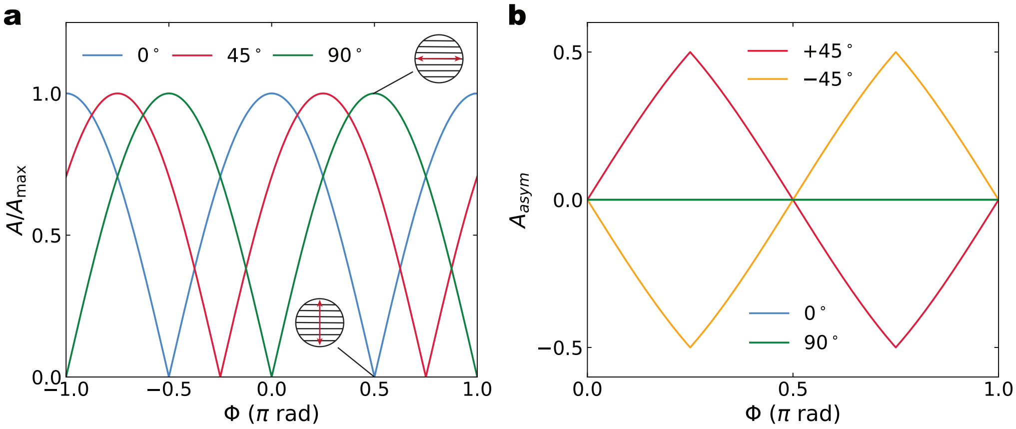

Figure 3.5: **Faraday rotation in transmission mode:** Measuring in transmission mode with misaligned transducer polarization allows us to isolate the acoustic Faraday rotation. (**a**) plots the normalized amplitude of the received signal as a function of polarization rotation angle for three transducer polarization misalignments. The position of the amplitude minima and maxima are determined by when the incoming soundwave polarization (red double arrows in the insets) is at 90° and 0° relative to the receiving transducer polarization (hatched black lines in the insets). Note that when the transducer polarization misalignment is 0° or 90°, the amplitude is an even function of rotation angle, whereas when the misalignment is 45° the amplitude is no longer identical for plus and minus rotation angle. To further illustrate the utility of transmission mode measurement, (**b**) shows the antisymmetric in rotation angle amplitude ($A(\Phi > 0) - A(\Phi < 0)$) as a function of rotation angle for different polarization misalignments. For 0° and 90° misalignments, there is no antisymmetric signal. For the ±45° misaligments, however, there is a non-zero antisymmetric signal with opposite sign for +45° and −45° misalignment.

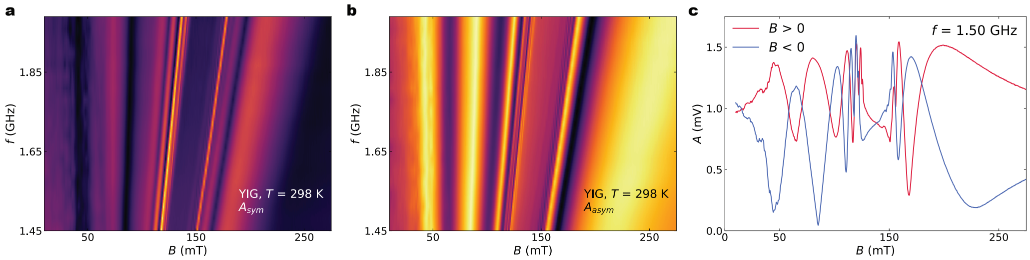

Figure 3.6: **Acoustic Faraday rotation in transmission mode:** To confirm that the polarization rotation we observe is a time-odd effect, we run our experiment in transmission mode, in which the strain pulse travels between two transducers with misaligned polarizations. In this configuration, an antisymmetric in magnetic field component of the signal indicates that the polarization rotation goes from clockwise to counterclockwise on reversing the direction of the magnetic field. (**a**) shows the symmetric in magnetic field amplitude, $A(B > 0) + A(B < 0)$, as a function of frequency and magnetic field. Dramatic amplitude oscillations are observed as in Figure 3.4. (**b**) shows the antisymmetric in magnetic field amplitude $A(B > 0) - A(B < 0)$ as a function of frequency and applied magnetic field. The oscillatory behavior survives antisymmetrization, confirming that the Faraday rotation is odd under time reversal. (**c**) illustrates a line cut at a fixed frequency of 1.60 GHz for both positive and negative magnetic field. The positions of the amplitude minima and maxima are interchanged under reversal of the magnetic field direction. Given the misalignment of the drive and receive transducers, this behavior is consistent with a time-odd polarization rotation.

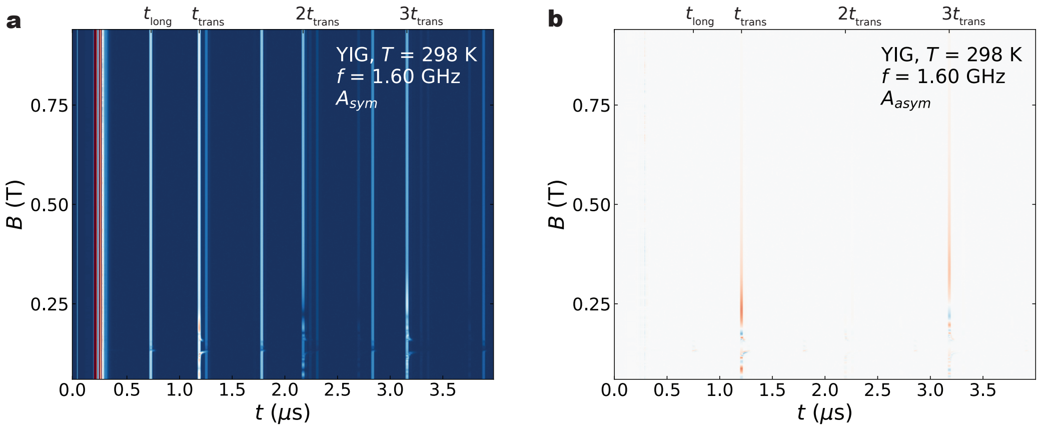

Figure 3.7: **Antisymmetrization of the full echo pattern:** In the transmission mode measurement of acoustic Faraday rotation, only transmitted shear sound survives magnetic field antisymmetrization. (**a**) shows the symmetric in magnetic field echo pattern as a function of applied magnetic field. Each vertical stripe is a received longitudinal or transverse strain wave, either transmitted through the sample (having traveled an odd number of sample lengths), or reflected (having traveled an even number of sample lengths). The longitudinal and transverse transit times are indicated on the top axis. (**b**) shows the same echo pattern antisymmetrized in magnetic field. All the echoes disappear except for the transmitted transverse sound at $t_{\rm trans}$ and $3t_{\rm trans}$, consistent with a time-odd Faraday rotation.

oscillations survive antisymmetrization, consistent with acoustic Faraday rotation.

To illustrate the extent of the difference between the positive and negative magnetic field data, Figure 3.6c shows the amplitude versus applied magnetic field at fixed frequency of 1.60 GHz for both magnetic field directions. The minim in the positive magnetic field data coincide with the maxima of the negative magnetic field data, as vis versa, as expected of Faraday rotation.

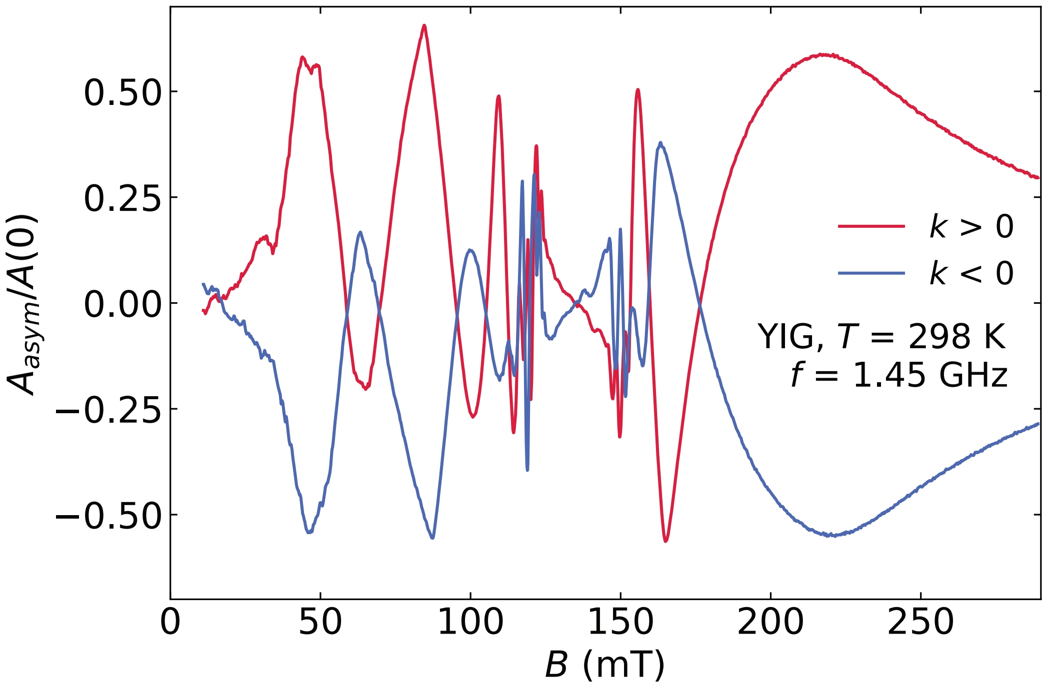

Figure 3.8: **Reversal of the propagation direction:** Tranmission mode experiments also allow us to reverse the propagation direction of the ultrasound by swapping the drive and receive transducers. Because the drive and receive transducer polarizations are misaligned by 45° with a fixed handedness, Faraday rotation flips the sign of the field antisymmetrized amplitude whe the propagation direction is reversed. Here, we plot the field antisymmetric signal as a function of applied magnetic field for the two propagation direction $\pm k$. As expected of a Faraday effect, the sign of the antisymmetric signal is opposite for the two propagation directions.

3.3 Kittel model

Here we give a brief derivation of the model proposed by Kittel as a way of generating RF magnons by injecting RF ultrasonic energy into a ferromagnet [30]. We begin with the classical Hamiltonian of a ferromagnetic spin system with magnetization density M along its easy axis, which we take here to be the z-axis. Energy can be added to the system by pointing the local magnetization density away from the z-axis. For that reason we take the system coordinates to be the components of the local magnetization density along the x- and y-axes, M_x and M_y. (Note about units: what follows is in SI units, but factors of μ_0 are omitted for clarity (but can be re-inserted by simply replacing the gyromagnetic ratio $\gamma \to \mu_0\gamma$). Otherwise, M is in units of tesla, and H in ampere per meter.)

There are two quantities associated with the magnetization dynamics: the spin stiffness A, which characterizes the energy cost of varying the magnetization density in space, and the precession frequency γM which quantifies the torque a perpendicular magnetization feels about the easy axis. To produce the equation of motion for Larmor precession, the Lagrangian is

$$L_{mag} = \frac{1}{2\gamma M}\left(M_x\dot{M}_y - \dot{M}_x M_y\right) - \frac{A}{2M^2}\left[(\nabla M_x)^2 + \left(\nabla M_y\right)^2\right]. \tag{3.1}$$

Applying a magnetic field strength H along the easy axis results in a Zeeman energy

$$E_Z = -H \cdot M \approx -H \cdot M\left(1 + \frac{M_x^2 + M_y^2}{2M^2}\right) \tag{3.2}$$

which, after dropping the constant term gives a term in the Lagrangian

$$L_Z = \frac{H}{2M}\left(M_x^2 + M_y^2\right). \tag{3.3}$$

Separately, we consider the elastic energy. Since we will be interested only in sound waves traveling along the magnetic easy axis, we have two elastic stiffnesses – one, c_L, for longitudinal displacement gradients (compressions along z) and another, c_T, for transverse displacement gradients (shearing perpendicular to z). In this case the coordinates are the local displacements, **u**, of the material from equilibrium and the Lagrangian is

$$L_{el} = \frac{\rho}{2}\dot{\mathbf{u}}^2 - \frac{c_L}{2}\varepsilon_{zz}^2 - \frac{c_T}{2}\left(\varepsilon_{xz}^2 + \varepsilon_{yz}^2\right), \tag{3.4}$$

where ρ is the mass density, $\varepsilon_{zz} = \partial_z u_z$ is the compressional strain, $\varepsilon_{xz} = (\partial_z u_x + \partial_z u_z)/2$ and $\varepsilon_{yz} = (\partial_z u_y + \partial_y u_z)/2$ are the shear strains.

The final ingredient of the model is a coupling between lattice strain and the magnetic moment. This can arise, for example, from the fact that exchange interactions depend on the relative positions of atoms in a material through the extent and geometry of orbital overlap in real space. The contribution of the spin-lattice coupling to the energy can be expanded in powers of the magnetization and strain. To lowest order in the magnetizations, we look for terms proportional to $M \cdot M_x$ and $M \cdot M_y$ and a single power of strain. In a cubic environment the only symmetry allowed term available that involves linear contributions from M_x and M_y is

$$L_i = \frac{g}{M^2}\left(M_x M_z \varepsilon_{xz} + M_y M_z \varepsilon_{yz} + M_x M_y \varepsilon_{xy}\right). \tag{3.5}$$

characterized by a single coupling constant g (in group theory jargon, explain in more depth later, this is the $T_{2g}^2 \times T_{1g}$ term that transforms as A_{1g}).

After the usual manipulations, the Lagrangian $L = L_{mag} + L_Z + L_{el} + L_i$ gives the coupled equations of motion for M_x, M_y, u_x, and u_y assuming an harmonic variation in the magnetization and strain

$$\begin{bmatrix} \frac{A}{M^2}k^2 + \frac{H}{M} & -\frac{i\omega}{\gamma M} & \frac{ig}{M}k & 0 \\ \frac{i\omega}{\gamma M} & \frac{A}{M^2}k^2 + \frac{H}{M} & 0 & \frac{ig}{M}k \\ -\frac{ig}{M}Mk & 0 & c_T k^2 - \rho\omega^2 & 0 \\ 0 & -\frac{ig}{M}k & 0 & c_T k^2 - \rho\omega^2 \end{bmatrix} \begin{bmatrix} M_{x0} \\ M_{y0} \\ u_{x0} \\ u_{y0} \end{bmatrix} = 0, \tag{3.6}$$

where M_{x0}, M_{y0}, u_{x0}, u_{y0} are the wave amplitudes for each degree of freedom, ω the frequency, and k the wavenumber. This set of linear equations can be block diagonalized by moving to a basis of left and right circularly polarized magnons and phonons: $m_\pm = M_x \pm iM_y$ and $u_\pm = u_x + iu_y$. In this basis the equation of motion is

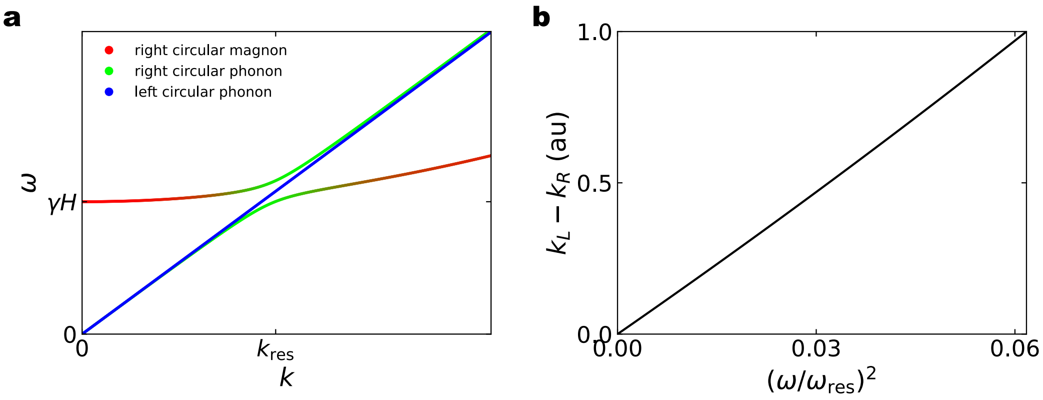

Figure 3.9: **Dispersion of the Kittel model:** (**a**) shows the numerical solution for the energy-momentum relationship of the three degrees of freedom in the Kittel model. The ingredients are two degenerate transverse phonons and a single right-hand circular polarized magnon. The solutions of the model are very well approximated by left- and right-hand circular polarized phonons and a right-hand circular polarized magnon. The color of each trace reflects the character of the mode at that energy. (**b**) shows that, when $\omega \ll \gamma H$, the difference in wavenumber of the two phonons – and therefore the Faraday rotation angle – increases as the frequency squared.

$$\begin{bmatrix} \frac{A}{M^2}k^2 + \frac{H}{M} - \frac{\omega}{\gamma M} & \frac{2ig}{M}k & 0 & 0 \\ -\frac{2ig}{M}k & c_T k^2 - \rho\omega^2 & 0 & 0 \\ 0 & 0 & \frac{A}{M^2}k^2 + \frac{H}{M} + \frac{\omega}{\gamma M} & \frac{2ig}{M}k \\ 0 & 0 & -\frac{2ig}{M}k & c_T k^2 - \rho\omega^2 \end{bmatrix} \begin{bmatrix} m_{+0} \\ u_{+0} \\ m_{-0} \\ u_{-0} \end{bmatrix} = 0. \tag{3.7}$$

The dispersion and mode decompositions can be carried out analytically, but is not terribly illuminating. The simple intuitive picture is much more useful: in the absence of magnetoelastic coupling ($g = 0$) Equation 3.3 describes an uncoupled system of magnons and phonons where the dispersion for the magnon is

$$\omega_{mag}(k) = \frac{\gamma A}{M}k^2 + \gamma H \tag{3.8}$$

and, despite seemingly having two branches here, one of the solutions has negative energy, so this single branch is non-degenerate. The dispersion of the phonon is

$$\omega_{ph}(k) = v_T k, \tag{3.9}$$

where $v_T = \sqrt{c_T/\rho}$ is the speed of sound. This, in contrast to the magnons, describes two degenerate transverse modes. Note that the magnon has a definite handedness (circular polarization), while the phonons can be written in whatever basis we choose.

The magnetoelastic coupling creates an avoided crossing near the point in energy/momentum where the coupled dispersions intersect. Since the u_- phonon doesn't intersect the M_- branch, to good approximation it retains linear dispersion. The opposite circularized phonon couples to the same circular polarized magnon and, near the intersection of the two dispersions, is mixed with the magnon. At this point – near the avoided crossing – the coupling alters the phonon's linear dispersion, breaking the degeneracy with the second transverse phonon and causing an acoustic Faraday effect.

To quickly review before attempting to be quantitative, the Faraday rotation comes from the simultaneous excitation of left and right circular polarized waves with different phase velocities. If the wavenumbers of the left/right circular waves are k_L/k_R then then sum of the two is

$$e^{ik_R x}\begin{pmatrix}1\\ i\end{pmatrix} + e^{ik_L x}\begin{pmatrix}1\\ -i\end{pmatrix} = \begin{pmatrix}e^{ik_R x} + e^{ik_L x}\\ i(e^{ik_R x} - e^{ik_L x})\end{pmatrix}. \tag{3.10}$$

written in terms of the average and difference of the wavenumbers $k_0 = (k_R + k_L)/2$ and $\delta k = (k_R - k_L)/2$ this becomes

$$2e^{ik_0 x}\begin{pmatrix}\cos(\delta k x)\\ \sin(\delta k x)\end{pmatrix}, \tag{3.11}$$

which describes a linear polarized wave with the polarization rotating as a function of position at a rate of

$$\frac{\Phi}{L} = \frac{k_R - k_L}{2} \tag{3.12}$$

radians per meter.

So to compute the Faraday rotation we take the disperion and find the difference in the two phonon wavevectors. This picture breaks down near the avoided crossing since there is no "phonon" any more, but when the phonon energy is far from the avoided crossing, the mixing is small and, as a start, we can treat the two modes which most closely satisfy $\omega = v_T k$. To treat the problem more precisely, we'll do numerics later.

To estimate the Faraday rotation far from the avoided crossing we solve for the dispersion at large magnetic field and small wavenumber, so $\omega \ll 2Ak^2 + \gamma H \approx \gamma H$. In this limit we can calculate the momenta near ω/v_T and expand in powers of $\omega/\gamma H$ to find the frequency as magnetic field dependence of the Faraday rotaion. The result, which will be related to the Hall viscosity later, is

$$\frac{\Phi}{L} \approx \frac{\sigma\omega^2}{4v} \frac{1}{(\gamma H - \sigma)^2 - \omega^2} \tag{3.13}$$

where $\sigma = 4g^2\gamma M^3/v^2\rho$. At sufficiently low frequency the rate of rotation is quadratic in frequency and decays like $1/H^2$ as the magnon is pushed to higher energy.

3.4 Fitting YIG to the Kittel model

It is tempting to simply fit the Faraday rotation data of YIG using Equation 3.3. However, before getting into the guts of it, we should point out a few subtleties. First, Equation 3.3 is a statement about *local* polarization. In particular, this means that if (as is the case in an experiment) that the total magnetic field inside a sample in non-uniform, than that must be taken into account in a fit. In fact, simulation of cylindrical geometries show that the field will strongest near the sample boundaries, so a disproportionate amount of the rotation will happen there. [82] In practice, we will make the assumption that there is an "average" magnetic field strength that captures the full rotation experienced over the entire sample.

Related to this fact is that the applied magnetic field (especially in the millitesla range) will not coincide with the total mangetic field relevant to the Faraday rotation. The magnetic field applied with our superconducting magnet will compete with the demagnetizing field of the sample as well as the anisotropy field due to higher order terms in the magnetic free energy. To account for this fact, we will replace H in Equation 3.3 with $H - H_{int}$, where H_{int} accounts for both the demagnetizing field and anisotropy field.

Lastly, Equation 3.3 describes the high-field behavior when both the sound and spin waves experience zero damping. Of course in a real sample, both types of excitation have finite lifetime, which can be accounted for by adding scattering rates to the magnon and phonon frequencies $\omega \to \omega + i/\tau$. This removes the singular behavior of Equation 3.3 at $\omega = (\gamma H - \sigma)$.

For the purposes of fitting data, it is useful to note that if the Faraday rotation angle Φ is regarded as a function of applied magnetic field and ultrasound frequency, then contours of constant rotation angle are straight lines. Rearranging Equation 3.3 we find

$$\frac{1}{\gamma}\left(1 + \frac{\sigma t}{4\Phi}\right)^{1/2} \omega = H - H_{int} \tag{3.14}$$

where $t = L/v$ is the sound wave transit time and H_{int} acccounts for the anistropy and demagnetization of the sample in the experiment. These straight contours are clearly visibly in the data as the streaks of amplitude minima in the f-B plane. Conceptually, then, fitting the data is clearcut: the value of H_{int} is determined by where the lines of amplitude minima meet at $f = 0$, γ sets the spacing between minima, and the combination of g^2, γ, and M set the overall slopes. Because M and g appear together, we are forced to use H_{int} as a proxy for M. The resulting value we obtain for g will be correct to an order of magnitude, but the error bar will be of order the demagnetizing factor (~50%).

To extract the physically meaningful quantities from the fit, we note two further details. First, for concreteness, the fit input is a set of amplitude minima at each frequency. The output is a set of lines with a common intercept at $f = 0$ and different slopes (one slope for each distinct minimum at fixed frequency). The slopes of the n-th minima, m_n, satisfies

$$m_n^2 = \frac{1}{\gamma^2}\left(1 + \frac{\sigma t}{4}\frac{2}{(2n+1)\pi}\right) \tag{3.15}$$

Echo	H_{int} (mT)	γ (GHz/T)	g (μeV/Å^3)
1	85	26.7	5
2	83	26.8	5

Table 3.2: **Summary of fit results:** summary of the physical parameters extracted from the Kittel model fits to the acoustic Faraday rotation data of YIG. The values obtained by fitting the amplitude minima of the first and second echoes agree very well with each other and the literature.

since the total rotation for a minimum is $(2n+1)\pi/2$ if the sound has rotated n times. On physical grounds, we expect the highest field minimum to be $n = 0$ (corresponding to a $\pi/2$ rotation), and the fit allows us to check this explicitly: the ratio of adjacent differences of the slope squared should follow a simple progression:

$$\frac{m_n^2 - m_{n+1}^2}{m_{n+1}^2 - m_{n+2}^2} = \frac{2n+5}{2n+1} \tag{3.16}$$

It's not Chern numbers, but we take what we get.

As a final note, Equation 3.3 is valid in the limit that $2AMk^2 \ll H$, so we will fit the high-field minima and go from there.

Figure 3.10 shows the fits of our data to the Kittel model of acoustic Faraday rotation. We perform independent fits to the amplitude versus magnetic field and frequency of the first two reflected echoes in the experiment. Both fits capture the linear-in-frequency dispersion of the amplitude minima very well. Using Equation 3.4 we identify the highest field minima in both echoes as the point at which the polarization has rotated $\pi/2$ radians. Fitting the slopes of each connected line of minima in the f-B plane to Equation 3.4 we extract the gyromagnetic ratio and magnetoelastic coupling of YIG. Table 3.2 summarizes the fit parameters – we find excellent agreement between our fit and other measurements of the gyromagnetic ratio, all of which find the g-factor of YIG to be that of free spins, $\gamma = 28$ GHz/T. The value of the magnetoelastic coupling also agrees with previous Faraday effect measurements.

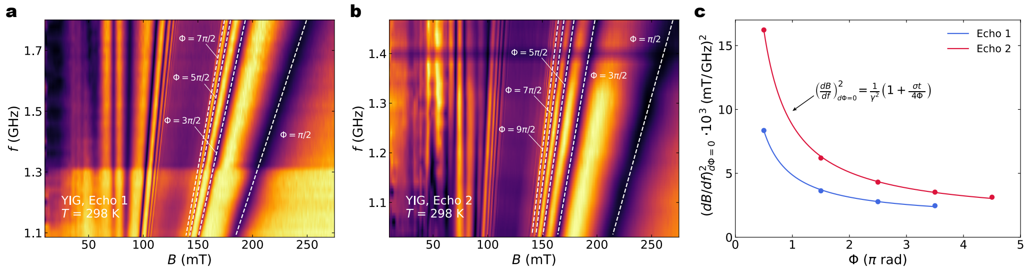

Figure 3.10: **Fits to the Kittel model:** (**a**) shows the Faraday rotation data (described in detail in Figure 3.4) for the first reflected echo overlaid with fits to the amplitude minima using the Kittel model. Linear fits to each connected set of minima in the f-B plane are constrained to meet at a single point at $f = 0$ which determines the demagnetizing field of the sample. The slopes of each line are then used to extract the gyromagnetic ratio and magnetoelastic coupling constant of YIG. (**b**) shows the same for the second reflected echo, which has traveled twice as far through the sample. (**c**) Each line of minima in the f-B plane is a contour of constant rotation angle $\Phi = (2n + 1)\pi/2$ with $n \geq 0$ an integer. As the rotation angle becomes large, the slope approaches the inverse of the gyromagnetic ratio. The rate at which the slope decrease as the rotation angle increases is set my the magnetoelastic coupling. The physical parameters extracted using the first and second echoes are in excellent agreement with each other and the literature.

3.5 Hall viscosity in the Kittel model

The Kittel model is a simple microscopic theory that describes ultrasound propagation in magnetic systems. In the model, magnetoelastic coupling causes transverse sound waves to experience acoustic Faraday rotation in an applied magnetic field. The modern literature takes a different perspective, in which the acoustic Faraday rotation results from the Hall viscosity of phonons. The connection between the two viewpoints is not immediately obvious, so this section bridges the two descriptions and details how the Hall viscosity emerges in the long-wavelength limit of the Kittel model.

To that end, we consider the Kittel model in the limit where the ultrasound frequency is much smaller than the gap in the spin wave spectrum induced by the applied magnetic field, so $\omega \ll \gamma H$. We will also make the simplifying assumption that the dispersion of the magnons is flat at the momenta we care about, which means we drop terms proportional to the gradients of the magnetization.

In this regime the magnetization dynamics are fast compared to the sound wave period, and we can integrate them out of the problem. The relevant terms of the Lagrangian can be written in terms of the magnetization components $\mathbf{M} = (M_x, M_y)$ and strain components $\varepsilon = (\varepsilon_{xz}, \varepsilon_{yz})$ as

$$L = \alpha \mathbf{M}^T \sigma \partial_t \mathbf{M} + \beta \mathbf{M}^T \mathbb{I} \mathbf{M} + \frac{g}{M} \mathbf{M}^T \mathbb{I} \varepsilon \tag{3.17}$$

where $\alpha = 1/2\gamma M$, $\beta = H/2M$, $\mathbb{I}$ is the identity matrix and $\sigma = i\sigma_y$ is the symplectic matrix (antisymmetric with ones on the off-diagonals, in normal speak).

The equation of motion for the magnetization is

$$[\beta \mathbb{I} + \alpha \sigma \partial_t] \mathbf{M} = -\frac{g}{2} \varepsilon, \tag{3.18}$$

from which we can expand the magnetization dynamics in powers of the time derivative. To first order in ∂_t the result is

$$\mathbf{M} \approx \left(-\frac{g}{2\beta} \mathbb{I} + \frac{g\alpha}{2\beta^2} \sigma \partial_t \right) \varepsilon. \tag{3.19}$$

Inserting Equation 3.5 in the Lagrangian, Equation 3.5, we took for terms that are first order in the time derivative. These come from the first and third terms of Equation 3.5, yielding an antisymmetric portion of the Lagrangian

$$L_{asym} = -\frac{g^2 \alpha}{2\beta^2} \varepsilon^T \sigma \partial_t \varepsilon = -\frac{g^2 \alpha}{2\beta^2} \left(\varepsilon_{xz} \dot{\varepsilon}_{yz} - \dot{\varepsilon}_{xz} \varepsilon_{yz} \right), \tag{3.20}$$

which is exactly the form of a Hall viscosity tensor element. Restoring units, we find the effective Hall viscosity

$$\eta_H = \frac{g^2}{\gamma M}\frac{1}{\mu_0 H^2}. \tag{3.21}$$

The acoustic Faraday rotation that results from this viscosity is found by inserting Equation 3.5 into the wave equation for propagating transverse waves at frequency ω and wave vector k

$$\rho\omega^2\mathbf{u} = k^2\begin{bmatrix} c_T & i\eta_H\omega \\ -i\eta_H\omega & c_T \end{bmatrix}\mathbf{u} \tag{3.22}$$

where c_T is the shear modulus and $\mathbf{u}$ is the polarization vector. Solving for the wave vectors we get $k_\pm = \rho\omega^2/(c_T + \eta_H\omega)$ and for $\eta_H\omega \ll c_T$ the difference in wave vectors (and the Faraday rotation per unit length) is

$$\frac{\Phi}{L} = \frac{k_+ - k_-}{2} \approx \frac{\eta_H}{2\rho v^3}\omega^2 \tag{3.23}$$

which matches exactly with the high magnetic field, low frequency limit of the Kittel model derived earlier. This expression is also directly analogous to the Faraday rotation derived starting from a long-wavelength Hall viscosity in Balents.

Putting in the numbers from our ultrasound measurements of YIG into Equation 3.5 we find, at an applied field of 250mT

$$\eta_H(250\text{ mT}) = 5\text{ mPa}\cdot\text{s}, \tag{3.24}$$

roughly the viscosity of room temperature water (or, more closely, of liquid gold).

3.6 Thermal Hall effect of YIG

In addition to an acoustic Faraday effect, the Hall viscosity of phonons is predicted to result in a thermal Hall effect. Though the acoustic Faraday effect in YIG is well-characterized, there have been no measurements of its thermal Hall conductivity. Therefore, to establish a quantitative link between the acoustic Faraday rotation and the thermal Hall effect of YIG, we perform measurements of its thermal Hall conductivity. We find no detectable thermal Hall effect within our experimental resolution. Given the magnetoelastic coupling we measure via the acoustic Faraday rotation, a simplified calculation of the thermal Hall conductivity of YIG suggests that the thermal Hall angle is several orders of magnitude of the current experimental resolution. This null result, however, is significant in the context of thermal transport measurements in other magnetic insulators, where the thermal Hall effect appears almost universal. The absence of a thermal Hall effect in YIG may stem from its exceptionally high crystal quality and low scattering rate.

To measure the themal Hall conductivity of YIG, we polish a thin Hall bar from our [111] oriented cylinder. The dimensions of the Hall bar are 1.22 mm × 1.50 mm × 25 μm where the large lateral dimensions define a face perpendicular to the [111] direction of the crystal. Mangetic field is applied along the [111] direction and the heat current perpendicular to the magnetic field. Because of the cubic symmetry of YIG, the longitudinal the transverse thermal conductivities are isotropic and the precise orientation of the heat current (and magnetic field) should not impact the results dramatically. All measurements were done using the DC steady state method, stepping the temperature at fixed magnetic field (described in more detail in methods).

The temperature dependence of the longitudinal thermal conductivity, κ_{xx}, at several values of applied magnetic field is shown in Figure 3.11a. The thermal conductivity rises from low temperature and exhibits a peak of approximately 250 W/K·m at $T \approx 22$ K in zero applied field. As the applied magnetic field increases, the thermal conductivity is suppressed by ~10% at 18 T. The reduction in the thermal conductivity on application of an external magnetic field is consistent with previous studies.

The simple low-energy magnon spectrum YIG offers a natural explanation for its negative magnetothermal conductivity. Because of their low damping, a significant fraction of the thermal conductivity of YIG is due to magnons and, below 200 K, the thermal population of magnons is restricted to the lowest energy acoustic branch at the gamma point (see Figure 3.2b). With a g-factor of 2, application of a magnetic field induces a gap in the acoustic magnons of 1.34 K/T, reducing the number of thermally populated states at a given temperature. At sufficiently low temperature compared to the applied magnetic field, the thermal conductivity due to magnons should be completely suppressed, and the remaining thermal conductivity due mostly to phonons.

The results of the thermal Hall conductivity measurements are presented in Figure 3.12. A non-zero thermal Hall conductivity generates a

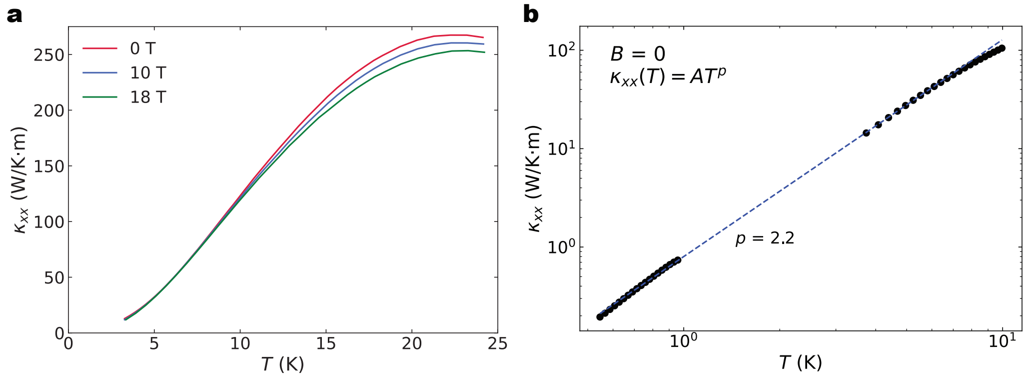

Figure 3.11: **Longitudinal thermal conductivity of YIG:** Measurement of the temperature and magnetic field dependence of the longitudinal thermal conductivity, κ_{xx}, of YIG. (**a**) Application of an external magnetic field results in a gap in the magnon spectrum. The reduction of low energy heat carriers causes the negative magnetothermal conductivity. Note, also, that the scale of the longitudinal thermal conductivity makes measurement of the thermal Hall effect challenging – large κ_{xx} means that it is difficult to generate sizeable temperature gradient across the sample. (**b**) The low temperature thermal conductivity at zero applied magnetic field approximately follows a power law with exponent $p = 2.2$. Without attempting to over-fit the data to a sum of two power laws, we note that this exponent falls squarely between the T^3 behavior expected of phonons and the $T^{3/2}$ expected for quadratic magnons.

transverse temperature difference, ΔT_y, across the sample that is antisymmetric in applied magnetic field. We observe no transverse temperature difference at an applied magnetic field of 2 T, 2.4 T, or 14 T between 3 K and 15 K. Converted into a thermal Hall conductivity, κ_{xy}, we bound the value $\kappa_{xy} < 1$ mW/K·m below 10 K.

It is possible that the thermal Hall conductivity of YIG is non-zero but below our measurement sensitivity. The experimental noise floor of ~ 100 μK is set primarily by the sensitivity and calibration of the thermometry. Our measurements at above 1 K would therefore benefit from using

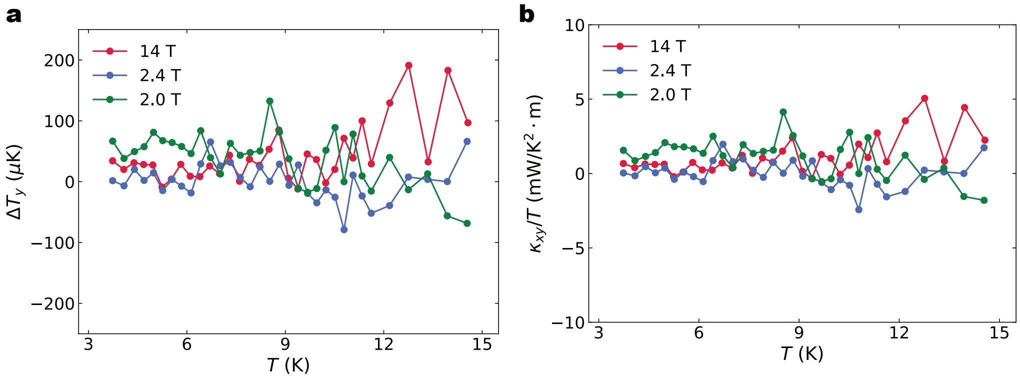

Figure 3.12: **Thermal Hall conductivity of YIG:** The Hall viscosity that results in the acoustic Faraday rotation of YIG also generates a thermal Hall effect. We measure the thermal Hall conductivity by detecting the odd in magnetic field transverse temperature difference, ΔT_y, across the sample. (**a**) shows the measured transverse temperature drop, antisymmetrized in magnetic field, between 3 K and 15 K at three different values of applied magnetic fields. We observe no signature of a thermal Hall effect within the resolution of our thermometers. (**b**) shows the temperature gradient from **a** converted to a thermal Hall conductivity divided by temperature. The experiment suggests that the thermal Hall conductivity $\kappa_{xy} < 1$ mW/K·m. Our measurement suggests that the thermal Hall conductivity of YIG is below current experimental resolution.

more sensitive Cernox 1050 thermometers, for example. In addition to increasing our temperature sensitivity, a better upper bound on κ_{xy} would be obtained by generating a larger longitudinal thermal gradient across the sample. In this respect YIG is a difficult material to work with because its longitudinal thermal conductivity is high enough that at experimentally accessible levels of applied heat current, the resulting thermal gradients are still small. For example, the longitudinal thermal conductivity of La_2CuO_4, which exhibits a large thermal Hall effect, has more than ten times less longitudinal thermal conductivity than YIG.

Figure 3.13 compares the thermal Hall angle $|\kappa_{xy}/\kappa_{xx}|$ of YIG to a vari-

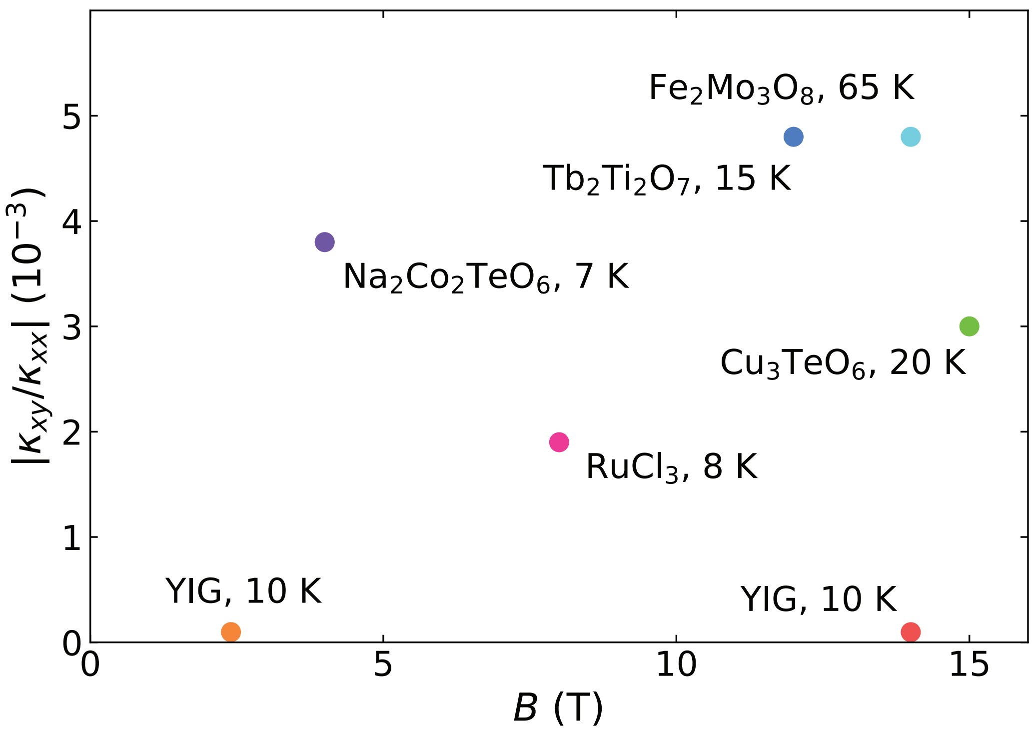

Figure 3.13: **Comparison of the thermal Hall angle in magnetic oxides:** A thermal Hall effect has been detected in a wide range of magnetic insulators. Here, we compare the maximum value of the the thermal Hall angle κ_{xy}/κ_{xx} in four other magnetic oxides, as well as α-$RuCl_3$. Our measurement of κ_{xy} of YIG places the thermal Hall angle nearly an order of magnitude below other insulating oxides. This may be because of the exceptionally high quality of YIG samples, with low disorder suppressing extrinsic contributions to the thermal Hall effect. The null result, however, is consistent with estimates of the intrinsic thermal Hall conductivity due to the phonon Hall viscosity of YIG, which suggest the intrinsic contribution is orders of magnitude below the experimental resolution.

ety of other insulating magnetic oxides with $\kappa_{xy} \neq 0$. The thermal Hall angle of YIG lies an order of magnitude below other materials at similar temperatures and applied magnetic fields. We include our measurements performed at both large and small applied magnetic field, where the gap in the spin wave spectrum is large and small compared to the temperature range of the measurement. An extrinsic thermal Hall effect due, for instance, to scattering off magnetic impurities, would naively increase linearly with applied magnetic field. An intrinsic thermal Hall effect due to hybridization of phonons with magnons, however, would only be expected if the thermal population of phonons extends past the spin wave gap. We find no evidence of a thermal Hall effect in either of these regimes. Estimates of the intrinsic contribution to the thermal Hall conductivity, presented below, are consistent with our measurement. The lack of a high-field thermal Hall effect may be due to the comparably high-quality of YIG crystals, where growth has been refined over decades, compared to other magnetic oxides.

3.7 Viscosity to phonon Berry curvature

In the modern literature, phonon Hall viscosity is related to thermal Hall conductivity through the Berry curvature of phonons. The concept of phonon Berry curvature, however, is a little ambiguous – what, exactly, is the Berry curvature we are referring to in this context? In this section we detail how, in the quantized version of models like Kittel's, spin-lattice coupling results in Berry curvature on the phonon bands. This phonon Berry curvature is exactly analogous to the Berry curvature of Bloch electrons.

We showed previously how, in the long wavelength limit, models with coupled magnetic and lattice degrees of freedom like the Kittel model give rise to phonon Hall viscosity. In that limit the phonon Lagrangian can be written in terms of the atomic displacements u as

$$L = \frac{\rho}{2}\dot{u}^2 - u^T \hat{C} u - \dot{u}^T \hat{\eta} u, \tag{3.25}$$

where $\hat{C}$ is the stiffness matrix (elastic moduli) and $\hat{\eta}$ is the time-odd antisymmetric viscosity. If we take for granted that we can make a "quantum" theory of the same model by promoting u to a field operator, the

Hamiltonian takes the generic form

$$H = \sum_k H_k = \frac{1}{2}\sum_k \frac{(p_k - \hat{\eta}(k)u_k)^2}{2\rho} + u_k^\dagger \hat{C} u_k, \tag{3.26}$$

where the viscosity plays the role of a vector potential in electromagnetism.

To compute the Berry curvature we need wavefunctions. To that end, we find the phonon creation operators $a = u + ip$ which diagonalize the Hamiltonian. The requires change of basis on the operators u and p that both diagonalizes H and preserves the commutation relations of the momentum and position operators. We can encode the full set of commutation relation between all three components of the position and momentum operators by writing $z_k = (u_k, p_k)$, so the commutation relations to preserve are

$$[z_k, z_k^\dagger] = i\begin{bmatrix} 0 & \mathbb{I} \\ -\mathbb{I} & 0 \end{bmatrix} \equiv iJ. \tag{3.27}$$

where $\mathbb{I}$ is the 3×3 identity matrix. The constraint on the change of basis, S, then, is that the redefined operators $z' = (u', p')$ satisfy

$$[z', z'^\dagger] = S\,[z_k, z_k^\dagger]S^\dagger = S\,(iJ)S^\dagger = iJ. \tag{3.28}$$

In jargon, we want S unitary symplectic. The existence of such an S that diagonalizes H is guaranteed by Williamson's theorem. For the uninitiated, these particulars are not obviously necessary because, in the case of "normal" phonons without viscosity, the block diagonal form of H can be diagonalized by a block diagonal unitary matrix, imitating the solution of a standard, second quantized system.

We can find the correct change of basis by solving the equation of motion

$$\dot{z}_k = i\,[z_k, H_k]\,. \tag{3.29}$$

For the Hamiltonian of viscous phonons, the equation of motion takes the form

$$\omega_k z_k = iJH_k z_k = i\begin{bmatrix} -\hat{\eta}/\rho & \mathbb{I}/\rho \\ -\hat{M} & -\hat{\eta}/\rho \end{bmatrix} z_k \tag{3.30}$$

The complication is that the matrix we want to diagonalize is not Hermitian, which brings in some subtleties. First, care must be taken with normalization. Using the usual $\psi_i^\dagger \psi_j = \delta_{ij}$ causes some problems since, for an eigenstate with energy ω_i, we would have $\psi_i^\dagger iJH\psi_i = \omega_i\delta_{ij}$. But since the left side is not Hermitian, there is no guarantee that $\omega_i > 0$ and this normalization is not possible in general.

To fix this, consider multiplying the eigenvalue problem on the left by $\psi_i^\dagger iJ$. Using $J^2 = -\mathbb{I}$, we find

$$\psi_i^\dagger H\psi_i = \omega_i \psi_i^\dagger iJ\psi_i. \tag{3.31}$$

Since H is Hermitian and positive definite (because the phonon problem is supposed to be stable), Equation 3.7 provides a consistent normalization as long as $\psi_i^\dagger iJ\psi_i$ has the same sign as ω_i, and we can adopt

$$\psi_i^\dagger iJ\psi_j = \delta_{ij}\mathrm{sign}(\omega_\mathrm{i}). \tag{3.32}$$

In passing, mention that this normalization is very annoying to remember when doing perturbation theory – corrections to the state vectors of the form $\psi_j^\dagger (iJ)V\psi_i/(\omega_i - \omega_j)$ carry the factor of $\mathrm{sign}(\omega_\mathrm{j})$.

Note that since H and iJ are both Hermitian, ω_i is real. In addition, taking the conjugate of the equation of motion shows that if ψ_i has energy ω_i, then ψ_i^* has energy $-\omega_i$. So the energies come in $\pm\omega_i$ pairs. Taken together, this means the matrix of eigenvectors V satisfies the following

$$iJHM = V\Omega\sigma_z \qquad V^\dagger iJV = \sigma_z, \tag{3.33}$$

where Ω is a block diagonal matrix with two copies of the phonon energies on the diagonal, and σ_z is the Pauli matrix. A little bit of arithmetic shows that this allows us to diagonalize the Hamiltonian and while maintaining the proper commutation relation using the change of basis $S = MT$ where

$$T = \frac{1}{\sqrt{2}}\begin{bmatrix} 1 & i \\ 1 & -i \end{bmatrix}. \tag{3.34}$$

Finally, we see that the phonon creation and annihilation operators, $\hat{a} = (a, a^\dagger)$, for viscous phonons are proportional to the eigenstates of the equation of motion. Using the usual definition with $a = u + ip$, so that $\hat{a} = T \cdot (u, p) = Tz$

$$H = \frac{1}{2}\sum_k z^\dagger H_k z = \frac{1}{2}\sum_k (VTz)^\dagger \begin{bmatrix} \Omega_k & 0 \\ 0 & \Omega_k \end{bmatrix} (VTz) = \frac{1}{2}\sum_k (V\hat{a})^\dagger \begin{bmatrix} \Omega_k & 0 \\ 0 & \Omega_k \end{bmatrix} (V\hat{a}). \tag{3.35}$$

This, finally, motivates the definition of the phonon Berry curvature $\mathbf{\Omega}$ associated with the phonon band with energy $\omega_i(k)$ presented, for example, in Shi in terms of the eigenstates of the equation of motion

$$\mathbf{\Omega} = -\mathrm{Im}\left[\frac{\partial(\psi_\mathrm{i}^\dagger \mathrm{iJ})}{\partial \mathbf{k}} \times \frac{\partial \psi_\mathrm{i}}{\partial \mathbf{k}}\right], \tag{3.36}$$

exactly the same idea as for the Berry curvature of an electron band. This Berry curvature, defined on the phonon bands in momentum space, is distinct from *strain* Berry curvature, in which lattice strain is a tuning parameter for the full electronic Hamiltonian of a material. This second definition of Berry curvature, in fact, provides a more direct link to the phonon Hall viscosity as detailed in later sections.

3.8 Thermal Hall conductivity – comparison with a simple model

To model the low-energy dynamics of a material like YIG, we should put the cubic stiffness matrix and the experimentally measured viscosities into Equation 3.7. This is possible numerically, however, to obtain a reasonable approximation, we will follow Balents and work with a simpler, isotropic model that admits an analytic, perturbative solution in $\hat{\eta}$. Because symmetry dictates that the Hall viscosity of an isotropic system is zero an isotropic model is not correct, but it's a start.

For an isotropic medium, there are two degenerate transverse modes and a single longitudinal mode irrespective of the phonon wave vector, $\mathbf{q}$. The stiffness matrix is

$$\hat{C} = \hat{R}(\mathbf{q}) \begin{bmatrix} c_T q^2 & 0 & 0 \\ 0 & c_T q^2 & 0 \\ 0 & 0 & c_L q^2 \end{bmatrix} \hat{R}(\mathbf{q})^T, \tag{3.37}$$

where c_L and c_T are the transverse and longitudinal elastic moduli, and $\hat{R}(\mathbf{q})$ is the rotation matrix that takes the z-axis to $\mathbf{q}$. The eigenvectors of the unperturbed problem are those of

$$iJH_0 = i\begin{bmatrix} 0 & \mathbb{I}/\rho \\ \hat{C} & 0 \end{bmatrix}, \tag{3.38}$$

which have energies $\pm v_T$ and $\pm v_L$. The corrections due to the viscosity are found using degenerate perturbation theory on the block diagonal

$$iJH_1 = i\begin{bmatrix} -\hat{\eta}/\rho & 0 \\ 0 & \hat{\eta}/\rho \end{bmatrix}. \tag{3.39}$$

At this point we need an expression for $\hat{\eta}(k)$. Because the thermal Hall conductivity will involve states up to energy $k_B T$, much larger than the phonon energies we probe with ultrasound in an acoustic Faraday effect measurement, we must modify the long-wavelength viscosity in the Kittel model presented earlier. We find the momentum dependence of the Hall viscosity in the Kittel model by keeping the gradient terms in the magnetization (which we threw away previously).

Using the Kittel model assumption that the magnetization dynamics are completely isotropic and that the direction of the magnetization is along the applied magnetic field, we can find the momentum-dependent viscosity when the field is applied along the z-axis. This amounts to changing β in Equation 3.5 to $\beta + Ak^2/2M^2$. We can write the viscosity in terms of the gap in the magnon spectrum in units of momentum, $\Delta = \sqrt{HM/A}$ as

$$\eta_H(k) = \frac{g^2 M}{\mu_0 \gamma A^2}\frac{1}{(\Delta^2+k^2)^2} \equiv \frac{\tilde{\eta}}{(\Delta^2+k^2)^2}. \tag{3.40}$$

After carrying out the perturbation theory we find the z component of the Berry curvature of the longitudinal branch and of each of the transverse bands, $\Omega_{z,L}$ and $\Omega_{z,T}$, to linear order in $\tilde{\eta}$

$$\begin{aligned} \Omega_{z,L} &= \tilde{\eta}\frac{3v_L^2+v_T^2}{\rho v_L(v_L^2-v_T^2)}\frac{\cos^2(\theta)[-3k^2+\Delta^2+(7k^2+3\Delta^2)\cos(2\theta)]}{k(k^2+\Delta^2)^2} \\ \Omega_{z,T} &= -\tilde{\eta}\frac{v_L^2+3v_T^2}{\rho v_T(v_L^2-v_T^2)}\frac{\cos^2(\theta)[-3k^2+\Delta^2+(7k^2+3\Delta^2)\cos(2\theta)]}{k(k^2+\Delta^2)^2}, \end{aligned} \tag{3.41}$$

where θ is the angle between $\mathbf{k}$ and the z-axis, and $v_L = \sqrt{c_{11}/\rho}$ and $v_T = \sqrt{c_{44}/\rho}$ are the longitudinal and transverse sound velocities keeping in mind that we are ignoring the cubic anisotropy of the lattice, so there are only two speeds of sound. Note that the sign of the Berry curvature on the longitudinal and transverse branches has opposite sign, and there will be competition between the two.

To estimate the thermal Hall conductivity from the Berry curvature, we employ the result presented in Shi et al which

$$\frac{\kappa_{xy}}{T} = \frac{1}{\hbar T^2} \int dE E^2 \sigma(E) \frac{dn_{BE}}{dE} = \frac{k_B^2}{\hbar} \int dx \frac{x^2 e^x}{(e^x - 1)^2} \sigma(k_B T x), \tag{3.42}$$

where $\sigma(E)$ counts the Berry curvature contribution from states with energy less than E from each phonon band i

$$\sigma(E) = \sum_i \int \frac{d^3 q}{(2\pi)^3} \Omega_{z,i} \Theta(E - E(q)). \tag{3.43}$$

For the Berry curvature in the Kittel model, Equation 3.8, the integral $\sigma(E)$ ends up being simple to evaluate. Up to coefficients that are functions of the phonon velocities and the material density, the result is a function of the energy $\hbar v_s \Delta$ where v_s is the speed of sound on that branch

$$\sigma(E) = \frac{4E^2}{15(1 + E^2)^2}, \tag{3.44}$$

from which we can see that the thermal Hall conductivity $\kappa_{xy}/T \sim T^2$ at low temperature, in agreement with the results in Shi and Balents.

The thermal Hall conductivity, Equation 3.8 can be evaluated numerically using the measured material parameters of YIG. The result is valid in the limit where the temperature is small compared to the magnon gap of YIG. Since the g-factor of YIG is almost exactly 2, this restricts the range of validity of the model at an applied magnetic field of 2 T to $T \ll 2$ K. At an applied magnetic field of 2 T, we find the maximum value of the intrinsic thermal Hall conductivity (within the realm of validity of this model) is on the order of 10 nW/K·m – four orders of magnitude below our measurement's sensitivity. Though somewhat discouraging, this is certainly consistent with the null result of the experiment.

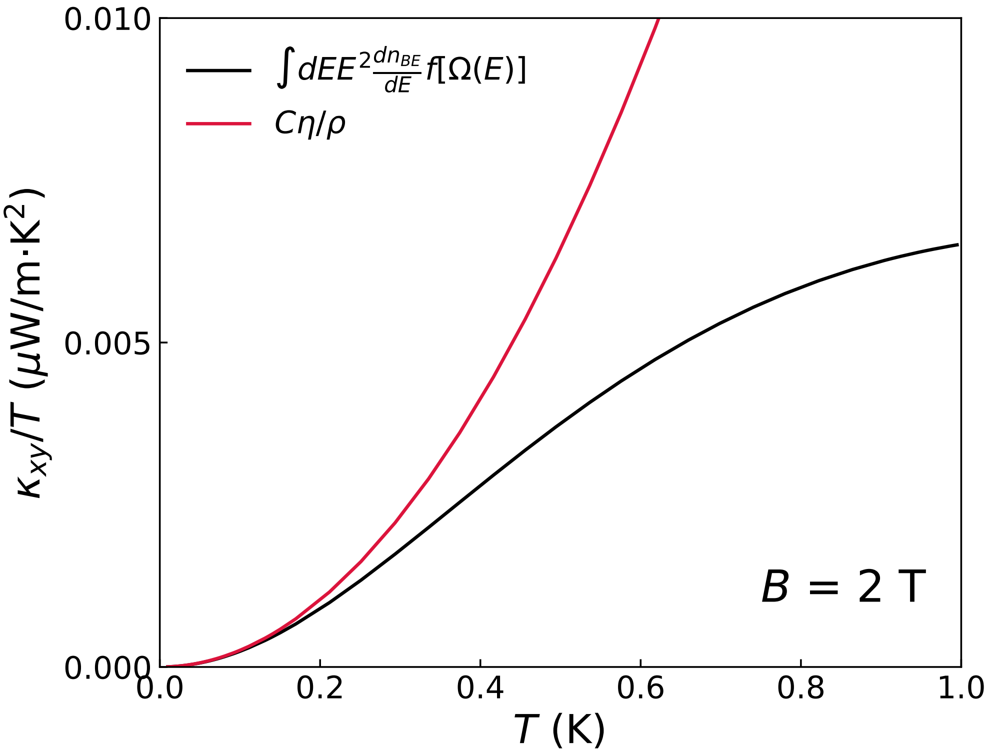

Figure 3.14: **Calculating the thermal Hall conductivity of YIG:** Plot of the temperature dependence of the intrinsic thermal Hall conductivity of YIG due to phonon Hall viscosity, η_H. The black curve is the Hall conductivity calculated using the Berry curvature formalism presented in Shi et al. The red curve is an estimate based on the acoustic energy flux, where the Hall conductivity is proportional to the specific heat, C, as presented in section 4.4. Using the Hall viscosity determined by the acoustic Faraday rotation measurement, both estimates predict a magnitude of κ_{xy} on the order of 10nW/K·m in an applied magnetic field of 2 T. The calculation is in agreement with the null result of the experiment.

3.9 Wrapping up and Next steps

In this section, we measured the acoustic Faraday rotation of YIG, establishing a set of experiments to isolate the time-odd, phonon Hall viscosity. The Faraday rotation is detected by measuring acoustic power transmitted between two shear-polarized piezoelectric transducers with polarizations misaligned by forty-five degrees. Misaligning the transducer polarization allows us to distinguish clockwise from counterclockwise polarization rotation, and the Hall viscosity appears as an antisymmetric in field component in the amplitude.

In YIG, the relatively large magnitude of the magnetoelastic coupling combined with the availability of large, high-quality crystals makes the Faraday rotation especially straightforward to measure. Interpreting our Faraday rotation data using the model of coupled magnetic and lattice degrees of freedom due to Kittel, we determined the Hall viscosity of YIG to be $\eta_H = 5$ mPa·s in an applied magnetic field of 250mT. Independent of the microscopic mechanism underlying the Faraday rotation, the transmission experiment we validated in YIG will enable us to extend measurements of the Hall viscosity to other materials in which the viscosity is smaller or the material only grows in thin flakes.

Because phonon Hall viscosity is also predicted to result in an intrinsic thermal Hall effect, we measured the thermal Hall conductivity of YIG, finding no thermal Hall effect within experimental resolution. We put a bound on the thermal Hall angle of YIG, $\kappa_{xy}/\kappa_{xx} < 10^{-4}$. This contrasts with other insulating magnetic oxides, where Hall angles greater than 10^{-3} have been reported. The lack of a thermal Hall effect may reflect the intrinsically low scattering rate of high-purity YIG.

The absence of a thermal Hall effect in YIG, however, is consistent with calculations of κ_{xy} due to the Berry curvature of phonons. Given the Hall viscosity we measure in the Faraday rotation experiment, we estimate an intrinsic thermal Hall effect of approximately 10 nW/K·m, well below our experimental resolution. Though this does not bode well for making a quantitative, experimental link between phonon Hall viscosity and thermal Hall conductivity in YIG, there are other avenues for further experiments.

The magnetostriction of the related compound, $Dy_3Fe_5O_{12}$, is known to be nearly two orders of magnitude larger than that of YIG. [94] Naively, because the thermal Hall conductivity is proportional to the square of the magnetoelastic coupling, this should bring the thermal Hall conductivity above the experimental noise floor. However, the magnon spectrum of stoichiometric $Dy_3Fe_5O_{12}$ no longer supports low-energy excitations that would couple strongly to gigahertz frequency ultrasound – what you gain in κ_{xy} you lose in Faraday rotation. [95, 96] Dy-doped YIG may provide a middle ground in which both the magnetoelastic coupling is amplified and the Faraday effect remains large. [97]

Chapter 4

Phonon Hall viscosity and the Intrinsic thermal Hall effect of α-RuCl$_3$

This chapter appears as a paper of the same title, authored by me, Ezekiel Horsley, Subin Kim, Young-June Kim, and B.J. Ramshaw. [98]

The thermal Hall effect has been observed in a wide variety of magnetic insulators, yet its origin remains controversial. While some studies attribute it to intrinsic origins—such as heat carriers with Berry curvature—others propose extrinsic origins—such as heat carriers scattering off crystal defects. Even the nature of the heat carriers is unknown: magnons, phonons, and fractionalized spin excitations have all been proposed. These questions are significant for the study of quantum spin liquids and are particularly relevant for α-RuCl$_3$, where a quantized thermal Hall effect has been attributed to Majorana edge modes. Here, we use ultrasonic measurements of the acoustic Faraday effect to demonstrate that the phonons in α-RuCl$_3$ have Hall viscosity—a non-dissipative viscosity that rotates phonon polarizations and deflects phonon heat currents. We show that phonon Hall viscosity produces an intrinsic thermal Hall effect that quantitatively accounts for a significant fraction of the measured thermal Hall effect in α-RuCl$_3$. More broadly, we demonstrate that the acoustic Faraday effect is a powerful tool for detecting phonon Hall viscosity and the associated phonon Berry curvature, offering a new way to uncover and study exotic states of matter that elude conventional experiments.

4.1 Introduction

Thermal transport has emerged as the dominant technique in the search for exotic, charge-neutral quasiparticles [99, 100]. The observation of a thermal Hall effect—where a temperature gradient builds up perpendicular to both a magnetic field and a heat current—has been used as evidence for fractionalized spin excitations in quantum magnets such as $Tb_2Ti_2O_7$ [101], α-RuCl$_3$ [102, 103], and several Kagome antiferromagnets [104, 105, 106]. Central to these claims is the assumption that phonons do not themselves generate a thermal Hall effect. This is a reasonable assumption, as phonons carry neither electric charge nor spin and thus should not interact directly with magnetic fields.

This assumption has recently been called into question due to the discovery of relatively large thermal Hall effects in conventional antiferromagnets that are unlikely to host spinons [107, 108, 109], as well as in non-magnetic insulators where phonons are the only heat carrier [110, 111, 112]. This suggests that phonons may be responsible for the thermal Hall effect in at least a subset of these materials.

How can phonons generate a thermal Hall effect? Intrinsic mechanisms invoke phonon Berry curvature [113, 114, 115, 116], whereas extrinsic mechanisms invoke phonon skew scattering [117, 118, 119]. While a large number of theoretical proposals have been put forward [113, 114, 115, 116, 117, 118, 119, 120, 121, 122], the only experimental probe thus far has been thermal transport—applying heat currents and measuring the resultant temperature gradients. A key limitation of thermal transport is its inability to distinguish between intrinsic and extrinsic mechanisms, and this has made it difficult to distinguish between proposed origins at even a coarse level.

Here, we take advantage of the fact that phonon Berry curvature not only causes an intrinsic thermal Hall effect, but also generates a dissipationless viscous force known as phonon Hall viscosity [123, 124]. Phonon Hall viscosity rotates the polarization of transverse-polarized phonons as they propagate (see Figure 4.1). This is called the acoustic Faraday effect and is analogous to how the optical Faraday effect rotates the polarization of light. Where thermal transport measurements use phase-incoherent heat currents, acoustic Faraday measurements use phase-coherent phonons that are only sensitive to intrinsic effects and not to phase-incoherent scattering.

We measure the acoustic Faraday effect in α-RuCl$_3$ and extract the phonon Hall viscosity. We find that the Hall viscosity is peaked near the magnetic phase boundary where the thermal Hall effect is maximized. The existence of phonon Hall viscosity in α-RuCl$_3$ suggests a non-zero phonon contribution to the thermal Hall effect, challenging interpretations of the thermal Hall effect solely in terms of Majorana fermions [125, 102, 126] or other fractionalized spin excitations [103]. We suggest that phonons acquire Hall viscosity in α-RuCl$_3$ by coupling to spin excitations. This general mechanism is likely responsible for the unusual thermal Hall effects reported in many other magnetic insulators.

4.2 Results

4.2.1 Measuring the acoustic Faraday effect

We first describe how phonon Hall viscosity alters sound propagation in solids, giving rise to the acoustic Faraday effect. In general, three dimensional solids have three distinct speeds of sound for waves propagating along any given direction. In crystals with high enough symmetry, and for high-symmetry propagation directions, the two transverse modes—modes with their polarization vector of atomic displacement perpendicular to their propagation vector—become degenerate, with the same speed of sound. This is the case for sound propagating along the c axis of α-RuCl$_3$. The degeneracy between the two modes is lifted by Hall viscosity, which can arise, for example, through spin-lattice coupling. As a result, the left- and right-circularly polarized combinations of the transverse modes then propagate at different speeds, giving rise to an acoustic Faraday effect (see Figure 4.1). This phenomenon is well documented in materials like yttrium iron garnet (YIG) and Cr$_2$O$_3$, where it arises from hybridzation between acoustic phonons and magnons [127, 128, 129]; in Tb$_3$Ga$_5$O$_{12}$, where it arises from coupling between acoustic and optical phonons [130] and which also has a phonon thermal Hall effect [131]; in CeAl$_2$ and Ni-doped MgO, where it arises from crystal field splitting [132, 133]; and in superfluid ^{3}He-B, where it emerges due to the shear stiffness of the Fermi liquid [134].

The acoustic Faraday effect is measured by generating linearly polarized, transverse sound waves using shear-polarized piezoelectric trans-

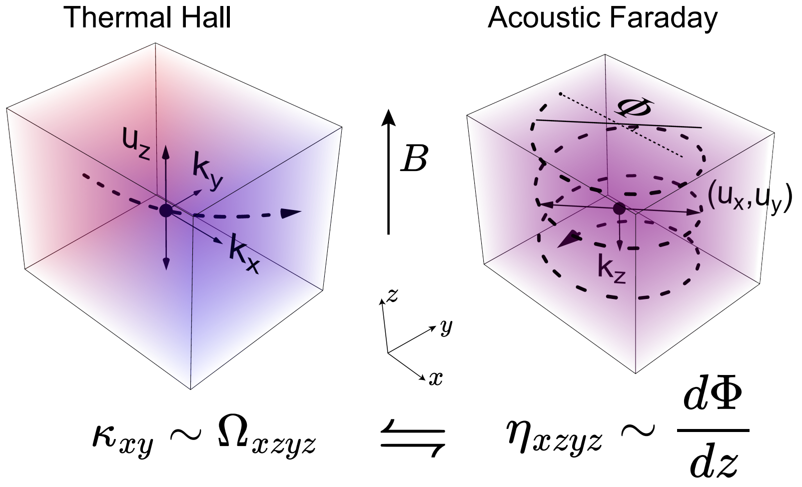

Figure 4.1: **The thermal Hall and acoustic Faraday effects, and how they are related.** Applying a magnetic field B parallel to z breaks time reversal symmetry and allows for both phonon Berry curvature, Ω_{xzyz}, and phonon Hall viscosity, η_{xzyz}. Phonon Hall viscosity can be thought of as a long-wavelength manifestation of the microscopic Berry curvature—the double-headed arrow indicates that these two quantities are equivalent [123, 124]. On application of a temperature gradient along x (indicated by the red-blue color gradient), phonon Berry curvature deflects phonons carrying heat along x and generates a heat current along y (the dashed line indicates the trajectory of a phonon in the presence of Berry curvature). Similarly, the polarization of acoustic phonons traveling along z rotates at a rate that is proportional to the Hall viscosity (Φ indicates the angle of the polarization away from the x axis, and the dashed line indicates the path of the polarization vector as the phonon propagates along z).

ducers attached to a sample (see Figure 4.2a). A radio-frequency voltage pulse actuates the piezoelectric transducer, generating a sound wave that travels through the sample, and is detected by a second shear-polarized piezoelectric transducer. The amplitude of sound detected by the receive transducer depends on the strength of Faraday rotation, which rotates the polarization of the incoming wave: the amplitude is maximum when the sound wave's polarization aligns with the traducer's polarization, and minimum when they are perpendicular. In general, varying the external magnetic field changes the Hall viscosity, which modifies the amount of Faraday rotation and, consequently, the amplitude of sound detected by the receive transducer.

One complication is that the amplitude of sound detected by the receive transducer depends not only on the amount of Faraday rotation, but also on sound attenuation. The attenuation can vary significantly with magnetic field, especially near a magnetic phase transition. This is particularly relevant for α-RuCl$_3$, where a spin-liquid state has been proposed near the critical field where long-range magnetic order is suppressed ($\approx$8 tesla for in-plane magnetic fields, see Figure 4.2b). Importantly for our experiment, sound attenuation is an *even* function of magnetic field—it depends on only the magnitude of the magnetic field, and not on the sign. In contrast, the acoustic Faraday effect is an *odd* function of magnetic field, changing sign with field reversal. To isolate the Faraday contribution, we measure the received sound amplitude for both positive and negative magnetic fields and then antisymmetrize the data. To address the limitation that a traditional pulse-echo reflection experiment cannot distinguish right-handed from left-handed rotations, we rotated the polarization of the receive transducer 45° with respect to that of the drive transducer (see Figure 4.2a). This configuration also enables an important experimental check: the field-antisymmetrized signal should switch sign when the sound propagation direction is reversed by swapping the drive and receive transducers.

Single-crystal samples of α-RuCl$_3$ were grown using the methods described in Kim *et al.* [138]. We select large single crystals with roughly parallel faces perpendicular to the c axis. We remove material by cleaving the sample until we produce two pristine, parallel faces, with overlapping area and no visible stacking faults. On two opposite c-axis faces, we sputter platinum bottom electrodes with titanium adhesion layers, followed by 1 μm thick, ZnO, mixed-mode (shear and longitudinal) piezoelectric trans-

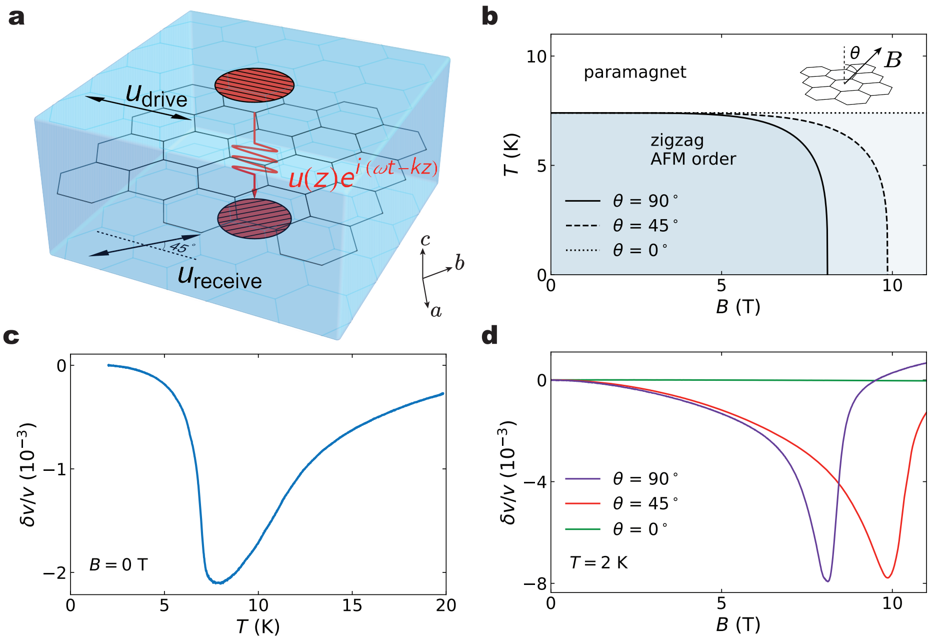

Figure 4.2: **Experimental geometry and sample characterization.** **a**, A piezoelectric drive transducer (upper red circle) sends a pulse of traverse sound (red line) along the c axis of a single-crystal α-RuCl$_3$ sample (indicated schematically by the honeycomb). The pulse is detected by a second, receive transducer (lower red circle) polarized 45° relative to the drive transducer. **b**, Schematic temperature-field phase diagram of α-RuCl$_3$ for different field orientations. The inset shows that θ is defined as the angle between the magnetic field $\boldsymbol{B}$ and the c axis (i.e. rotation is in the bc plane). We show the phase boundary for field along the b axis ($\theta = 90°$, sold line), field along the c axis ($\theta = 0°$, short dashed line), and field 45° between the b and c axes (long dashed line). **c**, The relative change in sound velocity as a function of temperature across the ordering temperature of $T_\text{N} = 7.5$ K. The sample exhibits a single magnetic phase transition, with no features near 14 K that would indicate a secondary structural and magnetic phase [135, 136]. **d**, The relative change in sound velocity as a function of magnetic field across the critical field of $B_c = 8$ T for $B||b$, $B_c = 10$ T for $\theta = 45°$, and for $B||c$ the sample remains in the ordered phase up to 12 tesla. The single phase transition indicates that the field is well-aligned with the b axis [137].

ducers, followed by platinum top electrodes on titanium adhesion layers. We excite the drive transducer using 50 ns bursts of $\approx$ 1.5 GHz radiofrequency voltage, amplify the signal detected at the receive transducer, and digitize it on an oscilloscope. We extract the amplitude and phase of the received signal using digital lockin. Further experimental details can be found in the Methods. The high quality of our samples is demonstrated by their single phase transition above 7 kelvin in zero magnetic field (Figure 4.2c), with no additional phase transitions at higher temperatures.

4.2.2 The acoustic Faraday effect of α-RuCl$_3$ for $B||c$

We first show data taken at 2 kelvin as a function of magnetic field from zero to 12 tesla applied along the c axis. In this configuration, the critical field to suppress magnetic order is over 30 tesla [141, 142], and the entire measurement is deep within the ordered antiferromagnetic state. This allows us to first demonstrate the acoustic Faraday effect in α-RuCl$_3$ without the additional complication of the magnetic phase transition (this configuration also has a thermal Hall effect, see Le Francois *et al.* [143]). Figure 4.3a shows the amplitude of transmitted sound as a function of time at a fixed field of $B = 10$ T along the c-axis and in the magnetically ordered state at $T = 2$ K. The mixed-mode transducers generate and detect both longitudinal and transverse sound waves, which travel at different speeds. The longitudinal and transverse modes are visible as distinct pulses in the time-series data, and we use both to validate our experimental method. Figure 4.3b (c) shows data that have been symmetrized (antisymmetrized) in magnetic field. Antisymmetrization completely removes the longitudinal signal, whereas transverse signal remains. This is consistent with the transverse signal arising due to the acoustic Faraday effect.

Figure 4.3d shows the amplitude of the transverse signal (at $t = t_{\text{trans.}}$) as a function of magnetic field for both positive and negative field directions ($\pm\boldsymbol{B}$), and panel e shows the same but for the opposite sound propagation direction. The asymmetry between $+\boldsymbol{B}$ and $-\boldsymbol{B}$ switches sign when the sound propagation direction $\boldsymbol{k}$ is switched to $-\boldsymbol{k}$ (by swapping the drive and receive cables at the top of the cryostat). The change in sign of the antisymmetric signal when changing $\boldsymbol{k}$ to $-\boldsymbol{k}$, the fact that the antisymmetric signal is non-zero only for transverse sound, and the vanishing of the antisymmetric signal at zero magnetic field, all confirm that the antisymmetric

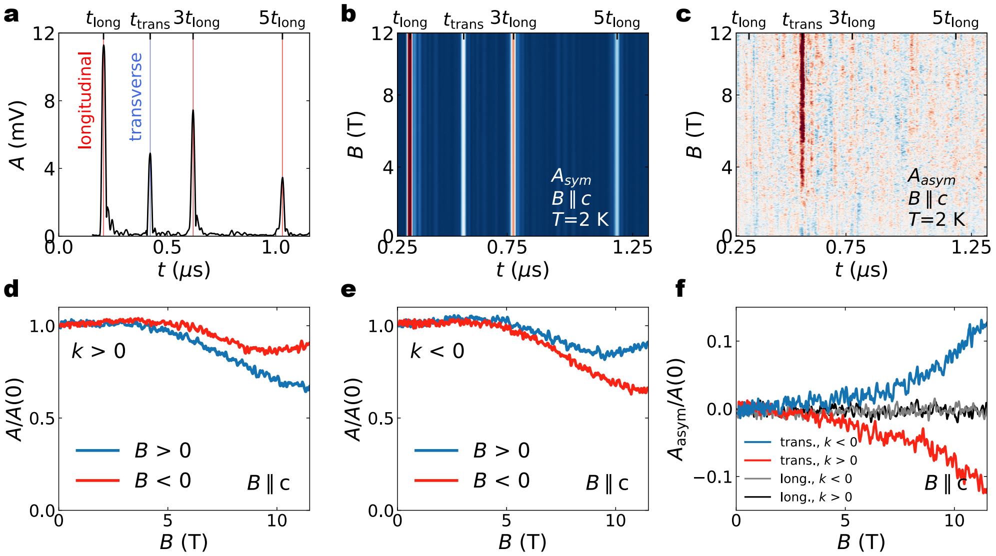

Figure 4.3: **Isolating the acoustic Faraday effect.** **a**, The raw signal detected using the setup shown in Figure 4.2a, for $B \| c = 10$ T and $T = 2$ K. Longitudinal and transverse pulses are identified based on their known speeds of sound [139, 140]. The first longitudinal pulse arrives at t_{long}, with echoes of this signal arriving at $3t_{\text{long}}$ and $5t_{\text{long}}$. The transverse pulse arrives at t_{trans} and is clearly separated in the time domain from the longitudinal signal. **b**, The field-symmetrized data show all longitudinal and transverse signals from 0 to 12 tesla. **c**, The field-antisymmetrized data contains only transverse signal because the Faraday effect rotates the transverse sound polarization in opposite directions for $\pm\boldsymbol{B}$, whereas it cannot rotate longitudinal polarization. **d**, The amplitude of transverse sound, normalized to its zero-field value, as a function of magnetic field for $\boldsymbol{B} \| c$ at $T = 2$ K. The magnetic field suppresses the amplitude more for positive field than for negative field. **e**, This behaviour switches when the propagation direction is switched, as expected for a Faraday effect. **f**, The field-antisymmetrized amplitude for both propagation directions. The transverse signal shows the characteristics of a Faraday effect, going to zero at $\boldsymbol{B} = 0$, and switching sign when $\boldsymbol{k} \to -\boldsymbol{k}$. The longitudinal signal, in contrast, is zero at all fields for both propagation directions.

signal is caused by the acoustic Faraday effect.

Having demonstrated that our procedure isolates the acoustic Faraday effect, we perform similar measurements in other experimental configurations: 1) we measure at temperatures up to 40 kelvin to test whether the Faraday effect is confined to the ordered state below 7 kelvin; 2) we measure with the magnetic field rotated 55° away from the *c* axis towards the *b* axis to determine how crossing the magnetic phase boundary affects the Faraday rotation; 3) we measure with magnetic field purely in the honeycomb plane to ensure that the Faraday signal disappears in this configuration; 4) we measure two additional samples of different thicknesses to ensure reproducibility; 5) we measure at additional ultrasonic frequencies. Data sets from (1) and (2) are analyzed below to extract the Hall viscosity of α-RuCl$_3$. Data sets from (3), (4), and (5) are shown in the Extended Data.

4.2.3 Extracting the Hall viscosity of α-RuCl$_3$

We now extract the phonon Hall viscosity by modeling our acoustic Faraday data using the elastic wave equation with viscous contributions included. The relationship between stress, $\boldsymbol{\sigma}$, and strain, ε, in a solid—Hooke's law—is modified at finite frequency by introducing the viscosity tensor $\hat{\eta}$:

$$\sigma_{ij} = c_{ijkl}\varepsilon_{kl} + \eta_{ijkl}\dot{\varepsilon}_{kl}, \tag{4.1}$$

where $\hat{c}$ is the elastic tensor and $\dot{\varepsilon}$ is the time derivative of strain. While the most familiar viscosity components are dissipative, time-reversal symmetry breaking—either intrinsic or from an applied magnetic field—allows for additional, *non*-dissipative "Hall" viscosities. A magnetic field component along the *c* axis of α-RuCl$_3$ activates the viscosity component η_{xzyz}.

When incorporated into the elastic wave equation, this viscosity couples transverse waves polarized along y to transverse waves polarized along x for waves propagating along the z direction. This coupling rotates linearly polarized transverse waves and produces an acoustic Faraday effect. Note that η_{xzyz} is allowed as long as there is *any* component of field along c. Other Hall viscosities are allowed when other field components are present—see Methods for a full symmetry analysis of the allowed Hall viscosities. The wave equation with Hall viscosity included is

$$\rho\omega^2\vec{u} = k^2\begin{bmatrix} c_{xzxz} & i\omega\eta_{xzyz} \\ -i\omega\eta_{xzyz} & c_{yzyz} \end{bmatrix}\vec{u}, \tag{4.2}$$

where ρ is the material density, ω is the sound frequency, $\vec{u}$ is the sound polarization vector, k is the sound wavenumber, and $c_{xzxz} \equiv c_{55}$ and $c_{yzyz} \equiv c_{44}$ are elastic constants.

Figure 4.4a and c show the antisymmetrized Faraday rotation data taken with $B \| c$ and B rotated 55° toward b, respectively. Both data sets are taken at 2 kelvin: the $B \| c$ data is entirely in the magnetically ordered state, whereas the $\theta = 55°$ data crosses the antiferromagnetic-to-paramagnetic transition at $B_\text{c} = 8.5$ T.

For $B \| c$, $c_{44} = c_{55}$ and we measure this elastic constant independently using the time-of-flight between echoes (see Figure 4.3a). The Hall viscosity η_{xzyz} is the only unknown in Equation 4.2 and is therefore directly determined by the antisymmetric amplitude (recall that field-*symmetric* changes in amplitude are removed through the antisymmetrization procedure).

When the magnetic field is rotated away from the c axis, the symmetry of the lattice is broken and c_{44} is no longer equal to c_{55}—an effect known as acoustic *birefringence*. Even though acoustic birefringence is even in magnetic field, it cannot be removed entirely through antisymmetrization in the presence of Hall viscosity. This likely produces the sharp spike in the antisymmetric signal just above B_c in Figure 4.4c, where the acoustic birefringence is largest. Because the effects of birefringence are difficult to disentangle from the viscous contribution near B_c, we exclude this narrow field region from the analysis. Note that birefringence alone cannot produce an antisymmetric signal; field-antisymmetric signals require Hall viscosity.

Figure 4.4b and d show the phonon Hall viscosity extracted from the antisymmetric data using Equation 4.2. For $B \| c$, the Hall viscosity increases continuously as a function of magnetic field up to $\eta_{xzyz} = 0.03$ mPa·s at 12 T. For $\theta = 55°$, the Hall viscosity peaks just above the critical field of 8.5 T, reaching a value of approximately 0.013 mPa·s.

4.2.4 Comparison to the thermal Hall effect

How do our measurements of phonon Hall viscosity relate to the thermal Hall effect in α-RuCl$_3$? The Hall viscosity can be interpreted in two ways. In an acoustic Faraday experiment with magnetic field along z, η_{zxzy} mixes a sound wave propagating along z and polarized along x with a sound wave propagating along z and polarized along y. In a thermal transport

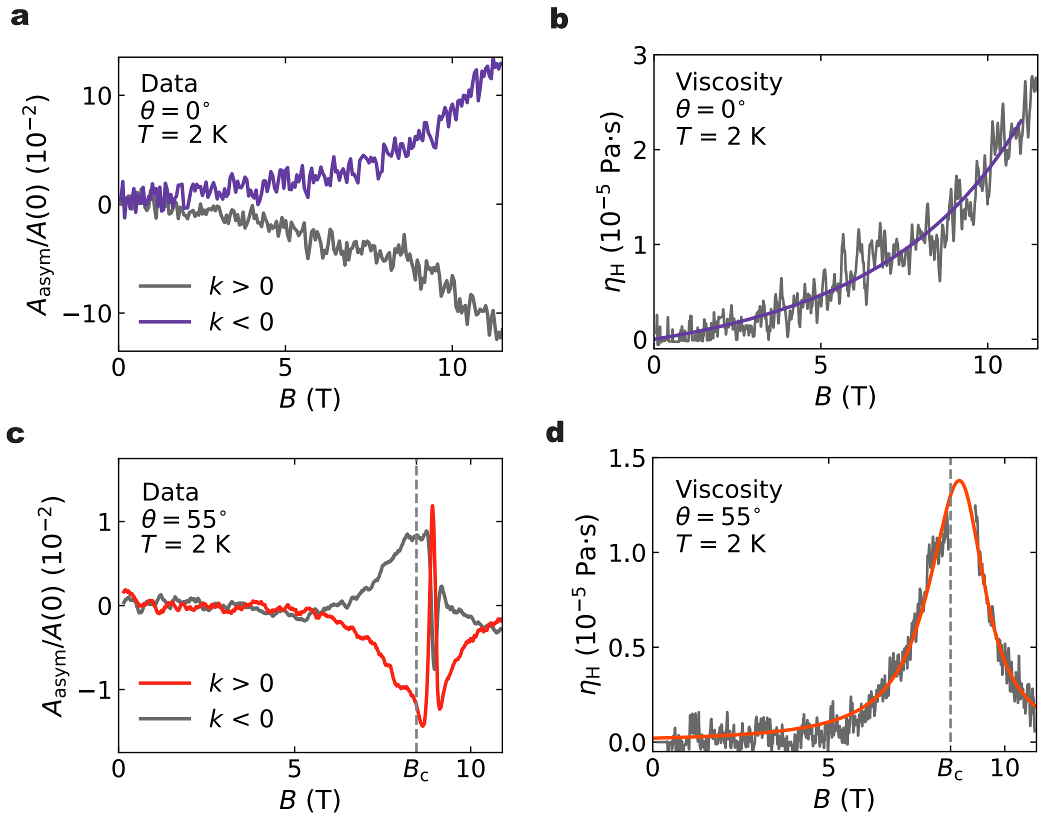

Figure 4.4: **The phonon Hall viscosity of α-RuCl$_3$.** **a**, The field-antisymmetrized Faraday signal normalized to the total zero-field signal, as a function of magnetic field for $B \| c$, at $T = 2$ K, for $\pm k$. **b**, The Hall viscosity extracted from the antisymmetric signal using Equation 4.2. The solid line is a guide to the eye. Panels **c** and **d** show the same data and analysis, but for magnetic field rotated 55° toward the b axis. The sharp feature slightly above B_c in panel **c** is likely a result of the small absolute signal size and the rapid change in speed of sound near this field. We have truncated this feature from the viscosity in panel **d**.

experiment with magnetic field along z, η_{xzyz} takes phonon heat flow along x and deflects it to heat flow along y. By symmetry, $\eta_{zxzy} = \eta_{xzyz}$, and thus our observation of phonon Hall viscosity suggests that phonons contribute to the thermal Hall effect in α-RuCl$_3$.

We can estimate the phonon contribution to the thermal Hall effect using our measurement of η_{xzyz} and the equations for acoustic energy transport in the presence of Hall viscosity—a detailed derivation is given in the Methods. The result is that Hall viscosity produces a thermal Hall conductivity: $\kappa_{xy} = \frac{\eta_{xzyz}}{\rho}C$, where ρ and C are α-RuCl$_3$'s density and specific heat, respectively. Note that the phonon Hall conductivity is independent of the phonon mean free path—it is intrinsic. The Hall conductivity can be compared with the longitudinal thermal conductivity: $\kappa_{xx} = \overline{v}_s lC$, where $\overline{v}_s$ is the average speed of sound and l is the phonon mean free path. The ratio of phonon Hall to phonon longitudinal thermal conductivities is then

$$\frac{\kappa_{xy}}{\kappa_{xx}} = \frac{\eta_{xzyz}}{\rho v_s l} = \frac{C}{\kappa_{xx}}\frac{\eta_{xzyz}}{\rho}. \tag{4.3}$$

Using our measured value of $\eta_{xzyz} = 1.3 \times 10^{-5}$ Pa·s, and the measured values of κ_{xx} and the specific heat at 10 K with $\mathbf{B}||c$ [143, 144], we estimate $\kappa_{xy}/\kappa_{xx} = 10^{-4}$—only a factor of 4 smaller than what is observed in thermal transport experiments under the same conditions by LeFrancois *et al.* [143]. Note that this estimate is a lower bound on the total phonon contribution to κ_{xy}: the full κ_{xy} will receive contributions from all three acoustic branches (here was have only accounted for one), and from all 4 viscosity tensor elements that are allowed for this magnetic field orientation (e.g. η_{xyxz}, etc.) There is no reason to expect that the different viscosities are substantially different, and first-principles calculations by Dhakal *et al.* indeed suggest they are all similar in magnitude [145]. In addition, finite Hall viscosity enables phonon side-jump scattering that will also contribute to κ_{xy}. Thus the total κ_{xy} contribution from phonon Hall viscosity could easily be a factor of 10 larger than what we estimate here.

Next, we analyze the temperature dependence of the Hall viscosity for $B||c$. Figure 4.5a shows that, aside from a sharp drop near the magnetic phase transition at 7.5 K, the Hall viscosity is only weakly temperature dependent up to 40 kelvin. This clearly demonstrates that phonon Hall viscosity in α-RuCl$_3$ is not due to the coherent hybridization of acoustic phonons and magnons into chiral "magnetopolarons" [127]—the conventional mechanism of the acoustic Faraday effect. We can compare the temperature dependence of the Hall viscosity to the thermal Hall effect by plotting η_{xzyz} alongside $\rho\kappa_{xy}/C$, which has units of viscosity. These quantities are the same order of magnitude and have qualitatively similar temperature dependencies: both showing minima near T_{N} and extending to temperatures much greater than T_{N}. The drop in η_{xzyz} near T_{N} may be intrinsic, or it may be due to strong phonon scattering due to thermal fluctuations of the order parameter at the antiferromagnetic phase transition. Although η_{xzyz} itself does not depend on the phonon mean free path, our ability to measure it does when the mean free path of our ultrasonic phonons becomes much shorter than the sample size, which happens near T_{N}.

Finally, in Figure 4.5b we compare the magnetic field dependence of the Hall viscosity at $\theta = 55°$ to the field dependence of the thermal Hall effect measured with magnetic field purely along the a axis. Both quantities begin to rise above 5 tesla and are peaked *above* the critical field where long-range order is suppressed. As both the static spin susceptibility and inelastic neutron scattering show that the magnetic state becomes soft at B_c [146, 147], this suggests that the phonon Hall viscosity originates from coupling between phonons and the spin degrees of freedom. Note that the thermal Hall effect in this field configuration—with $B||a$—is sensitive to many more viscosity tensor elements than the Faraday effect is: our measurement always probes η_{xzyz}, whereas κ_{xy} for $B||a$ is sensitive to η_{xzxy}, η_{xyxx}, η_{yzxx}, η_{yyyz} and η_{yyxz}. Thus, a direct quantitative comparison between these two quantities is not valid for this field orientation; the purpose of Figure 4.5b is to show that both quantities are sensitive to the proximity of the critical field where order is suppressed. Also note that, while crystal symmetry constrains κ_{xy} to be zero when the magnetic field purely along b, the same symmetry argument does not require all viscosity components to vanish for this field orientation (this is discussed further in Dhakal *et al.* [145]).

4.3 Discussion

Having shown that phonons can account for a significant fraction—if not all—of the observed thermal Hall effect in α-RuCl$_3$, we turn to the question of *why* the phonons in α-RuCl$_3$ have Hall viscosity. As noted above, the

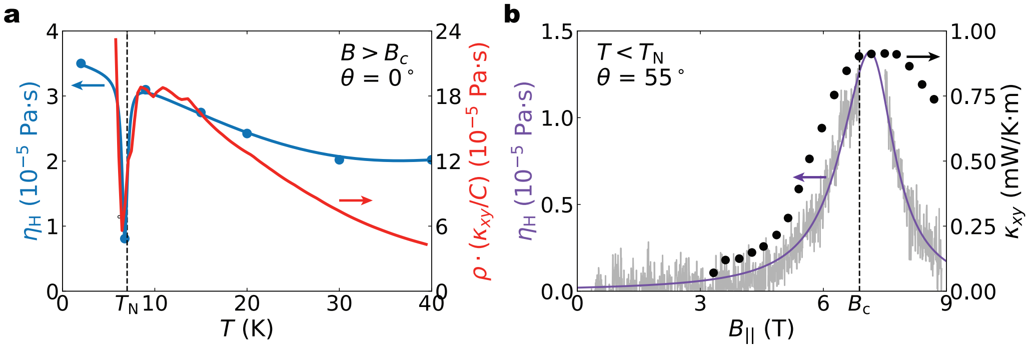

Figure 4.5: **Temperature and field dependence of the phonon Hall viscosity.** **a**, The phonon Hall viscosity as a function of temperature for **B**$\|c$ = 12 T. Blue circles are measured data points, and the blue line is a guide to the eye. The quantity $\rho\kappa_{xy}/C$, calculated using κ_{xy} from LeFrancois *et al.* [143] and C from Widman *et al.* [148], is plotted in red for comparison. **b**, The phonon Hall viscosity measured with **B** rotated 55° from c toward b, plotted as a function of in-plane magnetic field at T = 2 K. The κ_{xy} data are measured with **B**$\|a$ and are taken from Czajka *et al.* [149].

observation of Hall viscosity at temperatures well above the antiferromagnetic phase transition rules out the conventional mechanism of magnon-phonon hybridization [127]. Indeed, neutron scattering finds a broad continuum of excitations at low energy and momentum rather than distinct, sharp magnon bands [150, 151].

Can incoherent magnetic excitations produce phonon Hall viscosity? Strong spin-lattice coupling is clearly present in α-RuCl$_3$, as evidenced by the large changes in sound velocity at T_N and B_c (Figure 4.2 and Hauspurg *et al.* [139]), which are two orders of magnitude larger than those typically seen at superconducting phase transitions [152, 153]. Dhakal *et al.* [145] used a first-principles based approach to calculate the microscopic spin-lattice couplings in α-RuCl$_3$, and they demonstrated that the resultant phonon Hall viscosities can account for the full magnitude of the measured thermal Hall effect. Although they use a two-dimensional model that does not access the same viscosity component that we do in our experiment (η_{xzyz}), they find that all five in-plane viscosity components are the same order of magnitude—and, strikingly, the same order of magnitude as the value we measure for η_{xzyz}. Our measurements therefore provide experimental evidence that the phonon Hall viscosity in α-RuCl$_3$ is indeed large enough to account for the thermal Hall effect, calling into question the existence of a quantized contribution from Majorana edge modes. Phonon Hall viscosity also likely explains the unusual thermal Hall effects found in many other magnetic insulators. However, non-magnetic materials, such as SrTiO$_3$, likely require a different mechanism.

Beyond clarifying the origin of the thermal Hall effect in α-RuCl$_3$, our measurements provide a direct experimental link between phonon Hall viscosity and phonon Berry curvature—connecting two concepts that have, until now, remained largely theoretical [123, 124, 115, 114, 116]. Conventionally, viscosity is thought of as a long-wavelength property of sound, whereas Berry curvature is associated with the microscopic wave functions of phonons. The connection between phonon Hall viscosity and Berry curvature can be demonstrated by examining how the Hamiltonian of the system, $\mathcal{H}$, changes under an applied strain: $\frac{\partial \mathcal{H}}{\partial \varepsilon_{ij}}$. The stress of a state $|\Psi\rangle$ is the expectation value of this derivative: $\sigma_{ij} = \left\langle \Psi \middle| \frac{\partial \mathcal{H}}{\partial \varepsilon_{ij}} \middle| \Psi \right\rangle$. If the state of the system varies trivially with strain, then this reduces to the classical definition of stress: $\sigma_{ij} = \partial E / \partial \varepsilon_{ij} \equiv c_{ijkl}\varepsilon_{kl}$, where E is the state's energy. If, however, the system gains a geometric phase when traversing a path in strain space, then the expectation value acquires Berry curvature,

$$\sigma_{ij} = c_{ijkl}\varepsilon_{kl} + \Omega_{ijkl}\dot{\varepsilon}_{kl}, \tag{4.4}$$

where the full expression for Ω_{ijkl} in terms of strain is given by Avron *et al.* [123]. This expression can be compared to Equation 4.1,

$$\sigma_{ij} = c_{ijkl}\varepsilon_{kl} + \eta_{ijkl}\dot{\varepsilon}_{kl},$$

making the correspondence between Ω_{ijkl} and η_{ijkl} clear. It can be helpful to interpret Ω_{ijkl} as a "real-space" Berry curvature—it gives rise to a geometric phase when the crystal lattice is moved around a closed loop by an oscillating strain, such as the one created by a sound wave. This is analogous to the "momentum-space" Berry curvature of Bloch electrons, which gain geometric phases when traversing closed paths in momentum space. Where Bloch electrons experience a non-dissipative force from Berry curvature that leads to the anomalous Hall effect, the lattice (i.e. phonons and sound waves) experiences a non-dissipative Hall viscosity that leads to the thermal Hall and acoustic Faraday effects.

In general, a variety of mechanisms can generate phonon Berry curvature and Hall viscosity. For example, electron-phonon coupling can generate phonon Berry curvature and Hall viscosity in quantum Hall systems, topological insulators, and topological superconductors [124]. Similarly for spin-lattice coupling in chiral spin liquids [114]. Thus, our measurements do not rule out the possibility of spinon excitations in α-RuCl$_3$. They do, however, require that phonons account for at least a significant fraction of the thermal Hall effect. More generally, we have demonstrated that the acoustic Faraday effect is a direct probe of phonon Hall viscosity or, equivalently, phonon Berry curvature. Because phonon Hall viscosity is a property of many exotic phases, including topological superconductors and 3D quantum Hall states, acoustic Faraday rotation measurements will be a valuable tool for discovering and characterizing these states of matter.

4.4 Heat flux in the presence of Hall viscosity: semiclassical estimate of the thermal Hall conductivity

To estimate the intrinsic contribution to the thermal Hall effect due to Hall viscosity, we consider the transverse energy flux generated by thermal phonons. Thermally generated stress at frequency ω, $\sigma(\omega)$, carries an acoustic energy current

$$j_i = \mathrm{Re}[\sigma_{ij}(\omega)\dot{u}_j] = \mathrm{Re}[\left(c_{ijkl}\varepsilon_{ij} + \eta_{ijkl}\dot{\varepsilon}_{kl}\right)\dot{u}_j], \tag{4.5}$$

where $\dot{u}$ is the time derivative of displacements due to the stress. [154] Longitudinal thermal transport occurs because temperature gradients produce gradients in the amplitude (energy occupations) of thermal phonons. For example, if we consider z polarized thermal strains propagating in the x-direction with wave vector q_x, so that $u = u_z(x)e^{i(\omega t - q_x x)}$, there is a contribution to the energy flux

$$j_x = \mathrm{Re}[\sigma_{xz}\dot{u}_z] = \mathrm{Re}[i\omega c_{55}\varepsilon_{xz}u_z] = c_{55}\omega q_x u_z^2, \tag{4.6}$$

where we use Hooke's law $\sigma_{xz} = iq_x c_{55} u_z$ for this particular component. Strains involving displacements along x and y also contribute to j_x, bring-ing in terms proportional to c_{11} and c_{66} respectively. Taken together we can combine these contributions, using an average elastic modulus $\overline{c}$, to obtain

$$j_x = \overline{c}\, q_x \omega\, u^2 = \frac{\overline{c}}{\rho v_s} \left(\rho \omega^2 u^2\right) = v_s \left(\rho \omega^2 u^2\right), \tag{4.7}$$

where v_s is an average speed of sound and ρ is the density. Because these are thermally generated, random strains, there is no preferred direction for q_x and, in the absence of a thermal gradient, the net energy flux is zero.

However, in the presence of a thermal gradient along x, there is heat transport. Conceptually, the thermal phonons travel a mean free distance ℓ before they scatter and equilibrate with the local lattice temperature. The net acoustic energy flux is then

$$j_{x,\mathrm{net}} = j_x(x+\ell) - j_x(x-\ell) = v_s \left(\rho\omega^2 u(x+\ell)^2 - \rho\omega^2 u(x-\ell)^2\right). \tag{4.8}$$

Recognizing that $\rho\omega^2 u^2$ is the phonon energy density, U, we write

$$j_{x,\mathrm{net}} \approx v_s \ell \frac{\partial U}{\partial x} = v_s \ell C \frac{\partial T}{\partial x} = \kappa_{xx} \frac{\partial T}{\partial x} \tag{4.9}$$

where C is the heat capacity, and we identify the longitudinal thermal conductivity $\kappa_{xx} = v_s \ell C$. This thermal conductivity is extrinsic in the sense that it is proportional to the phonon mean free path.

Now consider the heat flux when there is a non-zero Hall viscosity. In particular, we consider an applied magnetic field along the c axis of α-RuCl$_3$. Returning to Equation 4.5, we find that the Hall viscosity produces a transverse energy flux where, for example, the viscosity η_{xzyz} produces

$$j_y = \mathrm{Re}[2\eta_{xzyz}\dot{\varepsilon}_{xz}\dot{u}_z] = \eta_{xzyz}\omega^2 \frac{\partial u_z}{\partial x} u_z = \frac{\eta_{xzyz}}{2\rho} \frac{\partial}{\partial x} \left(\rho\omega^2 u_z^2\right), \tag{4.10}$$

and the other two viscosity components η_{yyxy} and η_{yxxx} contribute similar terms. In the absence of a temperature gradient, there will be no net transverse heat flow, but if we enforce an amplitude gradient by applying a temperature gradient along the x-direction, then we transfer the spatial derivative to the applied temperature gradient and write

$$j_y = \frac{\overline{\eta}}{\rho} C \frac{\partial T}{\partial x}, \tag{4.11}$$

where $\overline{\eta}$ is an average Hall viscosity. Note that, while the transverse energy flux requires a longitudinal temperature gradient, its magnitude does not depend on the phonon mean free path—this effect is intrinsic.

Finally, the thermal Hall angle—the ratio of the thermal Hall conductivity and longitudinal thermal conductivity—is equal to the ratio of the transverse and longitudinal heat currents. Using Equation 4.9 and Equation 4.11 we recover the estimate

$$\frac{\kappa_{xy}}{\kappa_{xx}} = \frac{\eta}{\rho}\frac{C}{\kappa_{xx}}. \tag{4.12}$$

Note that using this equation to compare our measurement of η_{xzyz} to the thermal Hall effect depends on the Hall viscosity being only weakly dependent on frequency (since thermal measurements access much higher phonon frequencies than do our ultrasound measurements). This assumption is justified by the calculations of Dhakal *et al.*, who find that the Hall viscosity is independent of frequency for small wavevector.

Bibliography

[1] Sam Mugiraneza and Alannah M. Hallas. "Tutorial: a beginners guide to interpreting magnetic susceptibility data with the Curie-Weiss law". en. In: *Communications Physics* 5.1 (Apr. 2022). Publisher: Nature Publishing Group, p. 95. ISSN: 2399-3650. DOI: `10.1038/s42005-022-00853-y`. URL: `https://www.nature.com/articles/s42005-022-00853-y` (visited on 10/22/2025).

[2] Farrel W. Lytle. "XRay Diffractometry of LowTemperature Phase Transformations in Strontium Titanate". In: *Journal of Applied Physics* 35.7 (July 1964), pp. 2212–2215. ISSN: 0021-8979. DOI: `10.1063/1.1702820`. URL: `https://doi.org/10.1063/1.1702820` (visited on 10/22/2025).

[3] Helen D. Megaw. "Temperature changes in the crystal structure of barium titanium oxide". In: *Proceedings of the Royal Society of London. Series A. Mathematical and Physical Sciences* 189.1017 (Jan. 1997). Publisher: Royal Society, pp. 261–283. DOI: `10.1098/rspa.1947.0038`. URL: `https://royalsocietypublishing.org/doi/10.1098/rspa.1947.0038` (visited on 10/22/2025).

[4] Andrea Damascelli. "Angle-resolved photoemission studies of the cuprate superconductors". In: *Reviews of Modern Physics* 75.2 (2003), pp. 473–541. DOI: `10.1103/RevModPhys.75.473`.

[5] Jonathan A. Sobota. "Angle-resolved photoemission studies of quantum materials". In: *Reviews of Modern Physics* 93.2 (2021). DOI: `10.1103/RevModPhys.93.025006`.

[6] Patrick A. Lee. "Doping a Mott insulator: Physics of high-temperature superconductivity". In: *Reviews of Modern Physics* 78.1 (2006), pp. 17–85. DOI: `10.1103/RevModPhys.78.17`.

[7] Friedrich Krien et al. “Explaining the pseudogap through damping and antidamping on the Fermi surface by imaginary spin scattering”. en. In: *Communications Physics* 5.1 (Dec. 2022). Publisher: Nature Publishing Group, p. 336. ISSN: 2399-3650. DOI: `10.1038/s42005-022-01117-5`. URL: `https://www.nature.com/articles/s42005-022-01117-5` (visited on 10/22/2025).

[8] B. Keimer et al. “From quantum matter to high-temperature superconductivity in copper oxides”. en. In: *Nature* 518.7538 (Feb. 2015). Publisher: Nature Publishing Group, pp. 179–186. ISSN: 1476-4687. DOI: `10.1038/nature14165`. URL: `https://www.nature.com/articles/nature14165` (visited on 10/22/2025).

[9] Leon Balents. “Spin liquids in frustrated magnets”. en. In: *Nature* 464.7286 (Mar. 2010). Publisher: Nature Publishing Group, pp. 199–208. ISSN: 1476-4687. DOI: `10.1038/nature08917`. URL: `https://www.nature.com/articles/nature08917` (visited on 10/22/2025).

[10] Lucile Savary and Leon Balents. “Quantum spin liquids: a review”. en. In: *Reports on Progress in Physics* 80.1 (Nov. 2016). Publisher: IOP Publishing, p. 016502. ISSN: 0034-4885. DOI: `10.1088/0034-4885/80/1/016502`. URL: `https://doi.org/10.1088/0034-4885/80/1/016502` (visited on 10/22/2025).

[11] Nicolas Doiron-Leyraud et al. “Quantum oscillations and the Fermi surface in an underdoped high-Tc superconductor”. en. In: *Nature* 447.7144 (May 2007). Publisher: Nature Publishing Group, pp. 565–568. ISSN: 1476-4687. DOI: `10.1038/nature05872`. URL: `https://www.nature.com/articles/nature05872` (visited on 10/20/2025).

[12] J. R. Kirtley et al. “Angle-resolved phase-sensitive determination of the in-plane gap symmetry in YBa2Cu3O7”. en. In: *Nature Physics* 2.3 (Mar. 2006). Publisher: Nature Publishing Group, pp. 190–194. ISSN: 1745-2481. DOI: `10.1038/nphys215`. URL: `https://www.nature.com/articles/nphys215` (visited on 10/22/2025).

[13] H. Murayama. “Effect of quenched disorder on the quantum spin liquid state of the triangular-lattice antiferromagnet ¡math xmlns=”http://www.w3.org/1998/Math/MathML”¿¡mrow¿¡mn¿1¡/mn¿¡mi¿T¡/mi¿¡m

In: *Physical Review Research* 2.1 (2020). DOI: `10.1103/PhysRevResearch.2.013099`.

[14] Y. J. Yu. "Heat transport study of the spin liquid candidate 1T-TaS$_2$". In: *Physical Review B* 96.8 (2017). DOI: `10.1103/PhysRevB.96.081111`.

[15] D. C. Tsui. "Two-Dimensional Magnetotransport in the Extreme Quantum Limit". In: *Physical Review Letters* 48.22 (1982), pp. 1559–1562. DOI: `10.1103/PhysRevLett.48.1559`.

[16] Horst L. Stormer. "The fractional quantum Hall effect". In: *Reviews of Modern Physics* 71.2 (1999), S298–S305. DOI: `10.1103/RevModPhys.71.S298`.

[17] K. D. Nelson et al. "Odd-Parity Superconductivity in Sr2RuO4". In: *Science* 306.5699 (Nov. 2004). Publisher: American Association for the Advancement of Science, pp. 1151–1154. DOI: `10.1126/science.1103881`. URL: `https://www.science.org/doi/10.1126/science.1103881` (visited on 10/20/2025).

[18] A. Pustogow et al. "Constraints on the superconducting order parameter in Sr2RuO4 from oxygen-17 nuclear magnetic resonance". en. In: *Nature* 574.7776 (Oct. 2019). Publisher: Nature Publishing Group, pp. 72–75. ISSN: 1476-4687. DOI: `10.1038/s41586-019-1596-2`. URL: `https://www.nature.com/articles/s41586-019-1596-2` (visited on 10/22/2025).

[19] Sayak Ghosh et al. "Thermodynamic evidence for a two-component superconducting order parameter in Sr2RuO4". en. In: *Nature Physics* 17.2 (Feb. 2021). Publisher: Nature Publishing Group, pp. 199–204. ISSN: 1745-2481. DOI: `10.1038/s41567-020-1032-4`. URL: `https://www.nature.com/articles/s41567-020-1032-4` (visited on 10/22/2025).

[20] Austin W. Lindquist and Hae-Young Kee. "Reconciling the phase shift in Josephson junction experiments with even-parity superconductivity in Sr 2 RuO 4". en. In: *Physical Review B* 107.1 (Jan. 2023), p. 014506. ISSN: 2469-9950, 2469-9969. DOI: `10.1103/PhysRevB.107.014506`. URL: `https://link.aps.org/doi/10.1103/PhysRevB.107.014506` (visited on 10/20/2025).

[21] Y. Kasahara et al. "Majorana quantization and half-integer thermal quantum Hall effect in a Kitaev spin liquid". en. In: *Nature* 559.7713 (July 2018). Publisher: Nature Publishing Group, pp. 227–231. ISSN: 1476-4687. DOI: `10.1038/s41586-018-0274-0`. URL: `https://www.nature.com/articles/s41586-018-0274-0` (visited on 10/22/2025).

[22] G. Grissonnanche et al. "Giant thermal Hall conductivity in the pseudogap phase of cuprate superconductors". en. In: *Nature* 571.7765 (July 2019). Publisher: Nature Publishing Group, pp. 376–380. ISSN: 1476-4687. DOI: `10.1038/s41586-019-1375-0`. URL: `https://www.nature.com/articles/s41586-019-1375-0` (visited on 10/20/2025).

[23] Sangwoo Sim. "Sizable Suppression of Thermal Hall Effect upon Isotopic Substitution in ¡math xmlns="http://www.w3.org/1998/Math/MathML" display="inline"¿¡msub¿¡mrow¿¡mi¿SrTiO¡/mi¿¡/mrow¿¡mrow¿¡mn¿3¡/mn¿¡/mrow¿¡/ In: *Physical Review Letters* 126.1 (2021). DOI: `10.1103/PhysRevLett.126.015901`.

[24] Yuji Hirokane. "Phononic thermal Hall effect in diluted terbium oxides". In: *Physical Review B* 99.13 (2019). DOI: `10.1103/PhysRevB.99.134419`.

[25] A. Ataei et al. "Phonon chirality from impurity scattering in the antiferromagnetic phase of Sr2IrO4". en. In: *Nature Physics* 20.4 (Apr. 2024). Publisher: Nature Publishing Group, pp. 585–588. ISSN: 1745-2481. DOI: `10.1038/s41567-024-02384-5`. URL: `https://www.nature.com/articles/s41567-024-02384-5` (visited on 10/23/2025).

[26] N. W. Ashcroft and N. D. Mermin. *Solid State Physics*. Holt-Saunders, 1976.

[27] C. Strohm, G. L. J. A. Rikken, and P. Wyder. "Phenomenological Evidence for the Phonon Hall Effect". en. In: *Physical Review Letters* 95.15 (Oct. 2005), p. 155901. ISSN: 0031-9007, 1079-7114. DOI: `10.1103/PhysRevLett.95.155901`. URL: `https://link.aps.org/doi/10.1103/PhysRevLett.95.155901` (visited on 10/21/2025).

[28] Bart A. Van Tiggelen. “Transverse Diffusion of Light in Faraday-Active Media”. en. In: *Physical Review Letters* 75.3 (July 1995), pp. 422–424. ISSN: 0031-9007, 1079-7114. DOI: `10.1103/PhysRevLett.75.422`. URL: `https://link.aps.org/doi/10.1103/PhysRevLett.75.422` (visited on 10/21/2025).

[29] G. L. J. A. Rikken and B. A. van Tiggelen. “Observation of magnetically induced transverse diffusion of light”. en. In: *Nature* 381.6577 (May 1996). Publisher: Nature Publishing Group, pp. 54–55. ISSN: 1476-4687. DOI: `10.1038/381054a0`. URL: `https://www.nature.com/articles/381054a0` (visited on 10/21/2025).

[30] C. Kittel. “Interaction of Spin Waves and Ultrasonic Waves in Ferromagnetic Crystals”. In: *Physical Review* 110.4 (May 1958). Publisher: American Physical Society, pp. 836–841. DOI: `10.1103/PhysRev.110.836`. URL: `https://link.aps.org/doi/10.1103/PhysRev.110.836` (visited on 09/12/2025).

[31] H. Matthews and R. C. LeCraw. “Acoustic Wave Rotation by Magnon-Phonon Interaction”. In: *Physical Review Letters* 8.10 (May 1962). Publisher: American Physical Society, pp. 397–399. DOI: `10.1103/PhysRevLett.8.397`. URL: `https://link.aps.org/doi/10.1103/PhysRevLett.8.397` (visited on 08/19/2025).

[32] Y. Onose et al. “Observation of the Magnon Hall Effect”. In: *Science* 329.5989 (July 2010). Publisher: American Association for the Advancement of Science, pp. 297–299. DOI: `10.1126/science.1188260`. URL: `https://www.science.org/doi/10.1126/science.1188260` (visited on 10/21/2025).

[33] Hosho Katsura. “Theory of the Thermal Hall Effect in Quantum Magnets”. In: *Physical Review Letters* 104.6 (2010). DOI: `10.1103/PhysRevLett.104.066403`.

[34] Ryo Matsumoto. “Theoretical Prediction of a Rotating Magnon Wave Packet in Ferromagnets”. In: *Physical Review Letters* 106.19 (2011). DOI: `10.1103/PhysRevLett.106.197202`.

[35] Jeffrey G. Rau and Michel J. P. Gingras. “Frustrated Quantum Rare-Earth Pyrochlores”. en. In: *Annual Review of Condensed Matter Physics* 10.Volume 10, 2019 (Mar. 2019). Publisher: Annual Reviews, pp. 357–386. ISSN: 1947-5454, 1947-5462. DOI: `10.1146/`

annurev - conmatphys - 022317 - 110520. URL: https://www.annualreviews.org/content/journals/10.1146/annurev-conmatphys-022317-110520 (visited on 10/23/2025).

[36] J. S. Gardner et al. "Neutron scattering studies of the cooperative paramagnet pyrochlore Tb$_2$Ti$_2$O$_7$". In: *Phys. Rev. B* 64.22 (Nov. 2001). Publisher: American Physical Society, p. 224416. DOI: 10.1103/PhysRevB.64.224416. URL: https://link.aps.org/doi/10.1103/PhysRevB.64.224416.

[37] J. S. Gardner et al. "Dynamic frustrated magnetism in Tb$_2$Ti$_2$O$_7$ at 50 mK". In: *Phys. Rev. B* 68.18 (Nov. 2003). Publisher: American Physical Society, p. 180401. DOI: 10.1103/PhysRevB.68.180401. URL: https://link.aps.org/doi/10.1103/PhysRevB.68.180401.

[38] T. Fennell. "Power-Law Spin Correlations in the Pyrochlore Antiferromagnet ¡span class="aps-inline-formula"¿¡math xmlns="http://www.w3.org/1998
display="inline"¿¡msub¿¡mi¿Tb¡/mi¿¡mn¿2¡/mn¿¡/msub¿¡msub¿¡mi¿Ti¡/mi¿¡mn¿2¡/m
mathvariant="normal"¿O¡/mi¿¡mn¿7¡/mn¿¡/msub¿¡/math¿¡/span¿". In: *Physical Review Letters* 109.1 (2012). DOI: 10.1103/PhysRevLett.109.017201.

[39] Max Hirschberger et al. "Large thermal Hall conductivity of neutral spin excitations in a frustrated quantum magnet". In: *Science* 348.6230 (Apr. 2015). Publisher: American Association for the Advancement of Science, pp. 106–109. DOI: 10.1126/science.1257340. URL: https://www.science.org/doi/10.1126/science.1257340 (visited on 10/21/2025).

[40] M. Majumder. "Anisotropic ¡span class="aps-inline-formula"¿¡math
xmlns="http://www.w3.org/1998/Math/MathML"¿¡msup¿¡mrow¿¡mi¿Ru¡/mi¿¡/mro
¡/mo¿¡/mrow¿¡/msup¿¡mo¿¡/mo¿¡mrow¿¡mn¿4¡/mn¿¡msup¿¡mi¿d¡/mi¿¡mn¿5¡/mn¿¡/
magnetism in the ¡span class="aps-inline-formula"¿¡math xmlns="http://www.w3.org/
honeycomb system: Susceptibility, specific heat, and zero-field NMR". In: *Physical Review B* 91.18 (2015). DOI: 10.1103/PhysRevB.91.180401.

[41] Yumi Kubota. "Successive magnetic phase transitions in ¡span
class="aps-inline-formula"¿¡math xmlns="http://www.w3.org/1998/Math/MathML"¿

XY-like frustrated magnet on the honeycomb lattice". In: *Physical Review B* 91.9 (2015). DOI: `10.1103/PhysRevB.91.094422`.

[42] K. W. Plumb. "α-RuCl$_3$: A spin-orbit assisted Mott insulator on a honeycomb lattice". In: *Physical Review B* 90.4 (2014). DOI: `10.1103/PhysRevB.90.041112`.

[43] Arnab Banerjee et al. "Excitations in the field-induced quantum spin liquid state of -RuCl3". en. In: *npj Quantum Materials* 3.1 (Feb. 2018). Publisher: Nature Publishing Group, p. 8. ISSN: 2397-4648. DOI: `10.1038/s41535-018-0079-2`. URL: `https://www.nature.com/articles/s41535-018-0079-2` (visited on 10/23/2025).

[44] K. A. Modic et al. "Scale-invariant magnetic anisotropy in RuCl3 at high magnetic fields". en. In: *Nature Physics* 17.2 (Feb. 2021). Publisher: Nature Publishing Group, pp. 240–244. ISSN: 1745-2481. DOI: `10.1038/s41567-020-1028-0`. URL: `https://www.nature.com/articles/s41567-020-1028-0` (visited on 10/23/2025).

[45] Xu-Guang Zhou et al. "Possible intermediate quantum spin liquid phase in -RuCl3 under high magnetic fields up to 100 T". en. In: *Nature Communications* 14.1 (Sept. 2023). Publisher: Nature Publishing Group, p. 5613. ISSN: 2041-1723. DOI: `10.1038/s41467-023-41232-7`. URL: `https://www.nature.com/articles/s41467-023-41232-7` (visited on 10/23/2025).

[46] Alexei Kitaev. "Anyons in an exactly solved model and beyond". In: *Annals of Physics*. January Special Issue 321.1 (Jan. 2006), pp. 2–111. ISSN: 0003-4916. DOI: `10.1016/j.aop.2005.10.005`. URL: `https://www.sciencedirect.com/science/article/pii/S0003491605002381` (visited on 10/23/2025).

[47] T. Yokoi et al. "Half-integer quantized anomalous thermal Hall effect in the Kitaev material candidate -RuCl3". In: *Science* 373.6554 (July 2021). Publisher: American Association for the Advancement of Science, pp. 568–572. DOI: `10.1126/science.aay5551`. URL: `https://www.science.org/doi/10.1126/science.aay5551` (visited on 10/23/2025).

[48] Peter Czajka et al. “Planar thermal Hall effect of topological bosons in the Kitaev magnet -RuCl3”. en. In: *Nature Materials* 22.1 (Jan. 2023). Publisher: Nature Publishing Group, pp. 36–41. ISSN: 1476-4660. DOI: `10.1038/s41563-022-01397-w`. URL: `https://www.nature.com/articles/s41563-022-01397-w` (visited on 10/22/2025).

[49] G. Grissonnanche et al. “Chiral phonons in the pseudogap phase of cuprates”. en. In: *Nature Physics* 16.11 (Nov. 2020). Publisher: Nature Publishing Group, pp. 1108–1111. ISSN: 1745-2481. DOI: `10.1038/s41567-020-0965-y`. URL: `https://www.nature.com/articles/s41567-020-0965-y` (visited on 10/22/2025).

[50] Xiaokang Li. “Phonon Thermal Hall Effect in Strontium Titanate”. In: *Physical Review Letters* 124.10 (2020). DOI: `10.1103/PhysRevLett.124.105901`.

[51] Lu Chen et al. “Large phonon thermal Hall conductivity in the antiferromagnetic insulator Cu3TeO6”. In: *Proceedings of the National Academy of Sciences* 119.34 (Aug. 2022). Publisher: Proceedings of the National Academy of Sciences, e2208016119. DOI: `10.1073/pnas.2208016119`. URL: `https://www.pnas.org/doi/10.1073/pnas.2208016119` (visited on 11/02/2025).

[52] Marie-Eve Boulanger et al. “Thermal Hall conductivity in the cuprate Mott insulators Nd2CuO4 and Sr2CuO2Cl2”. en. In: *Nature Communications* 11.1 (Oct. 2020). Publisher: Nature Publishing Group, p. 5325. ISSN: 2041-1723. DOI: `10.1038/s41467-020-18881-z`. URL: `https://www.nature.com/articles/s41467-020-18881-z` (visited on 11/02/2025).

[53] Rohit Sharma, Martin Valldor, and Thomas Lorenz. “Phonon thermal Hall effect in nonmagnetic ${\mathrm{Y}}_{2}{\mathrm{Ti}}_{2}{\mathrm{O}}_
In: *Physical Review B* 110.10 (Sept. 2024). Publisher: American Physical Society, p. L100301. DOI: `10.1103/PhysRevB.110.L100301`. URL: `https://link.aps.org/doi/10.1103/PhysRevB.110.L100301` (visited on 11/02/2025).

[54] Xiaokang Li et al. “The phonon thermal Hall angle in black phosphorus”. en. In: *Nature Communications* 14.1 (Feb. 2023). Publisher: Nature Publishing Group, p. 1027. ISSN: 2041-1723. DOI: `10.1038/`

s41467-023-36750-3. URL: `https://www.nature.com/articles/s41467-023-36750-3` (visited on 11/02/2025).

[55] Xiaobo Jin et al. *Discovery of universal phonon thermal Hall effect in crystals*. arXiv:2404.02863 [cond-mat]. May 2024. DOI: `10.48550/arXiv.2404.02863`. URL: `http://arxiv.org/abs/2404.02863` (visited on 11/02/2025).

[56] B. Flebus. "Phonon Hall Viscosity of Ionic Crystals". In: *Physical Review Letters* 131.23 (2023). DOI: `10.1103/PhysRevLett.131.236301`.

[57] Naoto Nagaosa. "Anomalous Hall effect". In: *Reviews of Modern Physics* 82.2 (2010), pp. 1539–1592. DOI: `10.1103/RevModPhys.82.1539`.

[58] E. N. Adams and E. I. Blount. "Energy bands in the presence of an external force fieldII: Anomalous velocities". In: *Journal of Physics and Chemistry of Solids* 10.4 (Aug. 1959), pp. 286–303. ISSN: 0022-3697. DOI: `10.1016/0022-3697(59)90004-6`. URL: `https://www.sciencedirect.com/science/article/pii/0022369759900046` (visited on 10/28/2025).

[59] N A Sinitsyn. "Semiclassical theories of the anomalous Hall effect". en. In: *Journal of Physics: Condensed Matter* 20.2 (Dec. 2007), p. 023201. ISSN: 0953-8984. DOI: `10.1088/0953-8984/20/02/023201`. URL: `https://doi.org/10.1088/0953-8984/20/02/023201` (visited on 10/27/2025).

[60] Robert Karplus. "Hall Effect in Ferromagnetics". In: *Physical Review* 95.5 (1954), pp. 1154–1160. DOI: `10.1103/PhysRev.95.1154`.

[61] Ganesh Sundaram. "Wave-packet dynamics in slowly perturbed crystals: Gradient corrections and Berry-phase effects". In: *Physical Review B* 59.23 (1999), pp. 14915–14925. DOI: `10.1103/PhysRevB.59.14915`.

[62] N. A. Sinitsyn. "Coordinate shift in the semiclassical Boltzmann equation and the anomalous Hall effect". In: *Physical Review B* 73.7 (2006). DOI: `10.1103/PhysRevB.73.075318`.

[63] G. Kotliar, A. Sengupta, and C. M. Varma. "Hall effect and magnetoresistance in copper oxide metals". en. In: *Physical Review B* 53.6 (Feb. 1996), pp. 3573–3577. ISSN: 0163-1829, 1095-3795. DOI: `10.1103/PhysRevB.53.3573`. URL: `https://link.aps.org/doi/10.1103/PhysRevB.53.3573` (visited on 10/28/2025).

[64] J. Smit. "The spontaneous hall effect in ferromagnetics II". In: *Physica* 24.1 (Jan. 1958), pp. 39–51. ISSN: 0031-8914. DOI: `10.1016/S0031-8914(58)93541-9`. URL: `https://www.sciencedirect.com/science/article/pii/S0031891458935419` (visited on 10/30/2025).

[65] Haoyu Guo. "Extrinsic phonon thermal Hall transport from Hall viscosity". In: *Physical Review B* 103.20 (2021). DOI: `10.1103/PhysRevB.103.205115`.

[66] Jing-Yuan Chen. "Enhanced Thermal Hall Effect in Nearly Ferroelectric Insulators". In: *Physical Review Letters* 124.16 (2020). DOI: `10.1103/PhysRevLett.124.167601`.

[67] P. w. Anderson, B. I. Halperin, and c. M. Varma. "Anomalous low-temperature thermal properties of glasses and spin glasses". In: *The Philosophical Magazine: A Journal of Theoretical Experimental and Applied Physics* 25.1 (Jan. 1972). Publisher: Taylor & Francis _eprint: https://doi.org/10.1080/14786437208229210, pp. 1–9. ISSN: 0031-8086. DOI: `10.1080/14786437208229210`. URL: `https://doi.org/10.1080/14786437208229210` (visited on 11/03/2025).

[68] Walther Rehwald. "The study of structural phase transitions by means of ultrasonic experiments". In: *Advances in Physics* 22.6 (Nov. 1973). Publisher: Taylor & Francis _eprint: https://doi.org/10.1080/00018737300101379, pp. 721–755. ISSN: 0001-8732. DOI: `10.1080/00018737300101379`. URL: `https://doi.org/10.1080/00018737300101379` (visited on 11/03/2025).

[69] Maissam Barkeshli. "Dissipationless phonon Hall viscosity". In: *Physical Review B* 85.24 (2012). DOI: `10.1103/PhysRevB.85.245107`.

[70] J. E. Avron, R. Seiler, and P. G. Zograf. “Viscosity of Quantum Hall Fluids”. In: *Physical Review Letters* 75.4 (July 1995). Publisher: American Physical Society, pp. 697–700. DOI: `10.1103/PhysRevLett.75.697`. URL: `https://link.aps.org/doi/10.1103/PhysRevLett.75.697` (visited on 11/03/2025).

[71] Ryo Matsumoto, Ryuichi Shindou, and Shuichi Murakami. “Thermal Hall effect of magnons in magnets with dipolar interaction”. In: *Physical Review B* 89.5 (Feb. 2014). Publisher: American Physical Society, p. 054420. DOI: `10.1103/PhysRevB.89.054420`. URL: `https://link.aps.org/doi/10.1103/PhysRevB.89.054420` (visited on 11/04/2025).

[72] Tao Qin. “Berry curvature and the phonon Hall effect”. In: *Physical Review B* 86.10 (2012). DOI: `10.1103/PhysRevB.86.104305`.

[73] J. M. Luttinger. “Theory of Thermal Transport Coefficients”. In: *Physical Review* 135.6A (1964), A1505–A1514. DOI: `10.1103/PhysRev.135.A1505`.

[74] N. R. Cooper, B. I. Halperin, and I. M. Ruzin. “Thermoelectric response of an interacting two-dimensional electron gas in a quantizing magnetic field”. In: *Physical Review B* 55.4 (Jan. 1997). Publisher: American Physical Society, pp. 2344–2359. DOI: `10.1103/PhysRevB.55.2344`. URL: `https://link.aps.org/doi/10.1103/PhysRevB.55.2344` (visited on 11/04/2025).

[75] Mengxing Ye, Lucile Savary, and Leon Balents. *Phonon Hall Viscosity in Magnetic Insulators*. arXiv:2103.04223 [cond-mat]. Mar. 2021. DOI: `10.48550/arXiv.2103.04223`. URL: `http://arxiv.org/abs/2103.04223` (visited on 09/17/2025).

[76] Ramesh Dhakal et al. *Theory of Intrinsic Phonon Thermal Hall Effect in ££-RuCl£_3£*. arXiv:2407.00660 [cond-mat]. Mar. 2025. DOI: `10.48550/arXiv.2407.00660`. URL: `http://arxiv.org/abs/2407.00660` (visited on 11/04/2025).

[77] Yunchao Zhang. “Phonon Hall viscosity from phonon-spinon interactions”. In: *Physical Review B* 104.3 (2021). DOI: `10.1103/PhysRevB.104.035103`.

[78] Sungjoon Park, Naoto Nagaosa, and Bohm-Jung Yang. "Thermal Hall Effect, Spin Nernst Effect, and Spin Density Induced by a Thermal Gradient in Collinear Ferrimagnets from MagnonPhonon Interaction". In: *Nano Letters* 20.4 (Apr. 2020). Publisher: American Chemical Society, pp. 2741–2746. ISSN: 1530-6984. DOI: `10.1021/acs.nanolett.0c00363`. URL: `https://doi.org/10.1021/acs.nanolett.0c00363` (visited on 11/04/2025).

[79] Fedor F. Balakirev et al. "Resonant ultrasound spectroscopy: The essential toolbox". In: *Review of Scientific Instruments* 90.12 (Dec. 2019), p. 121401. ISSN: 0034-6748. DOI: `10.1063/1.5123165`. URL: `https://doi.org/10.1063/1.5123165` (visited on 11/04/2025).

[80] Bruno Luthi. *Physical Acoustics in the Solid State*. en. Vol. 148. Solid State Sciences. Berlin/Heidelberg: Springer-Verlag, 2005. ISBN: 978-3-540-22910-0. DOI: `10.1007/b138867`. URL: `http://link.springer.com/10.1007/b138867` (visited on 11/04/2025).

[81] Vladimir Cherepanov, Igor Kolokolov, and Victor L'vov. "The saga of YIG: Spectra, thermodynamics, interaction and relaxation of magnons in a complex magnet". In: *Physics Reports* 229.3 (July 1993), pp. 81–144. ISSN: 0370-1573. DOI: `10.1016/0370-1573(93)90107-O`. URL: `https://www.sciencedirect.com/science/article/pii/037015739390107O` (visited on 08/19/2025).

[82] Shyh Wang and J. Crow. "Acoustic Faraday rotation". In: *IEEE Transactions on Magnetics* 7.1 (Mar. 1971), pp. 138–141. ISSN: 1941-0069. DOI: `10.1109/TMAG.1971.1067017`. URL: `https://ieeexplore.ieee.org/document/1067017` (visited on 08/19/2025).

[83] Andrew J. Princep et al. "The full magnon spectrum of yttrium iron garnet". en. In: *npj Quantum Materials* 2.1 (Nov. 2017). Publisher: Nature Publishing Group, p. 63. ISSN: 2397-4648. DOI: `10.1038/s41535-017-0067-y`. URL: `https://www.nature.com/articles/s41535-017-0067-y` (visited on 08/19/2025).

[84] D. Rodic et al. "True magnetic structure of the ferrimagnetic garnet Y3Fe5O12 and magnetic moments of iron ions". In: *Journal of Magnetism and Magnetic Materials* 191.1 (Jan. 1999), pp. 137–145. ISSN:

0304-8853. DOI: `10.1016/S0304-8853(98)00317-5`. URL: `https://www.sciencedirect.com/science/article/pii/S0304885398003175` (visited on 08/19/2025).

[85] M. Bonnet et al. "Refinement of the structure of yttrium iron garnet (YIG). A case of severe extinction and absorption". en. In: *Acta Crystallographica Section B* 31.9 (1975). _eprint: https://onlinelibrary.wiley.com/doi/pdf/10.1107/S0567740875007315, pp. 2233–2240. ISSN: 1600-5740. DOI: `10.1107/S0567740875007315`. URL: `https://onlinelibrary.wiley.com/doi/abs/10.1107/S0567740875007315` (visited on 08/19/2025).

[86] Imaddin A. Al-Omari, Ralph Skomski, and David J. Sellmyer. "Magnetic Properties of Y32xCa2xFe5xVxO12 Garnets". en. In: *Advances in Materials Physics and Chemistry* 2.3 (Sept. 2012). Publisher: Scientific Research Publishing, pp. 116–120. DOI: `10.4236/ampc.2012.23019`. URL: `https://www.scirp.org/journal/paperinformation?paperid=23196` (visited on 08/19/2025).

[87] H. Maier-Flaig et al. "Temperature-dependent magnetic damping of yttrium iron garnet spheres". In: *Physical Review B* 95.21 (June 2017). Publisher: American Physical Society, p. 214423. DOI: `10.1103/PhysRevB.95.214423`. URL: `https://link.aps.org/doi/10.1103/PhysRevB.95.214423` (visited on 08/19/2025).

[88] D. N. Bose, S. R. Borgaonkar, and T. S. Vedavathy. "Measurement of magnetic properties of single crystal YIG by non-resonant method". en. In: *Bulletin of Materials Science* 1.2 (Oct. 1979), pp. 121–128. ISSN: 0973-7669. DOI: `10.1007/BF02908575`. URL: `https://doi.org/10.1007/BF02908575` (visited on 08/19/2025).

[89] Xiaoming Yang et al. "High Quality and Large Size Yttrium Iron Garnet Crystal Grown by Top Seeded Solution Growth Technique". EN. In: *Journal of Inorganic Materials* 38.3 (2023), p. 322. ISSN: 1000-324X. DOI: `10.15541/jim20220353`. URL: `https://www.researching.cn/articles/OJ67c46d322ae72b87` (visited on 08/19/2025).

[90] Shin-ichi Shamoto et al. "Ultralow-energy magnon anomaly in yttrium iron garnet". In: *Physical Review Research* 2.3 (Aug. 2020). Publisher: American Physical Society, p. 033235. DOI: `10.1103/PhysRevResearch.2.033235`. URL: `https://link.aps.`

`org/doi/10.1103/PhysRevResearch.2.033235` (visited on 08/19/2025).

[91] E. R. Callen et al. "Magnetostriction in Cubic N\'eel Ferrimagnets, with Application to YIG". In: *Physical Review* 130.5 (June 1963). Publisher: American Physical Society, pp. 1735–1740. DOI: `10.1103/PhysRev.130.1735`. URL: `https://link.aps.org/doi/10.1103/PhysRev.130.1735` (visited on 08/19/2025).

[92] VV Lemanov, AV Pavlenko, and AN Grishmanovskii. "Interaction between elastic and spin waves in yttrium iron garnet crystals". In: *Soviet PhysicsJETP [translation of Zhurnal Eksperimentalnoi i Teoreticheskoi Fiziki]* 32 (1971), p. 389.

[93] A. E. Clark and R. E. Strakna. "Elastic Constants of SingleCrystal YIG". In: *Journal of Applied Physics* 32.6 (June 1961), pp. 1172–1173. ISSN: 0021-8979. DOI: `10.1063/1.1736184`. URL: `https://doi.org/10.1063/1.1736184` (visited on 08/20/2025).

[94] Shuichi Iida. "Magnetostriction Constants of Rare Earth Iron Garnets". en. In: *Journal of the Physical Society of Japan* 22.5 (May 1967), pp. 1201–1209. ISSN: 0031-9015, 1347-4073. DOI: `10.1143/JPSJ.22.1201`. URL: `https://journals.jps.jp/doi/10.1143/JPSJ.22.1201`.

[95] R. V. Jones, G. P. Rodrigue, and W. P. Wolf. "Ferrimagnetic Resonance in Single Crystals of Rare Earth Garnet Materials". In: *Journal of Applied Physics* 29.3 (Mar. 1958), pp. 434–435. ISSN: 0021-8979. DOI: `10.1063/1.1723170`. URL: `https://doi.org/10.1063/1.1723170`.

[96] Junya Yamamoto, Bernard T. Smith, and Ely E. Bell. "Far-infrared spectra of dysprosium and terbium iron garnet". EN. In: *JOSA* 64.6 (June 1974). Publisher: Optica Publishing Group, pp. 880–883. DOI: `10.1364/JOSA.64.000880`. URL: `https://opg.optica.org/josa/abstract.cfm?uri=josa-64-6-880`.

[97] Tao Zhu et al. "Effects of a high DC magnetic field on spin reorientation in dysprosium- yttrium iron garnets at low temperatures". In: *AIP Advances* 9.3 (Mar. 2019), p. 035326. ISSN: 2158-3226. DOI: `10.1063/1.5079559`. URL: `https://doi.org/10.1063/1.5079559`.

[98] Avi Shragai et al. *Phonon Hall Viscosity and the intrinsic thermal Hall effect of α-RuCl$_3$*. Oct. 2025. DOI: `10.48550/arXiv.2510.06443`. URL: `https://arxiv.org/abs/2510.06443` (visited on 09/17/2025).

[99] Hosho Katsura, Naoto Nagaosa, and Patrick A. Lee. "Theory of the Thermal Hall Effect in Quantum Magnets". In: *Physical Review Letters* 104.6 (Feb. 2010), p. 066403. DOI: `10.1103/PhysRevLett.104.066403`. (Visited on 06/02/2025).

[100] Xiao-Tian Zhang, Yong Hao Gao, and Gang Chen. "Thermal Hall Effects in Quantum Magnets". In: *Physics Reports*. Thermal Hall Effects in Quantum Magnets 1070 (June 2024), pp. 1–59. ISSN: 0370-1573. DOI: `10.1016/j.physrep.2024.03.004`. (Visited on 06/02/2025).

[101] Max Hirschberger et al. "Large Thermal Hall Conductivity of Neutral Spin Excitations in a Frustrated Quantum Magnet". In: *Science* 348.6230 (Apr. 2015), pp. 106–109. DOI: `10.1126/science.1257340`. (Visited on 10/23/2024).

[102] T. Yokoi et al. "Half-Integer Quantized Anomalous Thermal Hall Effect in the Kitaev Material Candidate α-RuCl3". In: *Science* 373.6554 (July 2021), pp. 568–572. DOI: `10.1126/science.aay5551`. (Visited on 10/23/2024).

[103] Peter Czajka et al. "Oscillations of the Thermal Conductivity in the Spin-Liquid State of α-RuCl3". In: *Nature Physics* 17.8 (Aug. 2021), pp. 915–919. ISSN: 1745-2481. DOI: `10.1038/s41567-021-01243-x`. (Visited on 05/01/2025).

[104] Daiki Watanabe et al. "Emergence of Nontrivial Magnetic Excitations in a Spin-Liquid State of Kagomé Volborthite". In: *Proceedings of the National Academy of Sciences* 113.31 (Aug. 2016), pp. 8653–8657. DOI: `10.1073/pnas.1524076113`. (Visited on 06/02/2025).

[105] Hayato Doki et al. "Spin Thermal Hall Conductivity of a Kagome Antiferromagnet". In: *Physical Review Letters* 121.9 (Aug. 2018), p. 097203. DOI: `10.1103/PhysRevLett.121.097203`. (Visited on 06/02/2025).

[106] Masatoshi Akazawa et al. "Thermal Hall Effects of Spins and Phonons in Kagome Antiferromagnet Cd-Kapellasite". In: *Physical Review X* 10.4 (Dec. 2020), p. 041059. DOI: `10.1103/PhysRevX.10.041059`. (Visited on 06/02/2025).

[107] Marie-Eve Boulanger et al. "Thermal Hall Conductivity of Electron-Doped Cuprates". In: *Physical Review B* 105.11 (Mar. 2022), p. 115101. DOI: `10.1103/PhysRevB.105.115101`. (Visited on 06/06/2025).

[108] Lu Chen et al. "Large Phonon Thermal Hall Conductivity in the Antiferromagnetic Insulator Cu_3TeO_6". In: *Proceedings of the National Academy of Sciences* 119.34 (Aug. 2022), e2208016119. DOI: `10.1073/pnas.2208016119`. (Visited on 10/23/2024).

[109] A. Ataei et al. "Phonon Chirality from Impurity Scattering in the Antiferromagnetic Phase of Sr_2IrO_4". In: *Nature Physics* 20.4 (Apr. 2024), pp. 585–588. ISSN: 1745-2481. DOI: `10.1038/s41567-024-02384-5`. (Visited on 06/06/2025).

[110] Xiaokang Li et al. "Phonon Thermal Hall Effect in Strontium Titanate". In: *Physical Review Letters* 124.10 (Mar. 2020), p. 105901. DOI: `10.1103/PhysRevLett.124.105901`. (Visited on 10/23/2024).

[111] Xiaokang Li et al. "The Phonon Thermal Hall Angle in Black Phosphorus". In: *Nature Communications* 14.1 (Feb. 2023), p. 1027. ISSN: 2041-1723. DOI: `10.1038/s41467-023-36750-3`. (Visited on 06/10/2025).

[112] Ashvini Vallipuram et al. "Role of Magnetic Ions in the Thermal Hall Effect of the Paramagnetic Insulator $TmVO_4$". In: *Physical Review B* 110.4 (July 2024), p. 045144. DOI: `10.1103/PhysRevB.110.045144`. (Visited on 06/06/2025).

[113] Tao Qin, Jianhui Zhou, and Junren Shi. "Berry Curvature and the Phonon Hall Effect". In: *Physical Review B* 86.10 (Sept. 2012), p. 104305. DOI: `10.1103/PhysRevB.86.104305`. (Visited on 11/13/2024).

[114] Yunchao Zhang et al. "Phonon Hall Viscosity from Phonon-Spinon Interactions". In: *Physical Review B* 104.3 (July 2021), p. 035103. DOI: `10.1103/PhysRevB.104.035103`. (Visited on 11/13/2024).

[115] Mengxing Ye, Lucile Savary, and Leon Balents. *Phonon Hall Viscosity in Magnetic Insulators*. Preprint at `https://arxiv.org/abs/2103.04223`. Mar. 2021.

[116] B. Flebus and A. H. MacDonald. “Phonon Hall Viscosity of Ionic Crystals”. In: *Physical Review Letters* 131.23 (Dec. 2023), p. 236301. DOI: `10.1103/PhysRevLett.131.236301`. (Visited on 06/04/2025).

[117] Jing-Yuan Chen, Steven A. Kivelson, and Xiao-Qi Sun. “Enhanced Thermal Hall Effect in Nearly Ferroelectric Insulators”. In: *Physical Review Letters* 124.16 (Apr. 2020), p. 167601. DOI: `10.1103/PhysRevLett.124.167601`. (Visited on 06/04/2025).

[118] B. Flebus and A. H. MacDonald. “Charged Defects and Phonon Hall Effects in Ionic Crystals”. In: *Physical Review B* 105.22 (June 2022), p. L220301. DOI: `10.1103/PhysRevB.105.L220301`. (Visited on 06/04/2025).

[119] Haoyu Guo, Darshan G. Joshi, and Subir Sachdev. “Resonant Thermal Hall Effect of Phonons Coupled to Dynamical Defects”. In: *Proceedings of the National Academy of Sciences* 119.46 (Nov. 2022), e2215141119. DOI: `10.1073/pnas.2215141119`. (Visited on 06/10/2025).

[120] Emily Z. Zhang, Li Ern Chern, and Yong Baek Kim. “Topological Magnons for Thermal Hall Transport in Frustrated Magnets with Bond-Dependent Interactions”. In: *Physical Review B* 103.17 (May 2021), p. 174402. DOI: `10.1103/PhysRevB.103.174402`. (Visited on 06/11/2025).

[121] Li Ern Chern, Emily Z. Zhang, and Yong Baek Kim. “Sign Structure of Thermal Hall Conductivity and Topological Magnons for In-Plane Field Polarized Kitaev Magnets”. In: *Physical Review Letters* 126.14 (Apr. 2021), p. 147201. DOI: `10.1103/PhysRevLett.126.147201`. (Visited on 06/11/2025).

[122] Jacob S. Gordon et al. “Theory of the Field-Revealed Kitaev Spin Liquid”. In: *Nature Communications* 10.1 (June 2019), p. 2470. ISSN: 2041-1723. DOI: `10.1038/s41467-019-10405-8`. (Visited on 06/11/2025).

[123] J. E. Avron, R. Seiler, and P. G. Zograf. “Viscosity of Quantum Hall Fluids”. In: *Physical Review Letters* 75.4 (July 1995), pp. 697–700. DOI: `10.1103/PhysRevLett.75.697`. (Visited on 05/22/2025).

[124] Maissam Barkeshli, Suk Bum Chung, and Xiao-Liang Qi. “Dissipationless Phonon Hall Viscosity”. In: *Physical Review B* 85.24 (June 2012), p. 245107. DOI: `10.1103/PhysRevB.85.245107`. (Visited on 10/23/2024).

[125] Y. Kasahara et al. “Majorana Quantization and Half-Integer Thermal Quantum Hall Effect in a Kitaev Spin Liquid”. In: *Nature* 559.7713 (July 2018), pp. 227–231. ISSN: 1476-4687. DOI: `10.1038/s41586-018-0274-0`. (Visited on 05/01/2025).

[126] J. a. N. Bruin et al. “Robustness of the Thermal Hall Effect Close to Half-Quantization in α-RuCl3”. In: *Nature Physics* 18.4 (Apr. 2022), pp. 401–405. ISSN: 1745-2481. DOI: `10.1038/s41567-021-01501-y`. (Visited on 06/02/2025).

[127] C. Kittel. “Interaction of Spin Waves and Ultrasonic Waves in Ferromagnetic Crystals”. In: *Physical Review* 110.4 (May 1958), pp. 836–841. DOI: `10.1103/PhysRev.110.836`. (Visited on 05/29/2025).

[128] M. Boiteux et al. “Acoustical Faraday Effect in Antiferromagnetic Cr_2O_3”. In: *Physical Review B* 4.9 (Nov. 1971), pp. 3077–3088. DOI: `10.1103/PhysRevB.4.3077`. (Visited on 05/20/2025).

[129] Shyh Wang and J. Crow. “Acoustic Faraday Rotation”. In: *IEEE Transactions on Magnetics* 7.1 (Mar. 1971), pp. 138–141. ISSN: 1941-0069. DOI: `10.1109/TMAG.1971.1067017`. (Visited on 05/20/2025).

[130] A. Sytcheva et al. “Acoustic Faraday Effect in $Tb_3Ga_5O_{12}$”. In: *Physical Review B* 81.21 (June 2010), p. 214415. DOI: `10.1103/PhysRevB.81.214415`. (Visited on 07/07/2025).

[131] C. Strohm, G. L. J. A. Rikken, and P. Wyder. “Phenomenological Evidence for the Phonon Hall Effect”. In: *Physical Review Letters* 95.15 (Oct. 2005), p. 155901. DOI: `10.1103/PhysRevLett.95.155901`. (Visited on 07/29/2025).

[132] R. Guermeur et al. “Rotation Du Plan de Polarisation d’une Onde Ultrasonore Se Propageant Dans Un Cristal Paramagnetique”. In: *Solid State Communications* 6.8 (Aug. 1968), pp. 519–522. ISSN: 0038-1098. DOI: `10.1016/0038-1098(68)90502-4`. (Visited on 07/29/2025).

[133] B. Lüthi and C. Lingner. “Magnetoelasticity, Rotational Invariance and Magnetoacoustic Birefringence in CeAl$_2$”. In: *Zeitschrift für Physik B Condensed Matter* 34.2 (June 1979), pp. 157–163. ISSN: 1431-584X. DOI: `10.1007/BF01322137`. (Visited on 07/29/2025).

[134] Y. Lee et al. “Discovery of the Acoustic Faraday Effect in Superfluid ^{3}He-B”. In: *Nature* 400.6743 (July 1999), pp. 431–433. ISSN: 1476-4687. DOI: `10.1038/22712`. (Visited on 07/07/2025).

[135] H. B. Cao et al. “Low-Temperature Crystal and Magnetic Structure of α-RuCl$_3$”. In: *Physical Review B* 93.13 (Apr. 2016), p. 134423. DOI: `10.1103/PhysRevB.93.134423`. (Visited on 06/02/2025).

[136] Subin Kim et al. “Structural Transition and Magnetic Anisotropy in α-RuCl$_3$”. In: *Physical Review B* 109.14 (Apr. 2024), p. L140101. DOI: `10.1103/PhysRevB.109.L140101`. (Visited on 06/02/2025).

[137] C. Balz et al. “Field-Induced Intermediate Ordered Phase and Anisotropic Interlayer Interactions in α-RuCl$_3$”. In: *Physical Review B* 103.17 (May 2021), p. 174417. DOI: `10.1103/PhysRevB.103.174417`. (Visited on 06/02/2025).

[138] Subin Kim, Bo Yuan, and Young-June Kim. “α-RuCl$_3$ and Other Kitaev Materials”. In: *APL Materials* 10.8 (Aug. 2022), p. 080903. ISSN: 2166-532X. DOI: `10.1063/5.0101512`. (Visited on 05/27/2025).

[139] A. Hauspurg et al. “Fractionalized Excitations Probed by Ultrasound”. In: *Physical Review B* 109.14 (Apr. 2024), p. 144415. ISSN: 2469-9950, 2469-9969. DOI: `10.1103/PhysRevB.109.144415`. (Visited on 11/01/2024).

[140] Blair W. Lebert et al. “Acoustic Phonon Dispersion of `$\ensuremath{\alpha}\text{\ensur`
`}}{\mathrm{RuCl}}_{3}$`”. In: *Physical Review B* 106.4 (July 2022), p. L041102. DOI: `10.1103/PhysRevB.106.L041102`. (Visited on 05/29/2025).

[141] K. A. Modic et al. "Scale-Invariant Magnetic Anisotropy in $RuCl_3$ at High Magnetic Fields". In: *Nature Physics* 17.2 (Feb. 2021), pp. 240–244. ISSN: 1745-2481. DOI: `10.1038/s41567-020-1028-0`. (Visited on 06/27/2024).

[142] Xu-Guang Zhou et al. "Possible Intermediate Quantum Spin Liquid Phase in α-$RuCl_3$ under High Magnetic Fields up to 100 T". In: *Nature Communications* 14.1 (Sept. 2023), p. 5613. ISSN: 2041-1723. DOI: `10.1038/s41467-023-41232-7`. (Visited on 07/03/2025).

[143] E. Lefrancois et al. "Evidence of a Phonon Hall Effect in the Kitaev Spin Liquid Candidate α-$RuCl_3$". In: *Physical Review X* 12.2 (Apr. 2022), p. 021025. DOI: `10.1103/PhysRevX.12.021025`. (Visited on 05/16/2025).

[144] O. Tanaka et al. "Thermodynamic Evidence for a Field-Angle-Dependent Majorana Gap in a Kitaev Spin Liquid". In: *Nature Physics* 18.4 (Apr. 2022), pp. 429–435. ISSN: 1745-2481. DOI: `10.1038/s41567-021-01488-6`. (Visited on 06/09/2025).

[145] Ramesh Dhakal et al. *Theory of Intrinsic Phonon Thermal Hall Effect in α-$RuCl_3$*. Preprint at `https://arxiv.org/abs/2407.00660`. Mar. 2025.

[146] Seung-Hwan Do et al. "Short-Range Quasistatic Order and Critical Spin Correlations in α-$Ru_{1-x}Ir_xCl_3$". In: *Physical Review B* 98.1 (July 2018), p. 014407. ISSN: 2469-9950, 2469-9969. DOI: `10.1103/PhysRevB.98.014407`. (Visited on 06/12/2025).

[147] Christian Balz et al. "Finite Field Regime for a Quantum Spin Liquid in α-$RuCl_3$". In: *Physical Review B* 100.6 (Aug. 2019), p. 060405. ISSN: 2469-9950, 2469-9969. DOI: `10.1103/PhysRevB.100.060405`. (Visited on 06/12/2025).

[148] S. Widmann et al. "Thermodynamic Evidence of Fractionalized Excitations in α-$RuCl_3$". In: *Physical Review B* 99.9 (Mar. 2019), p. 094415. DOI: `10.1103/PhysRevB.99.094415`. (Visited on 06/06/2025).

[149] Peter Czajka et al. "Planar Thermal Hall Effect of Topological Bosons in the Kitaev Magnet α-$RuCl_3$". In: *Nature Materials* 22.1 (Jan. 2023), pp. 36–41. ISSN: 1476-4660. DOI: `10.1038/s41563-022-01397-w`. (Visited on 06/06/2025).

[150] Arnab Banerjee et al. "Neutron Scattering in the Proximate Quantum Spin Liquid α-$RuCl_3$". In: *Science* 356.6342 (June 2017), pp. 1055–1059. DOI: `10.1126/science.aah6015`. (Visited on 11/01/2024).

[151] Arnab Banerjee et al. "Excitations in the Field-Induced Quantum Spin Liquid State of α-$RuCl_3$". In: *npj Quantum Materials* 3.1 (Feb. 2018), pp. 1–7. ISSN: 2397-4648. DOI: `10.1038/s41535-018-0079-2`. (Visited on 11/01/2024).

[152] Sayak Ghosh et al. "Thermodynamic Evidence for a Two-Component Superconducting Order Parameter in Sr_2RuO_4". In: *Nature Physics* 17.2 (Feb. 2021), pp. 199–204. ISSN: 1745-2481. DOI: `10.1038/s41567-020-1032-4`. (Visited on 05/17/2025).

[153] Florian Theuss et al. "Single-Component Superconductivity in UTe2 at Ambient Pressure". In: *Nature Physics* 20.7 (July 2024), pp. 1124–1130. ISSN: 1745-2481. DOI: `10.1038/s41567-024-02493-1`. (Visited on 05/17/2025).

[154] A. E. H. Love. *A Treastise on the Mathematical Theory of Elasticity*. Vol. 1. Cambridge University Press, 1892.